

# Chapter 9

## Turbulent Electron Thermal Transport in Tokamaks

There are broad and intense international collaborations as well as private sector companies working to find ways to produce power from controlling nuclear fusion reactions. Fusion reactions are Mother Nature's way to produce the enormous power from billions of stars of all sizes in the universe. We must find a way to construct plasma confinement in vessels, that is, to build a star. This is the Grand Challenge problem for the future generation of scientists and engineers. Remember more than 99.9% of the universe is in the plasma state and there are billions of stars producing fusion energy. Understanding the universe requires understanding and controlling fusion power.

The early history of the search in the USA for the path to building a fusion reactor is detailed by Steve Dean in *Search for the Ultimate Energy Source, A History of the U.S. Fusion Energy Program* (Springer) ISBN:978-4611-6036-7.

The origin of anomalous electron thermal turbulence from the spatial gradients in magnetized plasmas is universal [Horton (2018)]. Laboratory experiments demonstrating key features of drift waves are reviewed. The turbulent electromagnetic fields produce an anomalous transport that scales with both the gradient parameters and microscopic plasma scale length parameters. The change from the microscale dominated gyroBohm to the macroscale dominated Bohm scaling laws is discussed. The close correlations between the electron turbulent transport theory and the confinement properties measured in the steady-state hot-electron plasmas produced in tokamak devices are presented [Horton, *et al.* (2003)].

Plasma occurs in states of turbulence under a wide range of conditions including space and astrophysical plasmas as well as those produced in MHD stable laboratory confinement devices. The strength of the turbulence increases as the plasma is driven farther away from thermodynamic equilibrium. While there are many ways to drive the plasma away from equilibrium with particle beams, laser beams, and radio frequency waves, a universally-occurring departure from equilibrium is the existence of spatial gradients across an ambient magnetic field. The problem posed is then a classic one of determining the fluxes of particles, energy and momentum across an ambient magnetic field due to gradients in thermodynamic variables of density  $n_a$ , temperature  $T_a$  and flow velocity  $u_a$ .

Plasma distributions that are driven away from the thermodynamic equilibrium of a spatially

uniform Maxwell–Boltzmann velocity distribution with densities  $n_a$  and temperatures  $T_a$  for the charge particles species  $(e_a, m_a)$  are said to have a free energy density  $W_f$  available to drive plasma turbulence. For the first free energy example, we estimate the energy density associated with the relative cross-field drift velocity  $u$  between the ions and the electrons driven by the pressure gradient. The cross-field drift is required to maintain force balance in the nonuniform magnetized plasma with  $j \times B = \nabla p$  when  $j_\perp = \sum_a e_a n_a u_{\perp a}$  for  $n_e = \sum Z_i n_i$  and  $p = \sum_i p_i + p_e$ . The free energy density is  $W_f = \frac{1}{2} \sum_a m_a n_a u_a^2$ . The condition for the onset of instability is determined by linear stability analysis which specifies the relations between the system parameters  $\rho_a/L_{Ta}, T_e/T_i, m_i/m_e$  for various forms (different modes or branches of  $\mathcal{E}_{ij} \tilde{E}_j(k) = 0$ ) of  $q$  unstable plasma waves. Here  $\rho_a = c(m_a T_a)^{1/2}/e_a B$  is the thermal gyroradius. The nature of the nonlinear saturated state depends on how far into the unstable domain the system parameters reside which typically varies with space and time as the plasma turbulence reacts on the plasma distributions to push the system back toward one of the marginally stable states. The turbulence provides a mechanism for self-organization toward a relaxed dynamical state often containing a mixture of waves, vortices and zonal flows. The best high temperature, steady-state plasma confinement experiments are produced in tokamaks with large temperature gradients from the core plasma that is often more than twenty million degrees Kelvin surrounded by a room temperature wall no more than one meter away. These high-temperature gradients drive two well-known types of temperature gradient instabilities called the ITG and ETG modes for ion or electron temperature gradient instabilities. We will concentrate in this work on recent theoretical and experimental research on the electron temperature gradient driven turbulent transport. While much is known about these turbulence mechanisms there is still a need for more detailed formulas to make reliable predictions for operational regimes of future large tokamaks. Thus, we review the recent results on electron transport for the purpose of showing more clearly the areas that need further investigations to make predictions for the next generation of large tokamaks.

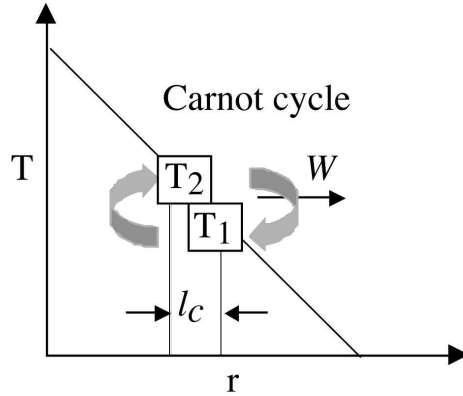


Figure 9.1: The thermodynamics of the Carnot cycle operating in a steep electron temperature gradient over correlation length  $l_c$  of the turbulent convection. The maximum energy density  $W$  to drive the turbulence occurs for a reversible Carnot cycle which gives  $W \leq P_c^2 (dT_e/dr) (N_e dT_e/dr - (2/3) T_e dN_e/dr) / T_e$  for the electron gas of density  $N_e$  and temperature  $T_e$ .

Figure 9.1 shows a schematic of the temperature gradient that operates a Carnot engine through a plasma convection to liberate energy  $W$  over a correlation length  $l_c$ . The plasma simulations of turbulence show that there are many vortices and wave structures that carry out this transport of plasma energy across the magnetic field much faster than one would calculated from collisional transport mechanisms in the plasma. This rapid transport of thermal energy is what has prevented the last generation of tokamaks from reaching the burning plasma state when are operating with deuterium and tritium fuels.

We now define the correlation functions, and correlation times and lengths needed to discuss plasma turbulence and show a simple example of their measurement in a controlled steady-state laboratory plasma.

## 9.1 Identifying Microinstabilities in Tokamak Pedestals

TO BE ADDED

## 9.2 Application of Gyrokinetic “Fingerprints” in Identifying Microinstabilities in a DIII–D Pedestal

### 9.2.1 Transport “fingerprints” of various gyrokinetic microinstabilities

TO BE ADDED

Table 9.1: [*Kotschenreuther, et al.* (2019)]

Mode:	$\chi_i/\chi_e$	$D_e/\chi_e$	$D_z/\chi_e$	Inward Particle Pinches	Shear Suppressed?
MHD-like (e.g. KBM)	$\sim 1$	$\sim 2/3$	$\sim 2/3$	No	No
MTM	$\sim 0$	$\sim 0$	$\sim 0$	No	No
ETG	$\sim 0$	$\sim 0$	$\sim 0$	No	No
ITG/TEM $\geq 1$	$-0.2 - 1$	$\sim 1$	Sometimes	Usually	

### 9.2.2 Experimental observations in DIII–D shot 174082

Strong electromagnetic fluctuations with frequencies appear at  $\sim 420$  kHz and  $\sim 140$  kHz. Shot 174082 has no heating sourced by pellets or gas puffing, only NBI, and is used as the baseline shot in a study of the effects of fueling methods on transport characteristics and pedestal structure [Nelson, *et al.* (2018)].

$$P_{\text{NBI}} = 4.67 \text{ MW}, \quad \beta_{\text{N}} = 2.0$$

### 9.2.3 Equilibrium profile reconstructions using OMFIT software package

Inter–ELM equilibrium reconstruction uses One Modeling Framework for Integrated Tasks (OMFIT) profiles, Osborne, and Consistent Automatic Kinetic Equilibrium (CAKE) packages with Thomson scattering and charge–exchange recombination data. Iterative process on kinetic equilibria generates accurate equilibrium profiles, consisting of magnetic geometry, pressure,  $q$ –profile, pressure derivative, and toroidal current source. There is a small dip in the edge of the safety factor, indicating low shear in the pedestal, a characteristic of microtearing modes observed in previous studies [Liu (2018)].

### 9.2.4 GENE simulations of the pedestal

High–resolution local linear, global linear, and local nonlinear simulations are performed across the pedestal, for a wide array of toroidal mode numbers. Nonlinear simulations are local, with minimum  $k_y \rho_i = 5$ , to find transport levels of the ETG. Global simulations focus on the wavenumber range  $k_y \rho_i < 1$ , with toroidal mode numbers ranging from  $n = 3$ –14. Each ion species is fully kinetic. Global simulations make use of the block structured grids algorithm, which adjusts the velocity space grid based on the electron temperature amplitude.

Global runs require high resolutions in the radial direction. Simulations in this study have a grid size of  $(x, z, v_{\parallel}, v_{\perp}) = (256, 96, 32, 16)$ . Block structuring the velocity grids improves performance by resolving with lower resolution in velocity space. There is roughly a 30% increase in efficiency of runs using BSG. Simulations take into account  $\mathbf{E} \times \mathbf{B}$  shear using interferometer data provided by DIII–D team.

## Results

Magnetic and electrostatic potential eigenfunctions lead to minimal parallel electric field cancellation. Upon simulation, the “fingerprints” of the observed linear mode are collected and compared. Global simulations indicate that a majority of heat transport is in the electron channel and the turbulence is electromagnetic in character.

### 9.2.5 Identifying instabilities based on “fingerprints”

Global simulation (“fingerprints”) correspond directly to the predicted behavior of microtearing modes.

### 9.2.6 Comparison between experimental and simulation results

Simulated microtearing modes have frequencies that correspond directly to the bands found in the experiments. The real frequencies of the MTMs also agree well with the predictions of analytic theory. The fastest-growing simulated mode agrees well with the highest experimental frequency. There currently is work being done on global simulations of modified equilibria to see if the experimentally-observed gap in frequencies can be replicated.

### 9.2.7 Edge modeling analysis

**TO BE ADDED**

Edge modeling analysis: SOLPS diffusivities

**TO BE ADDED**

Edge modeling analysis: Electron particle flux

**TO BE ADDED**

### 9.2.8 Conclusions

The “fingerprints” method of instability identification categorizes modes is based on the physical characteristics of transport. In conjunction with simulations, this is a powerful tool that identifies causes of pedestal microturbulence. Microtearing modes are proving to be a valid candidate as the major cause of experimentally-observed anomalous heat losses. Despite the multitude of modes driven unstable in the pedestal region, systematic simulations can accurately report the underlying physics of the fastest-growing mode in the linear regime. Taking into consideration a reasonable variation of equilibrium profiles leads to a significant increase in ETG transport, but not enough to satisfy power balance derived from the plasma profiles.

Advances in gyrokinetic codes, along with analytic techniques for mode identification based on “fingerprints” method have found the significance of Microtearing Modes (MTM) and Electron Temperature Gradient (ETG) modes in driving the energy losses within the Edge Transport Barriers (ETB) of fusion experiments operating in the ELMy H-mode regime. Gyrokinetic simulations using the Gyrokinetic Electromagnetic Numerical Experiment (GENE) code [Liu (2018)] are performed using equilibrium EFIT profiles constructed from experimental data. Nonlinear local simulations of DIII-D shots 174082 and 174092 have shown that electron heat flux has only minor contributions from ETG turbulence, allowing for the presence of MTM’s and neoclassical effects to account for observed energy losses. The increased particle sources in shot 174092 leads to additional transport mechanisms. The Microtearing Modes (MTM) instabilities found in simulations of shot 174082 are consistent with an observed magnetic fluctuation, having a frequency in the electron diamagnetic direction and range. Simulation results have also shown that Kinetic Ballooning Modes (KBM) can contribute to particle losses in pedestals. Fluctuations linked to KBMs and MTMs provides a useful “fingerprint” in distinguishing these two modes, and can be used in a quasilinear prediction of transport channels.

Following the analysis of *Halfmoon, et al.* (2019), we analyze the electromagnetic fluctuations and transport in the DIII-D tokamak showing how the drift wave turbulence produces the plasma transport in the plasma near and across the magnetic separatrix and how this relates to the experimental data.

For complex structured signals  $\varphi(x, t)$ , typical of what is meant by the term turbulence, the standard measure of the coherence of the signals is the two-point, two-time correlation function

$$C_{12}(x, t_1, x_2, t_2) = \langle \varphi(x_1, t_1) \varphi(x_2, t_2) \rangle \quad (9.1)$$

where the average  $\langle \rangle$  is the time average taken over a time period  $T$  that contains many oscillations of the associated field. The correlation functions for the plasma electric potential  $\varphi$  and the fluctuations of the electron density  $\delta n_e = n_e(x, t) - \langle n_e \rangle$  are the principal structure functions measured in laboratory plasma turbulence research. The dependence of  $C_{12}$  on  $r = x_1$  and  $\tau = t_2 - t_1$  is strong, decaying to small values for large  $r, \tau$  and weak on  $R = (r_1 + r_2)/2$  and  $t = (t_1 + t_2)/2$  for typical turbulent systems. In the physics idealization of homogeneous, stationary turbulence  $C_{12} \rightarrow C_{12}(r, \tau)$  independent of  $R$  and  $t$ . It is evident that  $C_{12}(r, \tau)$  is a maximum at  $r = 0, \tau = 0$  where  $C_{12}(0, 0) = \langle \varphi^2 \rangle$ . The space and time separation where  $C_{12}$  falls to low

values for large  $|r| \geq \ell_c$  or  $|\tau| \geq \tau_c$  defines the correlation length  $\ell_c$ . These properties provide the definition of the correlation distances  $\Delta x_c, \Delta y_c, \Delta z_c$  and correlation time  $\tau_c$  by choosing a critical point for the fall-off of  $C_{12}/C_{12}(0, 0)$  often taken as the  $1/e$ -point. Often a theoretically more useful definition of the correlation length  $\Delta x_L$  or time  $\tau_c$  is the integral scale length such that  $\Delta x_L C_{12}(0, 0) = \int_{-\infty}^{+\infty} dx C_{12}(x, \tau)$  and  $\tau_c C_{12}(\tau = 0) = \int_0^{\infty} C_{12}(\tau) d\tau$ . Typically the subscripts on  $C_{12}$  are dropped and the particular fields used in the correlation functions are implied.

A clear example of the plasma turbulence correlation function for the electrostatic potential  $\varphi(x, t)$  turbulence is shown in Fig. 9.2 from the experiment of *Stenzel* (1978). In Fig. 9.2(a) the decay of the two-point correlation function of separation  $\Delta z$  of the two space points along the direction of the plasma current  $j = -enu$  driving the turbulence is shown for all other separations ( $\Delta x = \Delta y = \tau = 0$ ) equal to zero. In Fig. 9.2(b) the constant level contours of  $C_{12}$  of the correlation function for separations in  $\Delta z$  along the current and in an orthogonal direction  $\Delta y$  are shown. Note that the central maximum (approaching 40 units) occurs at the  $\Delta y = \Delta z = 0$  point and the correlation length ( $\Delta y_c \cong 6$  mm) perpendicular to the current is longer than the correlation parallel to the current  $\Delta z = 4$  mm. This anisotropy of the turbulence is a characteristic of plasmas due to the preferred directions of unstable wave propagation associated the geometry and the magnetic fields in the plasma systems.

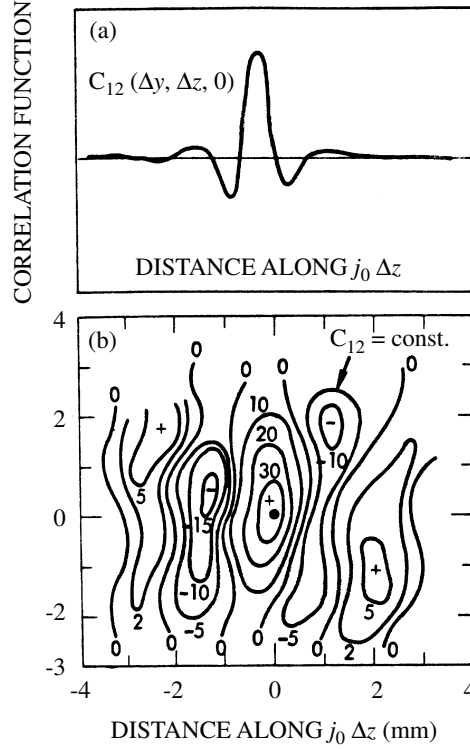


Figure 9.2: Characterization of the turbulent electrostatic potential by the two-point correlation function  $C_{12}$  in Eq. (9.1). (a) Decay of the correlation function with separation of the two points along an axial line parallel to the current; (b) Oscillatory decay of the correlations for two points in the  $y$ - $z$ -plane where the  $\hat{y}$ -direction is perpendicular to the current and  $\hat{z}$  is the parallel direction [Stenzel, *et al.* (1978)].

For broad-band turbulence there is a simple rule for estimating the correlation time  $\tau_c$  and correlation lengths  $\Delta r_c$  from the spectral width of the power spectrum  $I(k\omega)$  defined by the Fourier transform of the correlation function  $C_{12}(r, \tau)$ . The correlation time is given by  $\tau_c = 1/\Delta\omega$  and the correlation length  $\Delta z = 1/\Delta k_z$  where  $\Delta\omega = \omega_{\max} - \omega_{\min}$ ,  $\Delta k_z = k_{\max} - k_{\min}$  are the widths of the highest levels of the fluctuation power spectrum  $I(k, \omega)$ . As an example, the ion acoustic turbulence in the Stenzel experiment is shown in Fig. 9.3 where a spectrum consistent with turbulence theory has been reported. The spectral width from the  $1/e$  point is approximately 400 kHz consistent with the directly measured  $\tau_c = 2\mu\text{sec}$  correlation time. Physically, the correlation time  $\tau_c$  is the maximum time interval over which the field, in this case the electrostatic potential, maintains a given structure. In the next correlation time the complexion, or structure, of the field is qualitatively different.



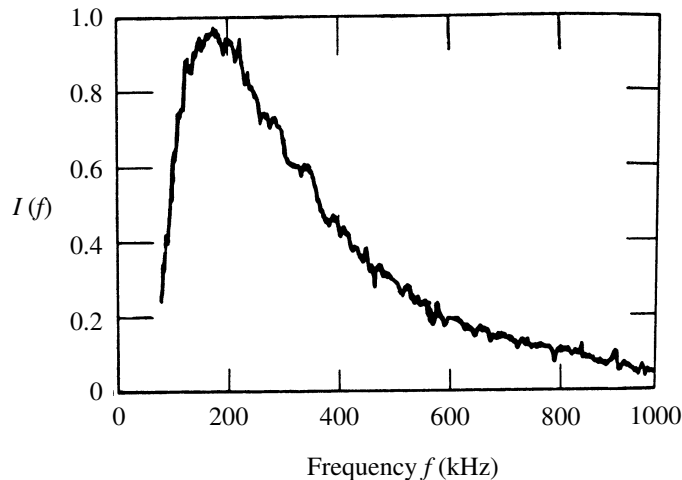


Figure 9.3: Frequency spectrum of ion acoustic turbulence showing the broadband potential fluctuation spectrum with short correlation time  $\tau_c = 1/\Delta\omega \simeq 0.4\mu\text{s}$ . The spectral distribution decreases slightly faster than  $1/\omega$  between the low-frequency cut-off due to nonlinear effects and a high frequency limit due to Landau damping on the thermal ions (courtesy of Stenzel).

The case of plasma turbulence produced by the spatial gradients from its confinement is described. The confinement or trapping of a plasma is produced both in the laboratory and space/astrophysics by magnetic fields that cause the charged particles to gyrate with radius  $\rho_a = m_a v_a / q_a B$  around the local magnetic field  $B(x)$ . The confinement along  $B$  occurs either due to the large increase of  $|B|$  giving rise to the magnetic mirror effect as in Earth’s magnetosphere or due to the field lines forming closed, nested toroidal surfaces as in solar current loops and the laboratory tokamak device. From over 30 years of laboratory research in the tokamak confinement studies of plasma there is a detailed understanding of the intrinsic, irreducible plasma turbulence that develops from spatial gradients. This turbulence is generically called drift wave turbulence and is driven by the cross-field gradients of the plasma density  $\nabla n = -(n/L_n)\hat{e}_x$  and temperature  $\nabla T = -(T/L_T)\hat{e}_x$ . While there are many detailed forms known for the turbulence depending on the plasma parameters, there are three generically distinct types of plasma cross-field diffusivities  $D[\text{m}^2/\text{s}]$  of particles and  $\chi[\text{m}^2/\text{s}]$  for thermal diffusivity. The three functionally distinct forms are: (1) the Bohm diffusivity  $D_B = \alpha_B (T_e / eB)$ , (2) the gyroBohm diffusivity from drift waves  $D_{\text{dw}} = \alpha_{\text{dw}} (\rho_i / L_T) (T_e / eB)$  where  $\rho_i = (m_i T_i)^{1/2} / eB$  is the thermal ion gyroradius and the (3) collisional turbulence diffusivities  $D_r = \alpha_{\text{rg}} \nu_e \rho_e^2 (L_S^2 / L_T R_C)$  where  $\nu_e$  is electron-ion collision frequency associated with resistivity  $E_{\parallel} = \eta j_{\parallel}$  along the magnetic field. The Bohm diffusivity varies as  $T/B$  and is documented for the Joint European Torus (JET) in *Taroni, et al.* (1994) and *Erba, et al.* (1995). A modified form, called Taroni-Bohm, of the Bohm scaling of transport has been widely accepted as a standard empirical transport formula for the two large tokamaks JET and JAERI Tokamak-60 (JT-60U) for many years. The modification is required to get the dependence on the plasma current produced magnetic field to dominate over the externally applied magnetic field. The numerical coefficient  $\alpha_B$  is a low coefficient  $\alpha_B \sim 1/200$ . In contrast, the drift wave transport formulas vary as  $T^{3/2}/B^2 L$  and are documented in theory, e.g., *Horton* (1990) and

gyrokinetic simulations with a coefficient  $\alpha_{\text{dw}} \sim 0.3$  [Dimits, *et al.* (2000)]. The third functional form of the diffusivity is that arising from resistive interchange instabilities where  $D_r$  varies as  $x_{\text{rg}} \sim n/T_e^{1/2} B^2$  and has a coefficient  $\alpha_{\text{rg}}$  of order unity [Wakatani and Hasegawa (1984), Scott (1989), Rogers, *et al.* (1998), Hallatschek and Biskamp (2001)]. The coefficients  $\alpha_B, \alpha_{\text{dw}}$  and  $\alpha_{\text{rg}}$  are weak functions of many detailed plasma parameters such as  $T_e/T_i, L_T/R, \beta = 2\mu_0 p/B^2$  and more. Just as in neutral fluid turbulence, there are many degrees of freedom excited in plasma turbulence and there is difficulty in determining the details of these formulas either through theory or numerical simulations. Nonetheless, the years of experience with the tokamak confinement program have led to rather firm general conclusions about the turbulent diffusivities. The most successful approach to modeling the transport has been called the multi-mode approach where all relevant instabilities are assessed at each set of plasma system parameters. Now we give some details of the spatial gradient driven turbulence in magnetized plasma.

### 9.3 Spatial Gradient Driven Turbulence in Magnetized Plasma

In nonuniform, magnetized plasmas the ion acoustic waves are modified into two branches with different parallel phase velocities due to the presence of the diamagnetic currents  $j_a = e_a n_a u_{da}$  required from the  $j_a \times B = \nabla p_a$  force balance. Here, each charged particle species is designated by the subscript  $a$ . The relevant drift velocities  $u_{da}$  for driving the plasma turbulence are the small diamagnetic drift velocities  $u_{da} = T_a/e_a B L_{pa} = (\rho_a/L_{pa})v_{Ta}$  where  $L_{pa}^{-1} = -\partial_x \ln p_a(x)$ . Even for small values of  $\rho_a/L_{pa}$  these diamagnetic currents drive low-frequency ( $\omega \ll e_a B/m_a$ ) waves with  $k$  almost parallel to  $B \times \nabla p_a$  unstable. These waves are called drift waves and their effect is to produce a cross-field transport of particle, energy and momentum through the turbulent  $\mathbf{E} \times \mathbf{B}$  drifts.

### 9.4 Drift Waves in the Laboratory

The collisional drift waves with growth rates determined by the electrical resistivity  $\eta$  and thermal diffusivity  $\chi_e$  were the first drift waves to be discovered in Chen (1965a,b,c) and thoroughly investigated in Hendel, *et al.* (1968). The identification was made in low temperature steady-state plasmas produced by thermal (contact) ionization of Alkali elements (principally Cesium and Potassium) in long cylindrical devices with closely-spaced Helmholtz coils. Correlations between the observed potential-density waves with the properties predicted by the linear dispersion relation and the single-wave finite amplitude formulas [Hinton and Horton (1971)] were used to establish that the radially localized, 10 kHz rotating wave structures were the drift waves. The dimensionless density  $\tilde{n}/n$  and potential  $e\tilde{\varphi}/T_e$  waves are approximately equal amplitude sinusoidal oscillation with  $\tilde{n}$  leading  $\tilde{\varphi}$  by  $30^\circ$  to  $45^\circ$  in phase. Figure 9.4 shows the drift wave potential and density

isolines. Vortex dynamics has also been observed in the plasmas produced in these devices called  $Q$ -machines in the *Hendel, et al.* (1968) experiment. Here  $Q$  is for quiet, meaning that the plasma fluctuations are not as intense and broad-band as in the toroidal devices of that period. In the experiments of *Pecseli, et al.* (1984, 1985), externally excited vortices of like signs were shown to coalesce into one vortex. Vortices of opposite signs were reported to interact with each other forming a dipole vortex pair.

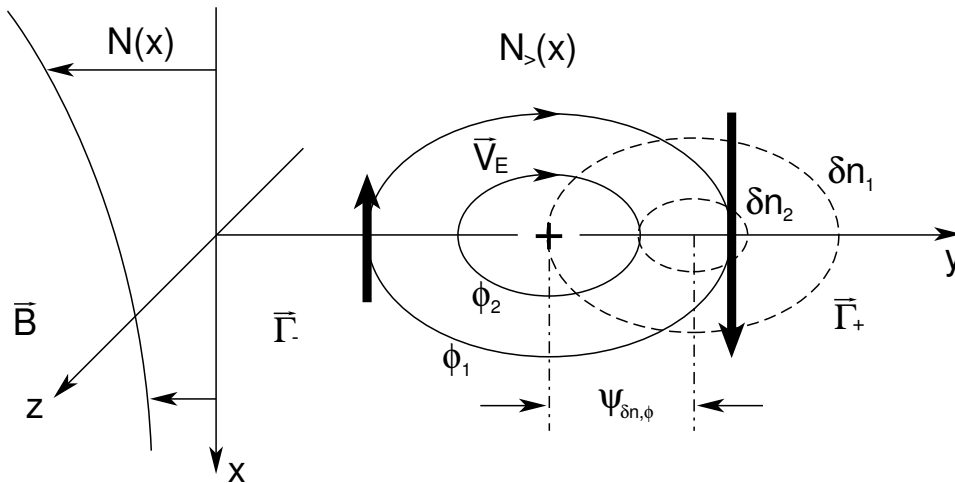


Figure 9.4: A segment of a drift wave fluctuation showing the variation of the electrostatic potential and the density perpendicular to the magnetic field at a given instant of time. The contours of  $\varphi$  in the plane perpendicular to  $B = B\hat{z}$  are the stream lines of the  $\mathbf{E} \times \mathbf{B}$  particle motion. The potential and the density variation are out of phase by  $\psi_{\delta n, \varphi}$ , producing the net downward flux.

Drift waves were found in the transient plasmas produced in the multipole confinement machines that were both linear and toroidal devices with strongly varying  $B$ -fields from parallel conductors carrying large currents from external power supplies. The theory for the drift waves in the multipole takes into account the localization of the unstable oscillations to regions of unfavorable gradient- $B$  and curvature particle drifts and the shear in the helical  $\mathbf{B}(x)$ -field [*Ohkawa and Yoshikawa* (1967)]. These experiments provided further evidence for the universal appearance of drift waves in confinement geometries. The correlation of drift wave theory with the multipole and spherator experiments are described in Sec. 3.3 of the *Horton* (1990) review article. The main result to be noted here is that the experiments show that increasing the magnetic shear reduces the fluctuation amplitudes [*Okabayashi and Arunasalam* (1977)]. The multipole devices are unique in being able to continuously vary the magnetic shear parameter strength from zero to order of unity. Even with the strongest magnetic shear, however, the fluctuations were not eliminated.

The magnetic shear plays a central role in the linear and nonlinear theory of the cross-field transport consistent with the role of shear on the fluctuations measured in these experiments. In re-

cent theory and experiments for tokamak confinement devices the combined roles of  $\mathbf{E}_r \times \mathbf{B}$  sheared flows and magnetic shear are known to produce enhanced confinement regimes [Synakowski, *et al.* (1997), Burrell (1997), Hahm (2002)]. The improved confinement occurs over narrow radial regions giving rise to new confinement regimes with internal transport barriers [Koide, *et al.* (1994), Levinton, *et al.* (1995), Strait, *et al.* (1995)]. The principal tools available for producing these changes in transport is the control of the drift wave turbulence in the system parameters through the programming of the plasma current to control the magnetic shear in  $\mathbf{B}(\mathbf{x})$  and the programming of the neutral beam injectors to control the mass flow shear in the plasma flow velocity  $\mathbf{u}(\mathbf{x})$ . The timing of the auxiliary power, the momentum injector with respect to the Ohmic transformer current is used to determine the plasma regime created.

In tokamaks the identification of drift waves in the core plasma came from the microwave scattering experiments [Mazzucato (1976)] and infrared CO<sub>2</sub> laser scattering experiments [Surko and Slusher (1976)]. These measured fluctuations were explained in the context of drift waves existing at the mixing-length level of saturation [Horton (1976)] taking into account the response of the trapped electrons in the drift-wave dissipation. Subsequently, many experiments around the world have observed the universal appearance of a broadband of drift wave fluctuations with  $\omega/2\pi \simeq 50 \text{ kHz} - 500 \text{ kHz}$  at  $k \perp = 1 \text{ cm}^{-1}$  to  $15 \text{ cm}^{-1}$  in toroidal confinement devices for both the tokamak and helical-stellarator systems. Many fluctuation and transport studies in toroidal confinement facilities around the world, including Tokamak Fusion Test Reactor (TFTR), Alto Campo Toro (Alcator), Torus Superconductor (Tore Supra), Texas Experimental Tokamak (TEXT), Advanced Toroidal Facility (ATF), Heliotron, JAERI Fusion Torus-2M (JFT-2M), Axially Symmetric Divertor Experiment (ASDEX) were undertaken in the 1980s and 1990s that have referred these initial findings of drift wave turbulence and the associated radial transport. ASDEX Upgrade experiments have drawn attention to the role of a critical electron temperature gradient in the electron power balance analysis [Ryter, *et al.* (2001ab)]. In the present work we concentrate on the recent electron transport experiments on Tore Supra where long time steady-state conditions are achieved with a well known power deposition profile and electron temperature profile. About 90% of the power goes through the electrons in the transport zone between the core and the edge plasma. This makes the system particularly simple compared to those regimes where the ions and electrons share the power transport in some complex manner. In addition there have been detailed microwave scattering experiments with polarized beams in these experiments which leads to knowledge of the electron density fluctuations and an less accurate but useful measurement of the magnetic fluctuations due a change in the polarization vector of the scattered microwave beams.

### 9.4.1 Conditions for transport and propagation of disturbances

Now we analyze the motion of charged particles in the  $\mathbf{E} \times \mathbf{B}$  convection. For the small, localized excess of ion charge shown in Fig. 9.4 the convection

$$v_E = \frac{c\mathbf{E} \times \mathbf{B}}{B^2} \quad (9.2)$$

rotates plasma clockwise around the potential maximum  $\varphi > 0$  which is also the density and electron pressure maximum in the adiabatic response. The motion is clockwise when viewed down the magnetic field line  $\mathbf{B}$ . Now, if the ambient plasma is uniform ( $\partial_x n_z = \partial_x T_i = 0$ ) across the convection zone, then the cell rotates without plasma transport. When the plasma has an  $x$ -gradient of density (pressure), however, there is a rapid transport of the structure along the symmetry direction  $\hat{\mathbf{y}}$  with a small diffusive transport across an  $x = \text{const}$  surface. The speed of the localized structure in Fig. 9.4 along the symmetry direction is approximately the electron diamagnetic drift speed  $v_{de} \equiv cT_e/eBL_n$  where  $L_n^{-1} = -\partial_r \ln N$ . The analytical description of the net convective flux particle and thermal fluxes across a given surface  $S$  is given by

$$\Gamma_e = \frac{1}{S} \int_S n_a \mathbf{v}_E \cdot d\mathbf{a} = -D_{11} \frac{dn_e}{dx} - D_{12} \frac{dT_e}{dx}, \quad (9.3)$$

$$q_e = \frac{3}{2S} \int_S n_a T_a \mathbf{v}_E \cdot d\mathbf{a} = -D_{21} \frac{dn_e}{dx} - n_e D_{22} \frac{dT_e}{dx}. \quad (9.4)$$

In the absence of the phase shift  $\psi_{\delta n, \varphi} = 0$  in Eq. (9.4), the particle transport vanishes. For different phase shifts the off-diagonal terms in Eqs. (9.3) and (9.4) can add or subtract from the diagonal terms. The situation is shown in Eqs. (9.4) where the heat flux is shown versus the electron temperature gradient. In Sec. 3 we show that the electron power balance studies show that the off-diagonal term produces an inward heat flux contribution that gives a critical gradient above which the heat flux rises to a high level. It should be understood that there are also collisional transport process that would contribute to  $\Gamma_e$  and  $q_e$  but that they are in generally smaller by one to two orders of magnitude than the turbulent fluxes [Shaing (1988)]. The collisional fluxes also exhibit off-diagonal structures [Balescu (1988)].

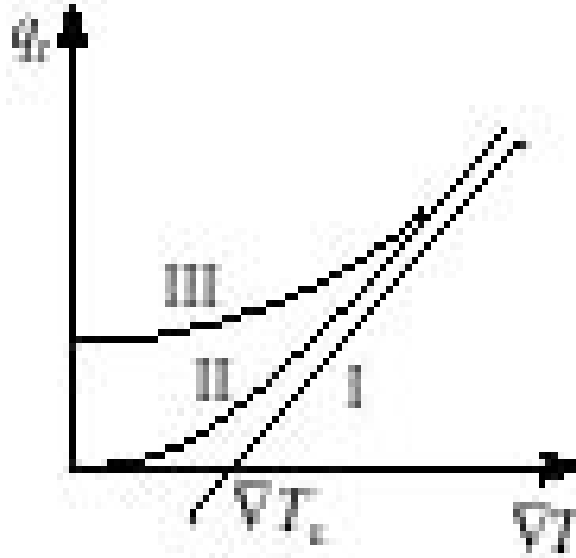


Figure 9.5: The three types of flux–gradient relations that arise in complex plasmas systems with off–diagonal transport diffusivities.

In the proper set of flux–driving gradient variables the transport matrix has Onsager symmetry [Shaing (1988), Sugama *et al.* (1996)]. The matrix is positive definite with  $D_{11}D_{22} - D_{12}D_{21} > 0$ . The positive definiteness of the matrices relating conjugate pairs of driving forces and transport fluxes is developed in detail by Sugama in a series of works on turbulent transport. In typical particle and power balance experimental studies of steady–state discharges the particle and thermal fluxes  $\Gamma$  and  $q$  are determined from the input source of particles and energy and the resulting measured profiles of  $n, T$  to infer the required diffusivities  $D_{ij}$ . For different signs of  $D_{12}$  there are three types of thermal flux versus temperature gradient relations that occur in plasmas as shown in Fig. 9.5. Type I shows a process of transport that starts above a critical gradient, in Type II processes the flux vanishes when the gradient vanishes, and in Type III the flux is finite when the gradient vanishes. The Type III flux occurs when the turbulence is driven by other gradients such as the ion temperature or electron density gradient for Ion Temperature Gradient (ITG) or Transmission Electron Microscopy (TEM driven fluctuations. Figure 9.5 shows these relationships schematically. The Type I flux gradient relation applies to ETG turbulent transport where one of the linear theoretical formulas gives critical gradient.

Consider the simple case shown in Fig. 9.5. For the positive electric potential structure in Fig. 9.5 the clockwise  $\mathbf{E} \times \mathbf{B}$  rotation brings higher density  $N_>$  (and higher pressure  $N_>T_e$ ) plasma to the right and lower density  $N_<$  (pressure) to the left resulting in a shift of the maximum density and potential, linked through the electron response by  $\delta n_e \cong n_e(e\varphi/T_e)$ , to the right. The speed of the translation is proportional to the gradient of the density  $L_n^{-1} = -\partial_r \ln N$  and inversely proportional to the strength of the magnetic field  $B$ . The speed also increases with electron temperature  $T_e$  since the potential fluctuation  $e\varphi$  scales up with  $T_e$ . For a negative potential structure the  $\mathbf{E} \times \mathbf{B}$  rotation is counter–clockwise, but the structure moves to the right with same

speed (in the limit of small  $e\varphi/T_e$ ) since now lower density plasma is brought to the right shifting the minimum in that direction. Now, the ion density at this location builds up in the time  $\delta t$  equal to that of the original electron maximum  $\delta n_e = N(e\varphi/T_e)$  when the condition

$$\delta n_i = -\frac{\delta t c \varphi}{B \delta y} \frac{\partial N}{\partial x} = N \frac{e\varphi}{T_e}, \quad (9.5)$$

is satisfied. In the last step we use quasineutrality, taking  $\delta n_i = \delta n_e = N(e\varphi/T_e)$  which is valid for fluctuations that are large compared to the Debye length. During the time  $\delta t$  the convection moves the maximum of the structure to the right by  $\delta y = v_{de} \delta t$  where

$$v_{de} = \frac{\delta y}{\delta t} = -\frac{c T_e}{e B N} \frac{\partial N}{\partial x}. \quad (9.6)$$

The  $x$ -displacement of the plasma during this motion is  $\xi_x = v_x \delta t = -\delta t \varphi / B \delta y$ . When this displacement becomes comparable to  $\delta x$  the motion is nonlinear leading to the formation of nonlinear vortex structures. Locally, the plasma is mixed over the length  $\delta x$  in one rotation period when the amplitude reach the mixing length level  $\xi_x = \int^t dt' v_{Ex} = \delta x = l_c$ . The nonlinear problem is treated in *Chaos and Structures in Nonlinear Plasmas* by Horton and Ichikawa (1996).

### 9.4.2 Drift wave diffusivities and the ion inertial scale length

It is conventional in the study of drift waves and transport to introduce gradient scale lengths and reference diffusivities. Thus, the length  $L_n$  is defined as the density gradient scale length through the relation  $1/L_n = -\partial_x \ln N$ . The temperature gradient scale length  $L_T$  is defined similarly. The spacetime scales of the waves lead to two different dimensional scalings for the plasma diffusivities. The reference diffusivities are the Bohm diffusivity

$$D_B = \frac{T_e}{eB}, \quad (9.7)$$

and the drift wave diffusivity

$$D_{dw} = \left( \frac{\rho_s}{L_n} \right) \left( \frac{T_e}{eB} \right), \quad (9.8)$$

also commonly called the gyroBohm diffusivity in reference to the factor  $\rho_s/L_n \ll 1$ . Here  $\rho_s = (m_i T_e)^{1/2} / eB$  is effective gyroradius parameters for hot electrons of  $T_e \gtrsim T_i$ . Clearly, the scaling of the Bohm and gyroBohm diffusivities are markedly different with  $D_B \propto T_e/B$  independent of the system size while  $D_{dw} = T_e^{3/2} / B^2 L$  decreasing with the system size.

In short, the Bohm (9.7) scaling arises from *mesoscale* drift wave structures  $\Delta x = (\rho_s L_T)^{1/2}$  and thus is expected near marginal stability [Horton, *et al.* (1994), Kishimoto, *et al.* (1996), Garbet and Waltz (1996), Lin, *et al.* (1998)]. With a minimal model of ITG, Ottaviani and Manfredi (1999) investigate the  $\rho_s$  scaling for a constant thermal flux through a turbulent annulus. They

observed an inverse cascade to larger elliptical vortices but find that the flux scaling remains gyroBohm.

When the convective cells size reduces to scale as  $\Delta x = \rho_s$  the drift wave diffusivity (9.8), commonly called gyroBohm, applies. In defining the dimensionless gyroradius parameter  $\rho_*$ , it is usual to replace the spacetime varying length  $L_n$  with the relatively constant value  $a$  of the plasma minor radius. Thus, a key issue is the scaling of plasma confinement with

$$\rho_* \equiv \frac{\rho_s}{a}. \quad (9.9)$$

[Waltz, *et al.* (1990), Perkins, *et al.* (1993)].

Drift wave theory is able to account for confinement scaling either as  $D_B$  or  $\rho_* D_B$ . Transport dependent on  $\rho_*$  depends on the average mass  $m_i$  of the working gas ions since  $\rho_s = (m_i T_e)^{1/2} / eB$ . The transition between the Bohm and the gyroBohm scaling is a difficult problem, both theoretically and experimentally, that has received considerable attention. Simulations by *Furnish, et al.* (1999) give one picture of the transition and those of *Lin, et al.* (1998) give the results of even larger and higher resolution simulations. Both authors report that there is a transition at certain values of  $\rho_*$  which measures the ratio of the microscale size to the global size of the system. The role of large scale computing in settling such issues is made clear by *Lin, et al.* (1998). On the experimental side of the scaling problem, the scaling studies of *Perkins, et al.* (1993), *Petty, et al.* (1995), and *Erba, et al.* (1995) present evidence for the Bohm-like scaling of the turbulent transport. More recent power balance studies in the JET discharge up to 7 MA of plasma current use a model that adds the Bohm and gyroBohm contributions. This is called the Joint European Torus Tokamak (JETTO) model and is now widely used in transport predictions [*Erba, et al.* (1998)]. Roughly the JETTO model is obtained with  $\chi_e = \alpha_e q^2 (a/L_p) D_B$  and  $\chi_i = \alpha_i x_e + \chi_i^{\text{neo}}$  with  $\alpha_e = 2.1 \times 10^{-4}$  and  $\alpha_i = 3.0$  [*Erba, et al.* (1995)]. Here  $1/q(r) = RB_\theta / rB_T$  gives the local pitch of the helical magnetic sideline.

The relevant system parameters for Tore Supra (TS) and the large Tokamak Fusion Test Reactor (TFTR) are given in Table 9.2. The fluctuation measurement at wave numbers  $k_\perp \lesssim 1 \text{ cm}^{-1}$  requires the techniques of reflectometry [*Doyle, et al.* (1991), *Mazzucato and Nazikian* (1993)] and the indirect method of beam emission spectroscopy as in the *Durst, et al.* (1993) experiment.



Table 9.2: Plasma Drift Wave Parameters for TFTR and Tore Supra

Machine	TFTR	TS
magnetic field	4.8 T	2.7 T
major/minor radii	2.45 m/0.80 m	2.30 m/0.75 m
electron temperature	6 KeV	5 keg
density $n_e$ and	$4.0 \times 10^{13} \text{ cm}^{-3}$	$3.6 \times 10^{13} \text{ cm}^{-3}$
gradient length $L_n$	20 cm	20 cm
drift velocity $v_d$	$3 \times 10^5 \text{ cm/s}$	$1 \times 10^5 \text{ cm/s}$
$k$ scattering experiment	$1\text{-}20 \text{ cm}^{-1}$	$1.5 - 15 \text{ cm}^{-1}$
$\omega$ scattering experiment	10-500 kHz	10-1000 kHz
to 0.02	0.01 to 0.1	

Finally, it is important to point out parallels with other areas of physics. The closest and most important parallel to plasma drift waves is the analogy with the Rossby waves and vortices in geophysical atmospheric and oceanographic disturbances with periods long compared to the rotational period of the planet. *Hasegawa and Mima* (1977, 1978) and *Hasegawa, et al.* (1979) develop the limit in which the two models become isomorphic. The correspondence is due to the Coriolis force having the same mathematical form as the Lorentz force. The analogy was also recognized by *Petviashvili* (1977) which led to the first rotating parabolic water tank experiments by *Antipov, et al.* (1982, 1985) in Kurchatov in 1983 in Tbilisi. This aspect of the drift wave Rossby problem is found in the *Horton and Hasegawa* (1994) article in the special issue of CHAOS devoted to such geophysical vortex structures. A recent high resolution simulation of geophysical vortex turbulence is in *McWilliams, et al.* (1999).

### 9.4.3 Resistive drift wave and interchange turbulence

The collisional drift wave is a paradigm for anomalous transport that has been extensively investigated with many different modelings. A particularly simple 2D-model, called the *Hasegawa-Wakatani* (1983) model with an adiabaticity parameter  $c\ell$  has been investigated by *Wakatani and Hasegawa* (1984), *Krommes and Hu* (1994), *Sugama, et al.* (1988), *Gang, et al.* (1991), *Koniges, et al.* (1992), *Biskamp, et al.* (1994), and *Hu and Horton* (1997). To understand the origin of the simple  $\alpha$  model and to appreciate its limits we briefly present the 3D resistive drift model. For finite resistivity  $\eta = m_e \nu_e / n_e e^2$  the parallel current carried by the electrons in Eq. (9.10) yields  $j_{\parallel} = -(n_e e^2 / m_e \nu_e) \nabla_{\parallel} (\varphi - T_e / e \ell n n)$  using the isothermal approximation  $\delta p_e = T_e \delta n_e$ . The collisional drift wave equation follows from the divergence of the current  $\nabla \cdot \mathbf{j} = 0$  with the divergence of the polarization current  $j_p$  balancing the divergence of  $j_{\parallel}$  through  $\nabla \cdot \mathbf{j}_p = -\nabla_{\parallel} j_{\parallel} = \eta^{-1} \nabla_{\parallel}^2 (\varphi - \frac{T_e}{e} \ell n n)$  and the electron continuity equation. In other words the dynamical equation for the field-aligned vorticity  $\zeta = \mathbf{b} \cdot \nabla \times \mathbf{v}_E = c \nabla_{\perp}^2 \varphi / B$  is given by the

conservation of charge in the quasineutrality limit. The rotational part of the plasma momentum for the vorticity  $\nabla^2\varphi$  is equivalent to the current closure equation. The vorticity equation and the electron continuity equation give, in dimensional form

$$\frac{m_i n c}{B_0} \frac{d}{dt} \nabla^2 \varphi = \frac{B_0}{c} \nabla_{\parallel} j_{\parallel} + \hat{\mathbf{z}} \cdot \nabla p_e \times \nabla \Omega, \quad (9.10)$$

$$\frac{d}{dt} (n_0 + n_1) = \frac{1}{e} \nabla_{\parallel} j_{\parallel} + \frac{c T_e n_0}{e B_0} \hat{\mathbf{z}} \cdot \nabla \left( \frac{n_1}{n_0} - \frac{e \varphi}{T_e} \right) \times \nabla \Omega, \quad (9.11)$$

where  $\nabla \Omega$  is the effective  $\mathbf{g}$ -force used to relate the curvature and gradient- $B$  effects to the classical Rayleigh–Taylor instability. The computation of  $\Omega(r)$  for the average curvature of the magnetic field line is extensively used in stellarator/heliotron research [Carreras, *et al.* (1987)]. The derivatives on the left side of Eqs. (9.10) and (9.11) are the  $\mathbf{E} \times \mathbf{B}$  convective derivatives defined by  $df/dt = \partial_t f + v_E \cdot \nabla f$ .

The coupled vorticity and density equations Eqs. (9.10) and (9.11) have a conserved potential vorticity  $\zeta$  given by

$$\zeta = \frac{m_i c^2}{e B^2} \nabla_{\perp}^2 \varphi - \ln n n_0 - \frac{n_1}{n_0} - \Omega, \quad (9.12)$$

which generalizes the conserved vorticity  $\nabla_{\perp}^2 \varphi$  in 2D Euler fluid. It is useful to first consider the dimensionless form of the model equations (9.10) and (9.11) in global coordinates before using the local drift wave units  $\rho_s$  and  $L_n/c_s$ . Using the minor radius  $a$  for the cross-field  $B_0 \hat{\mathbf{z}}$  dimensions, the major radius  $R$  for the dimensionless  $z/R \rightarrow z$  and time in units  $\omega_{ci} t (\rho_s/a)^2 \rightarrow t$  [equivalent to  $(c T_e / e B a^2) t \rightarrow t$ ], one finds that the natural amplitude variables are  $e \varphi / T_e = \varphi$  and  $n_1/n_0 = n$ , and the dimensionless parameters of the model are  $\epsilon = a/R$ ,  $\rho = \rho_s/a$ ,  $\nu = \nu_e/\omega_{ce}$ . The dimensionless model is then

$$\rho^2 \frac{d}{dt} \nabla_{\perp}^2 \varphi = \frac{\epsilon^2}{\nu} \nabla_{\parallel}^2 (n - \varphi) - g \frac{\partial n}{\partial y} + \mu \nabla^2 \varphi, \quad (9.13)$$

$$\frac{dn}{dt} = \frac{\epsilon^2}{\nu} \nabla_{\parallel}^2 (n - \varphi) + \partial_x \ell n n_0 \frac{\partial \varphi}{\partial y} - g \frac{\partial}{\partial y} (n - \varphi) + D \nabla^2 n, \quad (9.14)$$

where  $g = d\Omega/dr$ . This 3D model has resistive drift waves driven by the density gradient  $(\partial_x n_0)^2$  through the charge separation from finite  $k_{\perp}^2 \rho_s^2$  and the resistive interchange driven modes from  $\omega_* \omega_D > 0$  where  $\omega_D = (ck_{\theta} T / e B) (d\Omega/dr)$  is the averaged grad- $B$ /curvature drift frequency [Chen and Cheng (1980)]. The linear eigenmodes are of two types: localized to the rational surfaces where  $k_{\parallel} = 0$  and global modes [Sugama, *et al.* (1988), Hong, *et al.* (1991)].

The electric potential has the important property of developing an  $m = 0/n = 0$  component with a well-defined circular null surface. This  $\varphi_{0,0}(r, t) = 0$  surface partially blocks the turbulent losses from the core of the cylindrical model. For stellarators the  $m = 1, n = 1$  rational surface is near the edge of the plasma and the dominant modes in this simulation are the  $m = 3/n = 2$  and  $m = 2/n = 1$  fluctuations and the  $m = 0/n = 0$  background profile for  $v_{\theta} = -c E_r / B$ . These simulations with  $\nu_e / \omega_{ce} = 1.4 \times 10^{-4}$  are too collisional to apply to the edge of tokamaks with  $I > 1$  MA confinement devices (where  $\nu_e / \omega_{ce} \lesssim 10^{-6}$ ).

### 9.4.4 The impact of rational surfaces on radial heat transport in TJ-II

In this work, we study the outward propagation of temperature perturbations. For this purpose, we apply an advanced analysis technique, transfer entropy, to ECE measurements performed in ECR heated discharges at the low-shear stellarator TJ-II. We observe that the propagation of these perturbations is not smooth, but is slowed down at specific radial positions, near ‘trapping zones’ characterized by long time lags with respect to the perturbation origin. We also detect instances of rapid or instantaneous (nonlocal) propagation, in which perturbations appear to ‘jump over’ specific radial regions. The analysis of perturbations introduced in a resistive magnetohydrodynamic model of the plasma leads to similar results. The radial regions corresponding to slow radial transport are identified with maxima of the flow shear associated with rational surfaces (mini-transport barriers). The nonlocal interactions are due to the MHD mode coupling effects [van Milligen, *et al.* (2017)].

Wakatani, *et al.* (1992) extend the investigation of the model Eqs. (9.13)–(9.14) to include an externally-imposed electric field  $E_r(r)$  exceeding the strength of self-consistently generated field from the  $m = 0/n = 0$  modes. The  $E_r < 0$  field suppresses the turbulence during the growth phases, but produces only a weak reduction of the flux in the saturated state. The collisionality dependence of the particle flux is shown to increase with  $\nu_e$  for  $\nu/\omega_{ce} < 10^{-3}$  and then to increase as  $\nu_e^{1/3}$  for  $\nu/\omega_{ce} > 10^{-3}$ . The numerical treatment of the stabilizing role of sheared flows is subtle in that the problem of resolving the low- $k$  modes giving fluctuating sheared flow requires a high density of small  $k_y$  modes. Hallatschek (2001) has carried out convergence studies and concludes that often the role of shear flow damping of the turbulence is over estimated since the  $L_y$  box size is not taken large enough to have adequate resolution of the low  $k_y$  condensation of turbulent energy. With resistive interchange turbulence Hallatschek carries out high resolution simulations and finds a condition for sufficient density of the low- $k$  modes. The nature of this turbulence interaction with the shear flow is investigated for toroidal ITG modes by Li and Kishimoto (2002). These authors confirm earlier theoretical studies that show there is a bursting or intermittent nature to the shear generation through the turbulent Reynolds stress. Thus, the  $\chi_i$  and the level of the turbulence generated component of the sheared flows undergo relaxation oscillations controlled by the strength of the instability and the magnitude of the shear flow damping. This generation of zonal flows behavior persists but is much weaker for the short scale electron temperature gradient driven turbulence.

In the widely-investigated 2D model of the Hasegawa–Wakatani equations (9.13)–(9.14) the operator  $\nabla_{\parallel}^2 \rightarrow -\bar{k}_{\parallel}^2$  or  $-1/\mathcal{L}_c^2$ , where  $\bar{k}_{\parallel}$  is the relevant mean parallel wave number and  $\mathcal{L}_c$  is the connection length to the divertor end plates in the scrape-off layer (open field lines) modeling. For the interior tokamak field lines this reduction seriously limits the applicability due to losing the information on the closeness of the helical pitch of the magnetic field to the twists of the fluctuations following the toroidal direction. This resonance of the field pitch to that of the fluctuations is a key player in numerous effects including (1) the condensation of the turbulence to large-scale zonal flows described above and (2) the response of the density as adiabatic or MHD-fluid like. For 2D turbulence models the parameter  $c\ell = k_{\parallel}^2 T_e / m_e \nu_e \omega_0$  measures the parallel

electron diffusion in a characteristic wave period ( $1/\omega_0$ ).

The space–time units are changed to the local scales of  $\rho_s$  and  $L_n/c_s$  in these 2D studies. The standard form of the Hasegawa–Wakatani 2D model is then

$$\frac{d}{dt}(\nabla^2\varphi) = \alpha(\varphi - n) + \mu\nabla^4\varphi, \quad (9.15)$$

$$\frac{dn}{dt} = -\kappa\frac{\partial\varphi}{\partial y} + \alpha(\varphi - n) + D\nabla^2n, \quad (9.16)$$

where the viscosity  $\mu$  and  $D$  are taken small, but finite to absorb all fluctuation energy reaching the smallest resolved space scales in the simulation system. The system’s strong turbulence features at small  $\alpha$  with  $\alpha/\overline{\omega} \sim 1$  where  $\overline{k}, \overline{\omega}, \overline{\gamma}$  are taken at the peak of the energy spectrum. Here the overbar on  $k, \omega, \gamma$  denotes a mean value near the peak of the energy spectrum  $E_k$ . One can show that  $\overline{k} \approx \alpha^{1/3}, \overline{\gamma} \approx \alpha^{1/3}$  and that  $E_{\overline{k}} \simeq \overline{\gamma}^2/\overline{k}^3 \simeq 1/\alpha^{1/3}$  [Hu and Krommes (1994)]. In the large  $\alpha$  limit the density  $n \rightarrow \varphi(1 + \mathcal{O}(1/\alpha))$  approaches the adiabatic limit and a weaker turbulence appears with  $E_k \simeq \overline{\gamma}\overline{\omega}/\overline{k}^3 \approx 1/\alpha$  since  $\overline{\gamma} \sim 1/\alpha$ , and  $\overline{k} = \alpha^0$  and  $\overline{\omega} = \alpha^0$  independent of  $c\ell$ . These  $\alpha$ –scalings in the small- $\alpha$  and large- $\alpha$  regimes have been verified by direct numerical simulation and the statistical closure method.

In the quasi-2D equations (9.15)–(9.16), the parameter  $\alpha = k_{\parallel}^2 T_e / m_e \nu_e \omega_0$  determines the properties of the waves. For  $\alpha \gtrsim 1$  the electrons tend to the Boltzmann distribution  $\overline{n} = e\varphi/T_e$  and the Hasegawa–Mima equation is recovered. The Hasegawa–Mima equation is isomorphic with the Rossby wave equation for high Rossby number geostrophic flow in the mid-latitudes [McWilliams, *et al.* (1999)]. There is a strong dual cascade in this equation with anisotropy in the north–south or radial direction. The anisotropy leads to zonal flows.

Plasma turbulence appears as ubiquitous as plasma itself. In space, solar and astrophysical plasmas show many varied forms of plasma turbulence ranging from large-scale Magnetohydrodynamic (MHD) turbulence [Biskamp (1997)] to the smallest Debye length scale Langmuir turbulence. For example, the magnetic energy released during solar flares heats and accelerates the plasma in the solar corona. Electrons on the open coronal magnetic field lines caused by large scale MHD reconnection events stream at relativistic speeds into the interplanetary plasma. The electrons beams drive Langmuir turbulence creating intermittent bursts of radio noise known as Type III radio sources. The peculiar intermittency of Langmuir turbulence called nonlinear wave collapse was first described by Zakharov (1972). The phenomenon of nonlinear wave collapse is reviewed by Robinson (1997) for a wide range of laboratory and space physics settings. The general theoretical analysis of wave turbulence for plasmas and neutral fluids is given in Zakharov, *et al.* (1992).

We have developed, based on the oscillating-center transformation, a general theoretical approach for self-consistent plasma dynamics including, explicitly, effects of nonlinear (higher-order) wave–particle resonances. A specific example is then given for low-frequency responses of trapped particles in axisymmetric tokamaks. Possible applications to transport as well as nonlinear wave growth/damping are discussed [Chen and Zonca (2019)].

### 9.4.5 Short wavelength drift wave turbulence

Short wavelength fluctuations  $k_{\perp}\rho_i \gg 1$  with finite electron inertia are driven unstable by the electron temperature gradient. The modes are electron analogs of the better studied ion temperature gradient modes often called ITG modes. Their properties are developed in *Lee, et al.* (1987) and *Horton et al.* (1988). The short wavelength turbulence produces the electron thermal diffusivity given by

$$\chi_e = 0.3 \left( \frac{r}{R} \right)^{1/2} \frac{v_e}{R} \frac{c^2}{\omega_{pe}^2},$$

which explains the widely-observed  $\tau_E \propto n_E a^2 R$  scaling of the energy confinement time. Recently, there have been many simulation studies of the short wavelength turbulence to understand the coupling to the electromagnetic fluctuations that produce coherent structures on the scale of the collisionless skin depth  $c/\omega_{pe}$ . In typical tokamaks this length is order a few millimeters and is smaller than the standard drift-wave turbulence that is on the scale of several centimeters. The reason the smaller scale turbulence can compete in its ability to transport plasma is that the correlation times are smaller since the modes involve electron dynamics.

Studies of the electron transport in a spectrum of ETG electromagnetic waves shows the stochastization of the guiding center orbits and the rapid transport of the electron thermal energy [*Kim, et al.* (1990)]. Recent self-consistent field simulations include *Idomura, et al.* (2000), *Jenko, et al.* (2000, 2001), *Dorland, et al.* (2000), and *Li et al.* (2002). It is found that, unlike in the analogous case of ITG turbulence, the turbulent electron heat flux significantly exceeds the simple mixing length estimate, using the scale length that maximizes the growth rate. The mechanism is identified as the formation of highly elongated radial vortices (“streamer”), instead of zonal flows as in the case of ITG, when the perturbations develop nonlinearly. The streamers lead to effective cross-field transport while the zonal flows reduce it. This results in the discussion on the differences between ITG and ETG turbulence. The electromagnetic secondary instabilities in ETG turbulence are investigated in theoretical work of *Holland and Diamond* (2002). The possibilities of magnetic secondary instabilities (zonal magnetic fields and magnetic streamers) are found as novel potential mechanisms for electron transport regulation and enhancement, respectively. A crucial issue raised in these works is that of pattern selection for both ITG and ETG turbulence. That is, whether zonal modes or streamers are preferentially generated. These issues are open challenges to the magnetic fusion community.

A variational method is introduced to analyze the transmissivity of an electromagnetic wave propagating in the magnetized plasma sheath. The plasma density is modeled by two parabolic inhomogeneous regions separated by one homogeneous region. The Lagrangian density of the system is constructed based on the fluid energy density and the electromagnetic energy density. The total variation of the Lagrangian density is derived. The fluid and electromagnetic fields are numerically solved by expansion in piecewise polynomial function space. We investigate the effect of an external magnetic field on the transmissivity of the electromagnetic wave. It is found that the transmissivity is increased when an external magnetic field is applied. The dependence of transmissivity on the collision frequency between the electrons and the neutral particles has also

been studied. We also show that the external magnetic field causes a shift in the critical frequency of the plasma sheath [*Chen and Zonca* (2019)].

To understand the differences and possible correlation between the short wave length ( $k\rho_e \sim 1$ ) and the intermediate wave length ( $k\rho_i \sim 1$ ) instabilities and turbulence, the instabilities of continuous wavelength spectrum from the short to the intermediate are studied by *Smolyakov, et al.* (2002) and *Hirose, et al.* (2002). The unstable modes of  $k_y\rho_{i,e} > 1$  are identified as short wavelength ITG and ETG modes, respectively. In contrast to the conventional ITG and ETG modes, the new modes require both ion and electron temperature gradient higher than certain thresholds. In addition, the short wavelength modes in toroidal geometry require a minimum magnetic shear as a driving force. It is thought that the short wavelength ITG modes driven turbulences may induce higher electron thermal transport than the ETG turbulence does and, therefore, are responsible for the anomalous electron thermal transport experimentally observed.

The dependence of the critical temperature gradient on other plasma parameters such as temperature ratio ( $T_e/T_i$ ), magnetic shear and safety factor for toroidal Electron Temperature Gradient (ETG) instability is studied and formulas are given by *Jenko, et al.* (2001) and *Dong, et al.* (2002a,b). An interesting point from *Dong, et al.* (2002a,b) is that the critical electron temperature gradient increases from  $R/L_{Te} \sim 3$  to  $R/L_{Te} \sim 10$  dramatically when the temperature ratio  $T_e/T_i$  increases from 1/3 to 3. This is in great favor of  $\alpha$  particle heated burning plasmas as it is verified by future high  $T_e/T_i$  experiments. In addition, a brief estimate for ASDEX Upgrade and Tore Supra experiments [*Ryter, et al.* (2001a,b), *Hoang, et al.* 2001)] on the critical gradient is given and compared with the results from solving the integral eigenvalue problem for the ETG modes. The theoretical results are in the range of the experimental observations.

The electron thermal transport experiments on eight tokamak devices [Axially Symmetric Divertor Experiment (ASDEX-Upgrade), COMPact ASSEmbly (COMPASS-D), Frascati Tokamak Upgrade (FTU), Joint European Torus (JET), Tokamak Configuration Variable(TCV), Tore Supra (TS), Rijnhuizen Tokamak Project (RTP) and ASDEX Upgrade (AUG)] are summarized by *Ryter, et al.* (2001a). The critical gradients, above which the measured electron thermal diffusivity and the calculated growth rates of drift instabilities increase dramatically, are identified as  $R/L_{Te} \sim 8-12$  that falls right into the range of calculated critical electron temperature gradient for toroidal ETG instabilities by *Dong, et al.* (2002a).

Tokamak Fusion Test Reactor (TFTR) discharges with high core temperatures  $T_{e0} \lesssim 8$  KeV,  $T_{i0} \lesssim 25$  KeV from the improved confinement regime (enhanced reversed shear) and high neutral beam heating power (28 MW) has small scale fluctuations at  $k_\perp \cong 0.85\omega_{pe}/c \sim 5\rho_i^{-1} \simeq 9$  cm<sup>-1</sup> [*Wong, et al.* (1997)]. These electron density fluctuations  $\langle \delta n_e^2 \rangle_k$  are measured by scattering a microwave beam with  $|\Delta \mathbf{k}| = k_\perp = 8.9$  cm<sup>-1</sup> from the core plasma continuously in time. Power balance studies are then performed to determine the electron thermal diffusivity  $\chi_e(r, t)$  required to give the measured  $n_e, T_e(r, t)$  profiles from the fraction of the beam power deposited into the electrons. The resulting  $\chi_e(r, t)$  is shown to track the fluctuation level over a period of one second while  $\chi_e$  varies from 0.5 to 4 m<sup>2</sup>/s.

A related instability based on the electron inertial in the nonlinear Ohm's law and a single pressure field driving interchange instability in the unfavorable magnetic curvature is called the current diffusive ballooning mode. *Yagi and Horton* (1994) develop the properties of this

turbulence and derive the thermal diffusivity as

$$\chi = f(s) \frac{c^2 q^2 v_A}{\omega_{pe}^2 R} \left( -R \frac{d\beta}{dr} \right)^{3/2}$$

where  $f(s)$  is a complicated function of magnetic shear  $s$  obtained from the ballooning mode calculation of  $\langle k_x^2 \rangle$ . Evaluation of the current diffusive  $\chi$ , in the form given by *Fukuyama, et al.* (1994), is compared with a standard ITG transport model for a high-beta poloidal JT-60U discharge is given in *Horton, et al.* (1997).

The importance of the electron transport at the  $c/\omega_{pe}$  scale has been pointed out and investigated by many authors: *Ohkawa* (1978), *Kadomtsev and Pogutse* (1979), *Lee, et al.* (1987), *Horton, et al.* (1988, 1989, 1990, 2000), *Connor* (1993), *Itoh, et al.* (1994), *Fukuyama, et al.* (1994), *Idomura, et al.* (2000), *Hirose and Elia* (2002), *Holland and Diamond* (2002), and *Dong, et al.* (2002a,b). It is the current view that these fluctuations are the mechanism for electron thermal transport. If this is the case, then the electron fluctuations may be responsible for holding the electron temperature down in discharges where the ion confinement is improved dramatically. Low electron temperatures in the large D-T fusion experiments are one of the main reasons that those experiments fell short of expectations. Due to the importance of the electron turbulent transport, we discuss the Tore Supra experiments in the next section. Tore Supra has optimal plasma conditions for the study of turbulent electron transport.

#### 9.4.6 Tore Supra hot electron plasma transport data analysis

Tokamak discharges with core electron heating that dominates the ion heating provide valuable data for the transport regimes in a burning fusion reactor where alpha particle slowing down through electron collisions is the dominant heating power  $P_{\alpha e}$  [MW/m<sup>3</sup>] for thermal plasmas. The long-time steady-state discharges produced in Tore Supra with dominant, core localized electron heating provide a unique opportunity for the study of electron transport under conditions similar to burning plasmas in a tokamak fusion reactor. In general, Radio Frequency (RF) heating systems in Tore Supra provide flexibility for driving up the plasma temperature and of controlling plasma current profiles. The Fast Wave Electron Heating (FWEH) provides high-performance discharges with the largest increase of the core electron temperature over the ohmic temperature  $T_e^{\text{OH}}$ .

Fast Wave Electron Heating (FWEH) shows long plasma energy confinement times  $\tau_E$  [*Hoang, et al.* (1998)]. The universal feature of toroidal confinement arising from temperature gradient driven turbulence controlling the diffusivities is that the total electron stored energy  $W_e$  and the global energy confinement time  $\tau_E$  show a strong degradation as the total input heating power  $P$ , taken as the sum of ohmic and injected RF powers, increases. This behavior is shown in the standard empirical L-mode scaling law for the global energy confinement time as a function of the system parameters. A large international database supports the standard L-mode laws of tokamak operation. Improved confinement is then measured by defining the H-factor through the ratio  $H = \tau_E / \tau_E^L$ . Here H stands for “high confinement” and the H-factor is the ratio of the

improved  $\tau_E$  to the standard  $\tau_E^L$ . By varying current profile and peaking density profile tokamaks can achieve H-factor from 1.6 to 2.0 and even higher for special advanced operational scenarios.

For Tore Supra with FWEH, the discharge parameters range over  $2 \text{ MW} \leq P \leq 10 \text{ MW}$  with  $0.4 \text{ MA} \leq I_p \leq 0.9 \text{ MA}$  at two values of the toroidal magnetic field  $B_\phi = 2.0 \text{ T}$  and  $2.8 \text{ T}$ . The scaling results show that an improved confinement factor  $H \simeq 1.6$  is obtained when the global energy confinement time is compared with the ITER97-L-mode [Kaye (1997)] thermal energy confinement scaling law. The improved confinement arises from controlling magnetic shear through RF heating. The current profiles that produce low central magnetic shear and high outer confinement zone ( $\rho = r/a > 0.6$ ) shear produced the largest H-factors. The ETG thermal diffusivity  $\chi_e$  formula, based on the existence of critical electron temperature gradient, is shown to be consistent with the power balance  $\chi_e^{\text{PB}}$  when  $\nabla T_e$  exceeds the critical value  $(\nabla T_e)_{\text{crit}}$ , by a factor of two or more [Hoang, *et al.* (2001)]. There is clear evidence in both the power balance  $\chi_e$  and the measured density and magnetic fluctuations for a critical electron temperature gradient of about  $3 \text{ KeV/m}$  in the FWEH database. The critical gradient is observed to increase with magnetic shear and be independent of the magnetic field, that is consistent with what is known from electromagnetic drift wave theory [Horton, *et al.* (1988, 2000)]. The electromagnetic drift wave turbulence theory successfully interprets the high-power FWEH Tore Supra database of more than 40 well-documented discharges. The working gas is typically helium and the plasma pressure satisfies  $m_i \beta_e / m_e \approx 40$  at the mid-radius  $r = a/2$ . Thus,  $v_A \ll v_e$  and the drift wave is electromagnetic, with an associated  $\delta B_x / B \sim 10^{-5}$  fluctuation.

Gas spark gap is widely used in any pulsed power system as the key element which directly determines its repetitive performance and output characteristics. Among many factors of three-electrode gas spark gap, background pressure is of much importance in determining the gap performance parameters such as the delay and jitter, and relevant studies have been rarely performed. A magnetohydrodynamic model of the arc in gas spark gap is built and the effects of background pressure on the arc characteristics are discussed by Huang, *et al.* (2019). It is demonstrated that a higher background pressure may result in radial compression of the arc column, a higher arc voltage, and a lower declination rate of arc resistance in the first quarter cycle. Relevant simulation data would be helpful for the optimization of the design of gas spark gap [Huang, *et al.* (2019)].

#### 9.4.7 Electron transport theory

The existence of a broadband of drift wave fluctuations in Tore Supra is documented by the laser scattering experiments [Devynck, *et al.* (1993)]. The long wavelength end of the scattering measures the region of the ITG trapped electron spectrum while the short wavelength end measures the ETG type of turbulence. If one assumes that the modes are electrostatic in nature, then the stability analysis of Ross, *et al.* (1977) applies. One finds that the modes are unstable for both zero electron temperature gradient and for a finite electron temperature gradient. There is a strong increase of the short wavelength electrostatic growth rate with  $\eta_e$  that leads those authors to state that for  $\eta_e > 2/3$  the short wavelengths modes are strongly unstable. They search for



stabilization by including the ion-ion collisions.

In contrast, the ion temperature gradient is the dominant controlling parameter for the long wavelengths as is easily seen in the work of *Rewoldt and Tang* (1990). In that work the growth rate is shown to have a substantial value down to zero temperature gradient ( $\eta_i = \eta_e = 0$ ) for the long wavelength modes. The Rewoldt and Tang stability analysis is historically interesting in that it shows clearly the improved confinement properties of the proposed high-field burning plasma experiment called the Compact Ignition Tokamak (CIT). This same theme has emerged again and a new more advanced high field compact ignition tokamak is shown to lead to ignition in *Hu, et al.* (2002). Rewoldt and his collaborators show how the growth rates and ratios of the particle and thermal fluxes vary for a realistic tokamak model. Due to the renewed interest in the compact high-field ignition experiments a timely work to revisit is *Rewoldt and Tang* (1990) in which the growth rates were worked out for CIT tokamak. In this work they used MHD equilibria coupled with BALDUR transport values of  $\eta_i$  and  $\eta_e$  to study the collision and the  $\eta_i$  dependences of the complete matrix eigenvalue problem for coupled ITG and trapped electron modes. They found that the growth rates are greatly suppressed for the high-density regime of a compact ignition tokamak in their figures 1 and 2. For high densities, where the bounce frequency of trapped electrons is lower than the collision frequency, the growth rate threshold appears in  $\eta_i$  as in the classical adiabatic electron ITG theory. When the density is lowered to that typical of the standard 5 T field tokamaks like TFTR and JET, the drift waves remain unstable with a substantial growth rate even at zero values of the  $\eta_i$  parameter due the density electron temperature gradients. This is due to the wave changing to rotate in the electron diamagnetic direction and being destabilized with the trapped electron resonant wave interactions. The ballooning mode eigenfunctions are reported along with the ratios of the particle flux and the electron heat flux divided by the larger ion thermal flux. By taking these ratios of the turbulent fluxes the uncertainty in the amplitude of the fluctuations is reduced although not entirely eliminated due to the nonlinear shift of the spectrum to wavelengths longer than those that maximize the growth rate. The subject was studied again by *Dong, et al.* (1997). In toroidal collisionless high temperature plasmas, ITG and Trapped Electron (TE) modes are shown to be weakly (strongly) coupled when both the temperature gradients and the driving mechanism of the TE are moderate to strong (weak but finite). In the regime of strong coupling, there is a single hybrid mode unstable for all ITG in plasmas with positive magnetic shear. In the weak coupling case, two independent unstable modes, one in the ion and the other in the electron diamagnetic direction, are found to coexist. In either situation, a negative magnetic shear exerts a strong stabilizing influence; the stabilizing effect is considerably enhanced by the presence of trapped particles. Theory predicts that for plasmas of given parameters, it will be much hard to simultaneously excite the two modes in a toroidal magnetic field with negative shear.

In view of short wavelength theory and simulations, it is clear that these small scale modes are a key mechanism for producing the universally observed anomalous electron thermal losses in tokamaks that was found from the beginning of tokamak history [*Kadomtsev* (1992)]. We analyze the turbulent electron heat loss in Tore Supra (TS) under the hypothesis that the short wavelength electromagnetic fluctuations arise from the well-known mechanisms of the temperature gradient driven toroidal drift wave instabilities [*Horton, et al.* (1988, 2000)]. The overview of the drift-

wave fluctuation spectrum given in Fig. 6 in *Horton, et al.* (1988) and is evaluated here in detail for (TS) to show the multiple space–time scales. Four important wavelengths scales shown along the  $x$ -axis in that figure are computed for a typical Tore Supra plasma (TS shot # 19542).

Now we show the properties of these fluctuations in Tore Supra. Two of the characteristic cross-field wavelengths are given by the wave numbers  $k_y^m$  that maximize the linear theory growth rates  $\gamma_{k_y}^{\text{ITG}}$  and  $\gamma_{k_y}^{\text{ETG}}$  for the ion and electron temperature gradient driven instabilities respectively. The third major scale lengths corresponds to the wavelengths that mark the transition from the short scale  $\nabla T_i$  and  $\nabla T_e$  directly driven turbulence that is well described within the framework of quasi-two-dimensional plasma turbulence to the longer wavelength regime where the three dimensionality of the turbulence dominates.

The 2D to 3D transitional cross-field scale length is given by the conditions  $\omega_{*i} = k_{\parallel} v_i$  for ITG and by  $\omega_{*e} = k_{\parallel} v_e$  for ETG where  $k_{\parallel} = 1/qR$  is fixed by the toroidal geometry and  $q = rB_T/RB_{\theta}$ . The inverse cascade of the quasi-two-dimensional system is arrested at this  $k_{\perp}$ -scale since the fluctuations become intrinsically three-dimensional at this and larger cross-field scale lengths. The FLR fluid simulations [*Horton* (1990)] show that the  $k_y$  wavenumber spectrum changes shape, developing a flat local maximum at this transitional scale where  $k_{\perp} \simeq \ell_c^{-1}$ . Physically, it is clear that the nonlinear dynamics of fluctuations changes character when the time to propagate the ion or electron acoustic wave around the torus is shorter than the corresponding drift wave period. The nonlinear matrix elements for the mode coupling become dominated by  $k_{\parallel}^2$  rather than  $k_{\perp}^2$  when the turbulence scale satisfies  $k_{\perp} < \ell_c^{-1}$ . Evidently, high  $q$  extends the range of the quasi-two-dimensional turbulence producing a higher turbulent thermal diffusivity through the extended range of the inverse cascade  $\ell_c = qR/\triangle k_y L_t = q\ell_c R/L_T$ . Further discussion of this inverse cascade effect is given in *Ottaviani and Manfredi* (1999). With the inverse cascade ITG turbulence spectrum, two successful applications with interpretative simulations for discharges in the ITER profile database are reported by *Redd, et al.* (1997).

Subsequently, *Erba, et al.* (1999) confirm and extend these investigations. These inverse cascaded transport formulas are called the OHE (Ottaviani-Horton-Erba) model [*Ottaviani, et al.* (1997)] for the ion transport channel. Simulations of ETG show the same type of inverse cascade effect which appears generic to the  $\mathbf{E} \times \mathbf{B}$  convective nonlinearities. Thus the same type of formula larger than that from the mixing length estimate must be included in turbulent electron transport. For ETG there are two larger scales where the turbulent energy can accumulate. The electron transport driven by the ETG turbulence is less well verified than the ITG turbulence. An experiment supporting the role of the ETG turbulence is found in *Wong, et al.* (1997). The key formulas are that the maximum growth rate is given by

$$\gamma_{\text{max}}^{\text{ETG}} = \frac{v_e}{(L_{Te}R)^{1/2}}, \quad (9.17)$$

where  $v_e = (T_e/m_e)^{1/2}$ , and occurs at  $k_y \gg k_x$  with

$$k_y^m = \frac{1}{\rho_e} \left( \frac{1 - 2L_{ne}/R}{1 + \eta_e} \right)^{1/2}, \quad (9.18)$$

where  $\rho_e = v_e/\omega_{ce}$ . The electrostatic inverse cascade limit defines the electron mixing length  $\ell_{c,e}$  as

$$\ell_{c,e}^{es} = q\rho_e \frac{R}{L_{T_e}}. \quad (9.19)$$

The derivation of this electrostatic scale  $\ell_{c,e}$  applies for low plasma  $\beta_{pe}$ . For higher  $\beta_{pe}$  the collisionless skin depth  $\delta_e = c/\omega_{pe}$  is the relevant breakpoint in the spectrum. If we compare formula with  $\ell_{c,e}$  in Eq. (9.19) with

$$\ell_{c,e}^{em} = \delta_e = \frac{c}{\omega_{pe}}, \quad (9.20)$$

to find the critical  $\beta_e^{\text{crit}} = L_{T_e}^2/q^2 R^2$  or  $\beta_p^{\text{crit}} = 2L_{T_e}^2/a^2$  for the transition defined by  $\ell_{ce}^{es} = \ell_{c,e}^{em}$ . The experiments have  $\ell_{c,e}^{em} > \ell_{c,e}^{es}$  for  $r/a \lesssim 0.3$ . The scale length  $\delta_e$  in Eq. (9.20) arises from the solution of the fluctuating component of Ampere's law

$$\nabla_{\perp}^2 \tilde{A}_{\parallel} = -4\pi \tilde{j}_{\parallel}^e/c = 4\pi n_0 e \tilde{u}_{\parallel}/c, \quad (9.21)$$

as explained in *Horton, et al.* (1988). Here  $\tilde{u}_{\parallel}$  is the fluctuating parallel electron flow velocity. Three 3D partial differential equations are given and solved for simulations of the finite  $\beta_e$  ETG turbulence in *Horton* (1990). The results show that at the scale  $\rho_{c,e}$  the cross-field turbulence has become approximately isotropic in the  $x$ - $y$ -plane. The vortex or coherent structures are much larger than the electron gyroradius scale. The toroidal gyrokinetic simulations of *Idomura, et al.* (2000) reconfirm these findings of large-scale structures supporting large thermal fluxes.

The region between  $\ell_{c,e}$  and  $1/k_y^m$  is sufficiently large that we may look for a spectral index to roughly characterize this region. It is to be noted, however, that in general, there is some degree of linear growth and damping throughout  $\mathbf{k}$ -space so that Kolmogorov exponents are not strictly defined, since there are no source/sink-free transport regions in  $\mathbf{k}$ -space. For completeness we note that the corresponding ITG time-space scales are

$$\gamma_{\text{max}}^{\text{ITG}} = \frac{c_s}{(L_{T_i} R)^{1/2}} \quad (9.22)$$

$$k_y^m = \frac{1}{\rho_s} \left( \frac{1 - 2L_{n_i}/R}{1 + \eta_i} \right)^{1/2} \quad (9.23)$$

and

$$\ell_{c,i} = q\rho_s \frac{R}{L_{T_i}}. \quad (9.24)$$

Note that for flat density profiles where  $2L_n/R \rightarrow 1$  another formula applies for  $k_y^m$ . The derivation and interpretation of these time spaces is given in *Ottaviani, et al.* (1997), and *Redd, et al.* (1997). The ion temperature does not become high enough for finite ion  $\beta$  effect being important in those experiments. For plasma states well above the critical gradient for the instability the threshold is relatively unimportant and the turbulent diffusivities are given by

$$\chi_e = C_e \ell_{c,e}^2 \gamma_{\text{max}}^{\text{ETG}} \quad (9.25)$$

and

$$\chi_i = C_i \ell_{c,i}^2 \gamma_{\max}^{\text{ITG}}. \quad (9.26)$$

The coefficients  $C_i = 0.014$  from *Ottaviani, et al.* (1997) for a JET discharge and  $C_e = 0.1$  is determined by *Horton, et al.* (2000) for a Tore Supra discharge. The theoretical meaning of  $C_i$  and  $C_e$  is the fraction to which the ITG and ETG turbulence reach the levels given by the mixing length level of  $e\tilde{\varphi}/T_e \simeq \ell_C/L_T$ . The *Hoang, et al.* (1998) power balance studies indicate that magnetic shear  $s = rq'/q$  is an important parameter. Strong magnetic shear leads to electron Landau damping and is known to provide a threshold gradient above the adiabatic value. *Hoang, et al.* (1998, 2001) investigate the question as to the experimental evidence for the existence of a critical electron gradient  $(\nabla T_e)_c$ . *Hoang, et al.* (1998) found evidence for a critical electron temperature gradient near  $(\nabla T_e)_c \simeq 3 \text{ KeV/m}$  and attempted to correlate the  $(\nabla T_e)_c$  inferred from heating experiments with the *Rebut, et al.* (1991) model. Serious difficulties with the toroidal magnetic field dependence and magnetic shear independence of the RLW formula are reported. Thus the emphasis has changed to the thresholds for ITG and ETG turbulence. There are well-developed formulas for critical threshold gradients for the ITG and ETG turbulence since these values are from the linear dispersion relation.

Here we examine the effects of magnetic shear dependence of  $(\nabla T_e)_c$  formula. The resulting ETG electron diffusivity is

$$\chi_e^{es} = C_e^{es} q^2 \left( \frac{R}{L_{T_e}} \right)^{3/2} \left( \frac{c\rho_e}{eB} \right) \left[ \frac{T_e}{L_{T_e}} - C_L \left( \frac{|s|T_e}{qR} \right) \left( 1 + \frac{T_e}{T_i} \right) \right], \quad (9.27)$$

with two parameters  $C_e$  and  $C_L$ . Formula (9.27) is the straightforward generalization of the ion turbulent thermal diffusivity formula in OHE model to the electron turbulence. The dependence of Eq. (9.27) on  $q^2$  and  $R/L_{T_e}$  reproduces features shown in *Hoang, et al.* (1998) for  $\chi_e$  from power balance. The critical gradient also agrees in magnitude (few KeV/m) and in the observed increase of  $(\nabla T_e)_c$  with magnetic shear reported from both the power  $\chi_e$  and the fluctuation levels in Tore Supra. Documentation of the agreement between theory and electron power balance inferred values of the critical gradient are presented in *Hoang, et al.* (2001). For the core region of the discharge the electrostatic  $\chi_e$  in Eq. (9.27) transforms to an electromagnetic turbulent transport given by

$$\chi_e^{em} = C_e^{em} \frac{c^2}{\omega_{pe}^2} \frac{v_e}{(L_{T_e} R)^{1/2}} \quad \beta_{pe} > \beta_{\text{crit}}. \quad (9.28)$$

The independence of  $\chi_e^{em}$  on  $B_T$  appears strange but is explained by the requirements that  $\beta_e^{\text{crit}} = L_{T_e}^2/q^2 R^2 (\beta_{pe} > \beta_{pe}^{\text{crit}} \sim (L_{T_e}/a)^2)$  and  $q \geq 1$ . Analyzing the difficult region between the high- and low-beta regimes we find that a working formula to span the two regimes is given by

$$x_e^{em} = \frac{x_e^{es}}{[1 + (C_e^{es} \beta_e / C_e^{em} \beta_e^{\text{crit}})]}.$$

This composite formula has the same high and low beta limits and keeps the desirable property of reducing to the electrostatic gyroBohm scaling at low plasma pressure. This feature is necessary

in modeling the LHCD experiments where the density is low and use of Eq. (9.28) would yield too high a transport rate.

### 9.4.8 Theory comparison with power balance analysis

#### A reference Tore Supra (TS) shot

Here we analyze TS shot#19542 for the time interval  $t = 5.0\text{-}6.35$  due to the previous detailed study in *Hoang, et al.* (1998) and its availability on the ITER profile database. The plasma data at  $t = 6.0\text{ s}$  is shown characteristics of this  $0.685\text{ MA}/2.71\text{ T}$  discharge given in Table 9.3.

Table 9.3: Tore Supra (TS) High- $\beta_p$  Experiment #19542 at  $t = 6\text{ s}$

$R/a$	2.3 m/0.75 m
$B_\phi$	2.7 T
$I_p$	0.69 MA
$P_{\text{RF}}$	3.4 MW
$n_e(0)$	$3.6 \times 10^{19} \text{ m}^{-3}$
$T_e(0)/T_i(0)$	4.3 KeV/0.55 KeV
$n_D \tau_E T_e$	$3.7 \times 10^{18} \text{ m}^{-3} \cdot \text{s} \cdot \text{KeV}$
$v_\phi(0)$	-20 km/s

The profiles of the electron temperature  $T_e$ , ion temperature  $T_i$  and electron density are shown in Fig. 9.6.

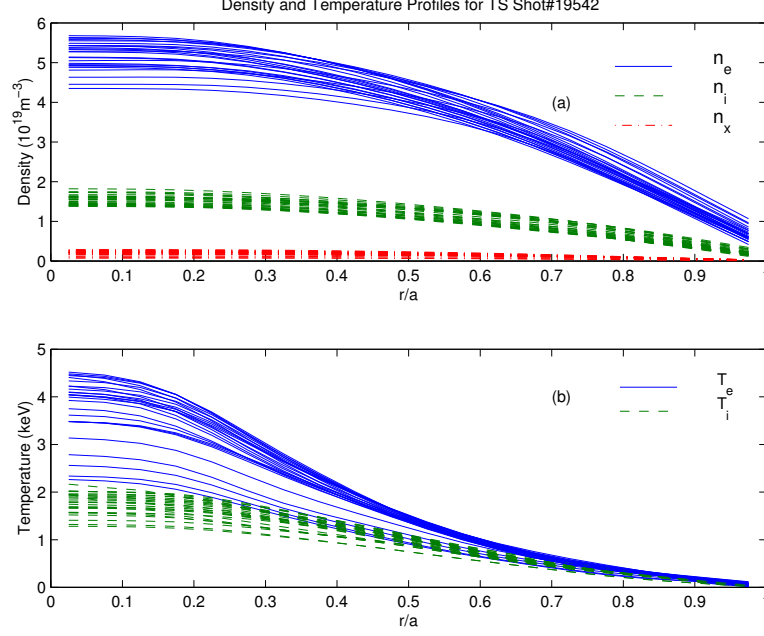


Figure 9.6: The (a) temperature and (b) density profiles from  $t = 5$  s to 6.35 s in Tore Supra shot # 19542. [Reprinted with permission from *Horton, et al.* (2000), Copyright 2002, American Institute of Physics].

The fast wave Radio Frequency RF heating power is absorbed by electron Landau damping ( $\omega^{\text{RF}} \simeq k_{\parallel}^{\text{RF}} v_e$ ) and is exponentially localized ( $P_e^{\text{RF}} \exp(-r/L_p)$ ) to the core of this discharge with the  $1/e$  width  $L_p = 4.3$  cm. In this discharge the net integrated power deposited is 3.4 MW. The strong localization of the deposited power is important for producing the high electron temperature gradient shown in Fig. 9.7 that reaches a maximum value of 12 KeV/m at  $\rho = r/a \simeq 0.3$ . Also, shown in Fig. 9.7 is the critical electron temperature gradient computed from Eq. (9.27). We see that in the core out to  $\rho \simeq 0.8$  the electron temperature gradient exceeds this critical gradient by a factor from 5 to 2 in going from  $\rho = 0.3$  to 0.8. Thus, in our first analysis we choose to compute the thresholdless  $\chi_e$  formula with one parameter  $C_e$  to the power balance  $\chi_e$ .

The steady-state power balance equations in the core plasma are

$$\frac{1}{r} \frac{\partial}{\partial r} (r q_e) = P_e^{\text{RF}} + j_{\parallel} E_{\parallel} - Q_{ei}, \quad (9.29)$$

$$\frac{1}{r} \frac{\partial}{\partial r} (r q_i) = P_i^{\text{RF}} + Q_{ei}. \quad (9.30)$$

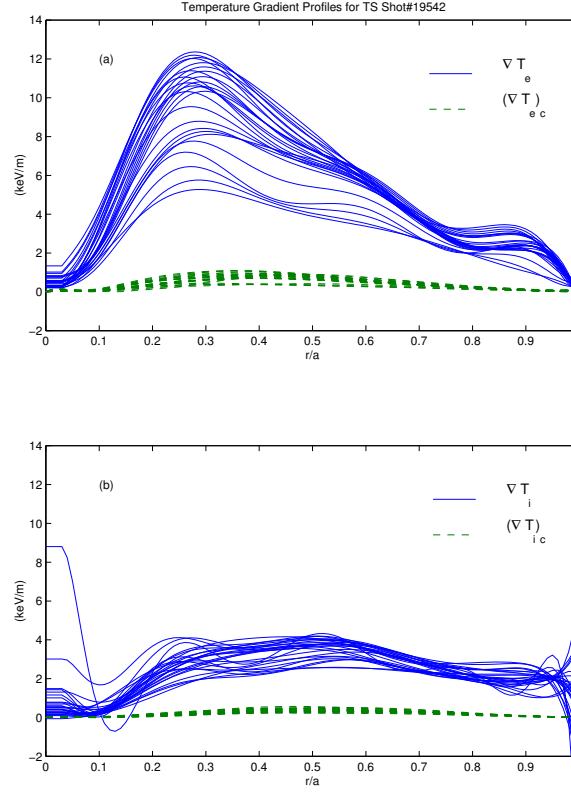


Figure 9.7: (a) The deposition profiles for the fast wave heating  $P_{\text{ICRHE}}(r)$  are highly peaked in the core as given in the  $U$ -files. The heating of the ions is from the electron-ion coupling  $Q_{ei}(r)$  with a small fraction from the fast wave heating. (b) The steady-state power balance heat fluxes. All the profiles are for  $t = 5$  s to 6.35 s in Tore Supra shot #19542. [Reprinted with permission from *Horton, et al.* (2002), Copyright 2002, American Institute of Physics].

Beyond  $\rho > 0.8$  the radiation losses in electron channel and the atomic physics processes in the ion channel may become dominant. Thus, we limit the transport analysis to  $\rho_1 < \rho < \rho_2$  typically choosing  $\rho_1 = 0.1$  and  $\rho_2 = 0.8$ . The electron-ion energy transfer term  $Q_{ei}$  is subdominant to  $P = P_e^{\text{RF}} + P_e^{\Omega}$ , but is the dominant input term in the ion power balance equation. More than 90% of the RF input power is coupled to the electron, and since  $T_e \gg T_i$ , the coupling  $Q_{ei}$  depends mainly on  $T_e$ .

The integration of Eqs. (9.29) and (9.30) from  $\rho = 0$  to  $\rho$  gives the power balance fluxes shown in Fig. 9.8.

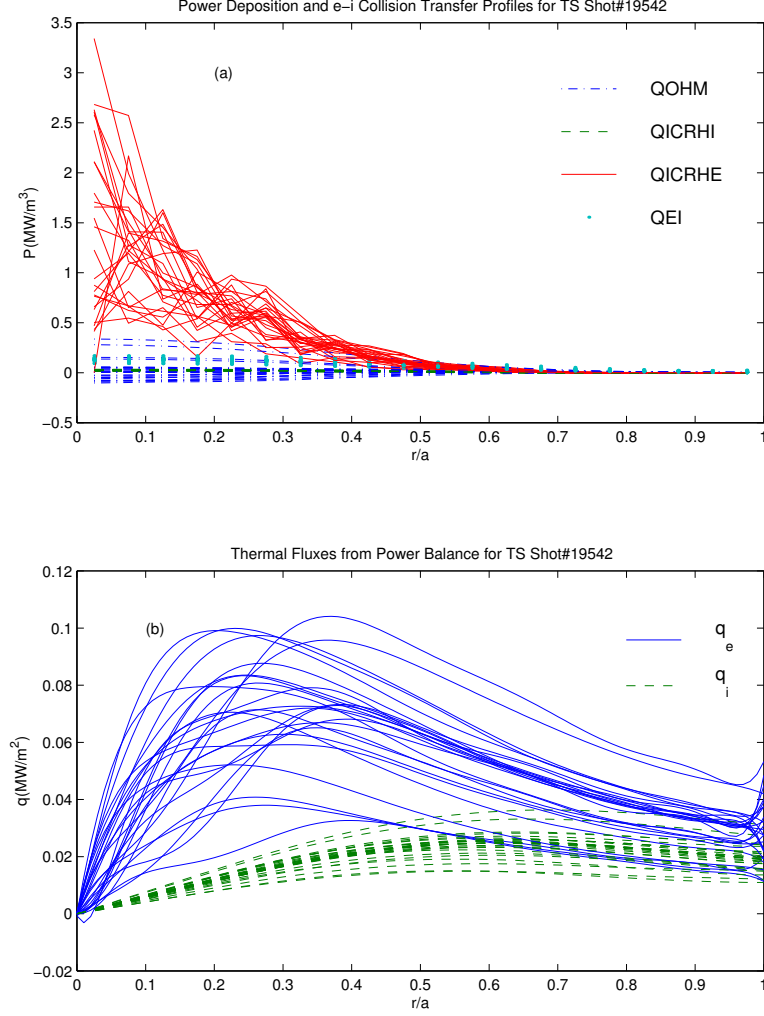


Figure 9.8: The profiles of the power deposition  $P(\text{MW/m}^2)$  and collisional transfer powers are shown in Fig. 9.8a and the radial profiles of the turbulent thermal fluxes  $q_e(r)$  and  $q_i(r)$  are shown in Fig. 9.8.

The peak flux  $q_e$  occurs at the edge of the FEWH deposition profile and then falls approximately as  $1/r$  until  $r/a \simeq 0.74$  where the lower temperature  $T_e$  provides a strong sink into the ion channel. The power balance thermal diffusivities are defined as

$$\chi_e^{\text{PB}} = -\frac{q_e}{n_e \left( \frac{dT_e}{dr} \right)} \quad (9.31)$$

$$\chi_i^{\text{PB}} = -\frac{q_i}{n_i \left( \frac{dT_i}{dr} \right)} \quad (9.32)$$

following Eq. (4) of *Hoang, et al.* (1998).



The values obtained for the power balance diffusivities (9.31) and (9.32) compared with the computations from Eqs. (9.26) and (9.27). In constructing this comparison we choose  $C_e$  and  $C_i$  by minimizing the mean-square deviation of the model  $\chi_S$  with the power balance  $\chi_S$ . The resulting values are  $C_e = 0.1$  and  $C_i = 0.015$  with the mean square deviations given by  $\sigma_{C_e} = 0.3$  and  $\sigma_{C_i} = 0.5$ . The value of the  $C_e$  is consistent with earlier theoretical estimates. The value of  $C_i$  is consistent with that value obtained for the JET shot # 19649, which is used in calibration of the OHE model [Ottaviani, *et al.* (1997)] to within the limits of the large errors in  $\chi_i$ . The Probability Distribution Functions (PDF) of  $\chi_e^{\text{expt}}/\chi_e^{\text{model}} = \chi_e^{\text{PB}}/\chi_e^{\text{em}}$  are not Gaussian, but have a skewness to large values of  $\chi_i^{\text{PB}}/\chi_i$  and  $\chi^{\text{PB}}/\chi_e^{\text{em}}$ . These heavy tails on the PDFs lead to the large values of  $\sigma_{C_e}$  and  $\sigma_{C_i}$ .

## Tore Supra-98 database

A database of approximately fifty discharges has been assembled and used for power balance analysis. The toroidal magnetic field  $B_\phi$  and plasma current  $I_p$  range from a minimum of 2.1 T/0.4 MA to a maximum of 2.8 T/0.9 MA. The electron density from  $1.2$  to  $5.2 \times 10^{19} \text{m}^{-3}$  with a range of mixture of deuterium and helium as working gas. The profiles of the power deposition  $P(\text{MW/m}^2)$  and collisional transfer powers are shown in Fig. 9.8a and the radial profiles of the turbulent thermal fluxes  $q_e(r)$  and  $q_i(r)$  are shown in Fig. 9.8.

For each of the independent time slices distributed over different TS shots, we obtain a coefficient  $C_e^{\text{es}}$  in Eq. (9.27) and a coefficient  $C_e^{\text{em}}$  in Eq. (9.28) by minimizing the square deviation between the model diffusivities and the ones obtained from power balance equations, as we did in the analysis of the reference shot in the previous section. In this way we get two distributions from the two sets of coefficients, with 48 samples in each for various values of  $\nu = 1$  and 2 in the exponent of  $q$  in  $\chi_e^{\text{es}}$  and  $\chi_e^{\text{em}}$  formulas. The mean square deviation of the data from the ETG model is minimized for  $\nu = 0$  to 1 for the  $\chi_e^{\text{em}}$  and  $\nu = 0$  for the  $\chi_e^{\text{es}}$  models, and  $C_e^{\text{em}}$  has much smaller relative deviation than  $C_e^{\text{es}}$  for all variations of  $\nu$ . The best fit values are  $C^{\text{em}} = 0.1$  and  $C^{\text{em}} = 0.15$  with error measure for the  $\chi_e^{\text{es}}$  more than twice that of the  $\chi_e^{\text{em}}$  formula. The results suggest that the electromagnetic turbulence formula [Eq. (9.28)] gives a better model for the turbulent electron thermal diffusivity, when only one correlation length formula is used. Predictive simulations have confirmed this suggestion as shown in Fig. 9.9.

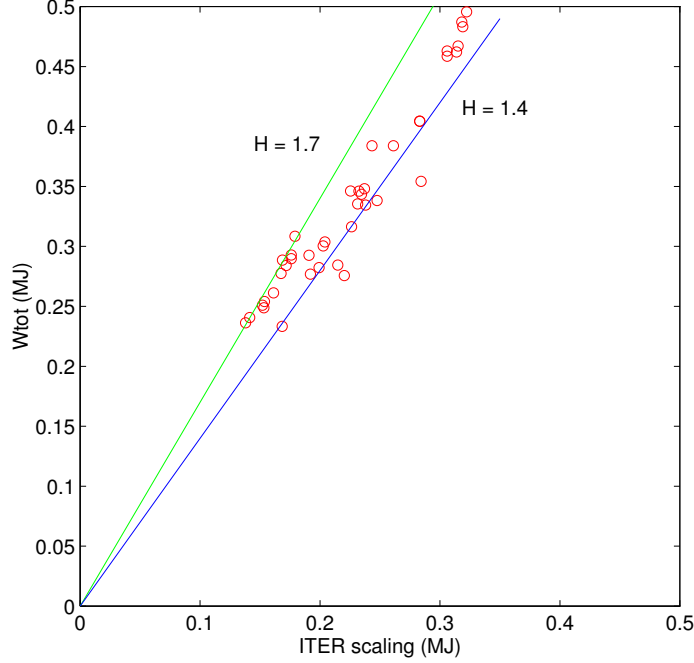


Figure 9.9: Comparison of the measured total plasma energy with the ITER-97 L-mode scaling prediction for the 48 Tore Supra shots. [Reprinted with permission from *Horton, et al.* (2000), Copyright 2002, American Institute of Physics].

In terms of global energy confinement time scaling, the electromagnetic  $\chi_e^{\text{ETG}}$  formula reproduces well the improved confinement which is essentially the H-mode equality. This is shown in Fig. 9.9, where the H-factor  $H = W^{\text{tot}}/W_L^{\text{tot}}$  of these discharges ranges between  $H = 1.4$  and  $H = 1.7$ . Here  $W_L$  is the ITER L-mode scaling [Kaye (1997)]

$$W_L^{\text{tot}} = 0.023 k^{0.64} R^{1.83} (R/a)^{0.06} I_p^{0.96} B_\phi^{0.03} \bar{n}_e^{0.40} M_{\text{eff}}^{0.20} P^{0.27}. \quad (9.33)$$

In contrast, we find that the low  $\beta_{pe}$ , electrostatic  $\chi_e^{\text{ETG}}$  formula predicts L-mode performance, which is too pessimistic for these discharges.

#### 9.4.9 Interpretive transport simulations

Now, we test the theory for the electron transport making simulations in the LOw COmplexity (LOCO) transport code in the interpretive configuration. By interpretive simulations one means transport runs on database shots with theoretical formulas used for  $\chi_e$  and  $\chi_i$  that yield the evolution of  $T_e(r, t)$  for the model to compared with the measured profiles. The comparisons are more demanding than the steady-state power balance since there is a ramp-up and ramp-down of the driving radio frequency heating power. For this model of electron thermal transport the

measured electron density is used in the simulation to eliminate uncertainties associated with the particle transport processes. Such runs allow one to interpret and assess the space-time evolution of the temperature profiles given by the theoretical electron thermal diffusivity formula. Here we show one comparison from the database that demonstrates well the accuracy to which the space-time evolution of the electron temperature profile is reproduced by the  $\chi_e^{\text{ETG}}$  formula. In *Horton, et al.* (2000) and *Hoang, et al.* (2001) many more discharges are analyzed and statistical distributions of the deviations between theory and the power balance inferred  $\chi_e$  are presented.

### Shot 18368, $I_p = 0.65 \text{ MA}$ , $P_{\text{ICRH}} = 3 \text{ MW} \rightarrow 6 \text{ MW}$

This Tore Supra discharge has a step-up over a period  $\Delta t = 0.5 \text{ s} (\sim 5\tau_E)$  from the RF power driving level of 3 MW to 6 MW shown in Fig. 9.10a.

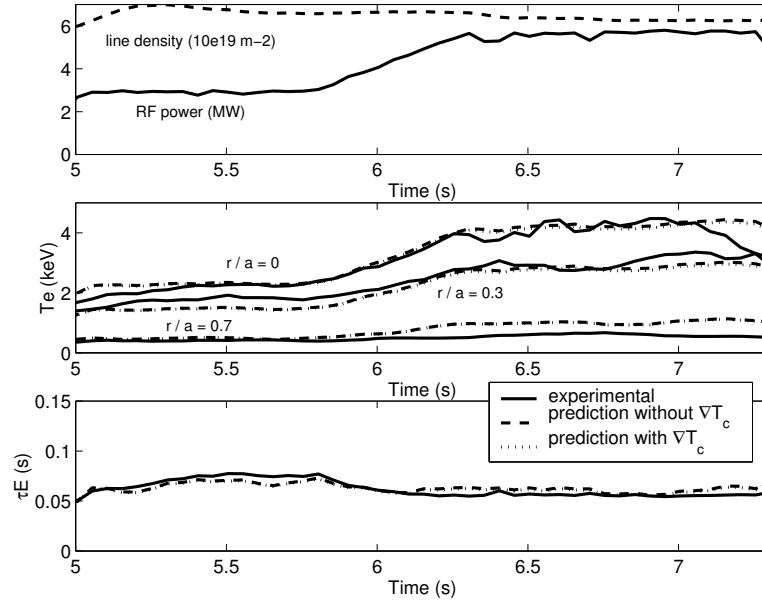


Figure 9.10: Interpretive simulation for shot 18368 in Tore Supra. (a) Applied FWEH heating ramp from 3 MW to 6 MW for  $\Delta t = 0.5 \text{ s}$  at  $t = 5.8 \text{ s}$ . (b) The rise and saturation of  $T_e$  at  $r/a = 0, r/a = 0.3$  and  $r/a = 0.7$  from the experiment (solid), and from the model without (dashed) and with (dotted) a critical gradient term. (c) Evolution of  $\tau_E$  from the experiment (solid) and from the model without (dashed) and with (dotted) a critical gradient term [Reprinted with permission from *Horton, et al.* (2000), Copyright 2002, American Institute of Physics].

The net stored electron energy increase from 0.2 MJ to 0.35 MJ with the model following closely the measured increase of electron thermal energy. The tracking of the modeled  $T_e$  profile at  $r/a = 0, 0.3$ , and  $0.7$  with the measured profile is shown in Fig. 9.10b. The model over-predicts the core temperature somewhat. There are some significant 100 ms oscillations on the

core temperature which are not in the model  $T_e$  and may account for the discrepancy. The model tracks the measured profile well at  $r/a = 0.3$  and  $0.7$  through the step-up in the RF power.

The top panel of Fig. 9.11 shows that the model prediction for the stored energy tracks well the measured stored energy over the step-up in the RF power. The core oscillations shows up as  $\Delta W_e \leq 50$  kJ excursions of the model  $W_e$  above that from the measured profiles for which  $\Delta W_e \leq 300$  kJ.

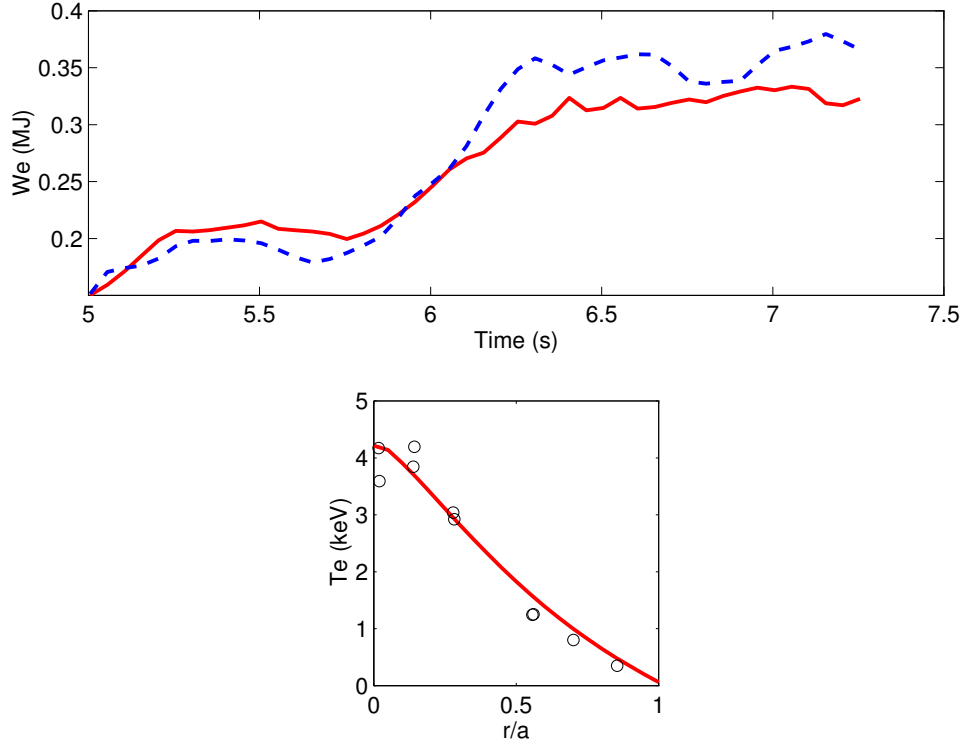


Figure 9.11: Interpretive simulation for shot 18368.(a) The stored electron energy  $W_e$ , from the experiment (solid) and from the simulations (dashed). (b) The temperature profile at  $t = 6.5$  s, from the experiment (circles) and from the simulations (solid). [Reprinted with permission from *Horton, et al.* (2002), Copyright 2002, American Institute of Physics.]

This and other similar interpretive simulations establish that the theoretical  $\chi_e$  model tracks well both the radial and time variations of the electron temperature profile in the RF heated plasma. The histograms for ratios of  $C_e = \chi_e^{\text{PB}}/\chi_e$  (model) are shown for the FWEH database of 48 shots in *Horton, et al.* (2000) and for a larger set of competing theoretical models in *Hoang, et al.* (2001). The conclusion is that the ETG transport formulas work well to provide a predictive tool for determining the electron temperature in tokamaks.

### 9.4.10 Summary of Tore Supra turbulent transport

The theoretical and experimental status of turbulent plasma transport in tokamaks is reviewed with an emphasis on the electron turbulent transport. The degree of the electron anomaly is the largest and, historically, the longest standing transport anomaly in the controlled fusion research program. We show that recent developments in theory and simulations allow the formula for  $\chi_e$  to be used and tested for confidence with steady-state electron data. While the best approach for describing turbulent transport is explicitly that of the multi-mode approach where all possible instabilities are assessed and applied as dictated by theory, we report here tests of the electron transport in plasma where the power flow is dominantly through the electron channel and thus most sensitive to the  $\chi_e$  formula.

The power balance analysis of the hot electron Tore Supra plasmas is unusually clear due to the direct, local deposition of radio frequency power into core electrons through the FWEH mode of operation. As a consequence, there is a multi-megawatt thermal flux conducting through the electron channel in the radial region from  $\rho = \rho_1 \simeq 0.2$  to  $\rho = \rho_2 \simeq 0.7$ . Since the electron temperature profile is accurately measured for these discharges there is a well-defined electron thermal diffusivity  $\chi_e$  called the power balance thermal diffusivity. The data analysis presented here shows clear evidence for the short scale length electron temperature gradient drift wave turbulence, providing a basic physics explanation for the mechanism producing the observed thermal diffusivity. This hypothesis is tested with transport codes with the local heating deposition profiles and edge boundary conditions given. The results show that the ETG formula is able to reproduce well the accurately-known electron temperature profiles. The theory gives that the turbulent correlation scale length changes character in going from the high electron pressure core to the lower pressure outer zone plasma. The degree to which the data supports the  $\chi_e$  formula based on the correlation lengths  $\ell_{c,e}^{em} = c/\omega_{pe}\ell_{c,e}^{es} \simeq q\rho_e R/L_{Te}$  is presented. The interpretation and predictions resulting from theoretical turbulence  $\chi_e$  formulas is then compared with the well-documented empirical formula based on the database — the Taroni-Bohm formula. The conclusion is that the electromagnetic turbulent electron thermal diffusivity explains well the power balance  $\chi_e^{PB}$ .

This explanation is consistent with the report of *Colas, et al.* (1998) that reports the presence and role of internal magnetic fluctuations on electron heat transport. The *Colas, et al.* (1998) transport analysis uses the internal magnetic fluctuations  $\delta B_r$  measured with cross-polarization scattering technique [*Zou, et al.* (1995)]. The magnetic turbulence at short wave length  $k_\perp = 12.6 \text{ cm}^{-1}$  is measured at  $r/a = 0.55$ . Power scans show that the intensity at this wavenumber and position increases as  $(\delta B_r/B)^2 \cong 10^{-8}(8\text{m}^{-1}/L_{Te})$  in experiments where  $\nabla T_e \leq 7 \text{ KeV/m}$ . The corresponding maximum electron thermal flux is  $0.1 \text{ MW/m}^2$  which exceeds considerably the values shown in Fig. 9.1 for shot TS19542 ( $t = 6 \text{ s}$ ). The  $\chi_e$  formulas used by *Colas, et al.* (1998) are not self-consistent collective electromagnetic field transport formulas: rather they are the test particle diffusivities of electrons in a given spectrum of purely magnetic fluctuations. More realistic test particle diffusivities for electrons are in *Kim, et al.* (1990), keeping both the electric fields and the magnetic fluctuations. The motion of electron guiding center is strongly influenced by both the electric and magnetic components of the fluctuations. For low fluc-

tuation levels the Coulomb collisional pitch-angle scattering and the electromagnetic drift wave fluctuation spectrum act together to determine the electron diffusion in tokamak geometries. In the low amplitude fluctuation limit, one recovers [Kim, *et al.* (1990)] the neoclassical banana-plateau diffusion coefficient. At the fluctuation levels given by the mixing length amplitudes, the anomalous transport formulas for the electron turbulent transport in Eqs. (9.26)–(9.27) are recovered.

## Momentum–energy transport from turbulence driven by parallel flow shear

The low-frequency  $\mathbf{E} \times \mathbf{B}$  turbulence driven by the shear in the mass flow velocity parallel to the magnetic field is studied using theory in a slab configuration with magnetic shear. Ion temperature gradient effects are taken into account. The eigenfunctions of the linear instability are asymmetric about the mode rational surfaces. Quasilinear Reynolds stress induced by such asymmetric fluctuations produces momentum and energy transport across the magnetic field. Analytic formulas for the parallel and perpendicular Reynolds stress, viscosity and energy transport coefficients are derived. Experimental observations of the parallel and poloidal plasma flows on TEXT–U are presented and compared with the theoretical models [Dong, *et al.* (1998)].

Since it was first studied in the early 1970s [Antipov, *et al.* (1982)] the instability driven by the cross-field gradient (shear) of the plasma mass flow velocity parallel to the magnetic field in an inhomogeneous plasma has been investigated extensively in fusion [Antipov (1985), Antonova (1983), Balescu (1988), Biskamp (1997), Biskamp, *et al.* (1994)] as well as in space plasmas [Burrell (1997), Carreras, *et al.* (1987)]. Such instability can be strongly driven by the neutral-beam injection in tokamak discharges. In addition, a strong gradient of the flow velocity may appear near the plasma boundary due to the presence of the limiter or divertor which is known to dramatically alter the plasma dynamics in the scrape off layer (the shadow of the poloidal limiter or the plasma divertor region) from that in the core bulk plasma. In space plasmas, high streaming velocities parallel to the magnetic field and rapid variation of the parallel flow velocity with the distance perpendicular to the magnetic field are measured in the plasma sheet boundary layer due to the solar wind on the plasma sheet [Carreras, *et al.* (1987), Chen (1965a)] create vortices and turbulence.

Such turbulence driving mechanisms are understood and the characteristics of the instability are well documented [Antipov, *et al.* (1982a, 1985), Antonova (1983), Balescu (1988), Biskamp (1997), Biskamp, *et al.* (1994), Burrell (1997), Carreras, *et al.* (1987), Chen (1965a)].

In this section the emphasis is not on the study of the instability itself but rather on momentum and energy fluxes described by the turbulence induced Reynolds stress. From the Reynolds stress parallel and perpendicular to the magnetic field we determine the associated viscosity and energy transport coefficients generated by the turbulence of the instability. The transport coefficients are characterized both by their magnitude at the mixing length level of the turbulence and by their dimensionless ratios, the Prandtl numbers.

It was first observed on the TEXT tokamak [Chen and Sen (1995)] that a poloidal flow shear is formed at the plasma edge. Such flow shear may suppress or enhance the plasma density fluctuations changing affect the local plasma confinement. Later, the L-mode to H-mode (L-H) transition in tokamak plasma confinement was found to be related to the presence of the poloidal flow shear near the plasma edge [Chen and Cheng (1980)]. Theoretical work was carried out to study the poloidal flow shear effect on the plasma turbulence [Colas, *et al.* (1998)].

Several possible sources for the generation of such poloidal flow shear have been proposed [Connor (1993), Devynck, *et al.* (1993), Dimits, *et al.* (2000), Dong, *et al.* (1997), Dorland, *et al.* (2000), Doyle, *et al.* (1991)]. Among them two models are widely studied. One is the particle losses caused by the interaction with the limiter or divertor [Connor (1993), Devynck, *et al.* (1993)]. An alternative explanation is the Reynolds stress produced by the turbulence in the plasma [Dimits, *et al.* (2000), Dong, *et al.* (1997)]. This latter mechanism requires a physical driving force for the turbulence. A few physical models such as drift-resistive ballooning mode [Dorland, *et al.* (2000)], resistive pressure-gradient driven mode [Doyle, *et al.* (1991)] have been proposed and studied.

The parallel velocity shear, combined with the ion temperature gradient, is proposed as the driving mechanism for the poloidal sheared flow. It has been pointed out by several authors [Dimits, *et al.* (2000), Doyle, *et al.* (1991)] that there must be a symmetry breaking mechanism such as boundary conditions in drift waves, or some symmetry breaking seed introduced in the study of pressure-gradient driven turbulence in order to generate nonzero Reynolds stress from the fluctuations. One of the features for the model proposed is that the mode eigenfunction is intrinsically asymmetric about the mode rational surface so that the Reynolds stress generation is independent of, or at least not sensitive to, boundary conditions. Symmetry breaking seeds are not needed in the nonlinear simulations [Biskamp, *et al.* (1994)].

Experimental measurements of the parallel and poloidal flows were carried out on Texas Experimental Tokamak Upgrade (TEXT-U) and some of the results are presented. The measurements from a Mach probe show that there is a strong radial gradient of the parallel ion mass flow at about the same region as the poloidal shear layer. The sharp spatial gradient may be created and maintained by the transition from a confined interior plasma to a scrape-off layer plasma regulated by the cold plasma sheath surrounding the limiter. The sheath condition on the net parallel plasma electric current requires the build up of a parallel ion velocity to a fraction of the ion acoustic speed. The turbulence is now driven by the free energy associated with the radial gradient of the parallel flow velocity, and in turn, produces an acceleration in the poloidal direction. The preliminary evidence that the plasma parallel velocity changes at about the same radial position as the poloidal shear layer supports this scenario for the poloidal shear flow generation. The theoretical results are compared with and shown to be in reasonable agreement with the experimental observations if a neoclassical damping mechanism is introduced to balance the driving force from the Reynolds stress.

In large tokamaks the toroidal velocity gradients are measured by spectroscopic techniques and may be driven in the interior by parallel beam injection. In the analysis of the high poloidal beta discharge regime on JT-60U [Durst, *et al.* (1993)], a transport barrier is reported at the  $q = 3$  surface where the toroidal velocity gradient, measured in terms of the dimensionless sta-

bility parameter defined here, has a value close to that found in the TEXT-U scrape-off layer. We speculate that same physical processes proposed here for local confinement improvement on TEXT-U is involved in the transport barrier generation on JT-60U plasma.

In Sec. 9.4.11 the physics in the shear flow model is described, and the eigenmode equation is given and solved analytically. Analytic formulas for the Reynolds stress are derived in Sec. 9.4.12 and the numerical evaluations are presented in Sec. 9.4.13. In Sec. 9.4.14 the experimental observations on TEXT-U are described and the correlation of the theoretical results with these experiments are discussed in detail.

### 9.4.11 Physics model and eigenmode equation

Consider a slab magnetic configuration  $\mathbf{B} = B_0(\hat{\mathbf{z}} + \frac{x}{L_s}\hat{\mathbf{y}})$ , where  $L_s$  is the scale length of magnetic shear. Here the  $x$ -,  $y$ -, and  $z$ -directions in the sheared slab geometry are defined as the radial, poloidal and toroidal directions in the tokamak configuration. Theory is used to describe the ion motion and the electrons are adiabatic. Equilibrium parallel velocity shear  $dv_{\parallel}(x)/dx = \text{const}$  is first considered and ion temperature gradient ( $\eta_i$ ) effects are included in the instability. The perturbed electrostatic potential is expressed as  $\tilde{\phi}(x, y, t) = \text{Re}\{\phi(x) \exp(ik_y y - i\omega t)\}$ . Under these assumptions it is straightforward to derive the linear eigenmode equation for the function  $\phi(x)$  as follows,

$$\frac{d^2\phi(x)}{dx^2} - b_s\phi(x) + \frac{1 - \hat{\omega}}{\hat{\omega} + K}\phi(x) + \left[ \frac{s^2 x^2}{\hat{\omega}^2} - \frac{\hat{v}'_{0\parallel} s x}{(\hat{\omega} + K)\hat{\omega}} \right] \phi(x) = 0, \quad (9.34)$$

where  $b_s = k_y^2 \rho_s^2$ ,  $\hat{\omega} = \omega/\omega_{*e}$ ,  $K = (1 + \eta_i)/\tau$ ,  $\tau = T_e/T_i$ ,  $\eta_i = d \ln T_i / d \ln n$ ,  $\omega_{*e} = k_y \rho_s c_s / L_n$  is the electron diamagnetic frequency,  $x$  is normalized to  $\rho_s = c_s / \Omega = (T_e / m_i)^{1/2} / \Omega = c(m_i T_e)^{1/2} / eB$ ,  $\Omega$  is the ion gyrofrequency. The flow shear and magnetic shear are  $\hat{v}'_{0\parallel} = L_n dv_{\parallel} / c_s dx$ ,  $s = L_n / L_s$  with  $L_n$  being the density gradient scale length. Here  $T_e$  and  $T_i$  are the electron and ion temperature, respectively. Equation (9.34) is valid in the hydrodynamic-like limit and the full kinetic equation is also given in Ref. 4.

The dispersion relation obtained from (9.34) is

$$\left[ -b_s + \frac{1 - \hat{\omega}}{\hat{\omega} + K} - \frac{\hat{v}_{0\parallel}^2}{4(\hat{\omega} + K)^2} \right] \frac{\hat{\omega}}{is} = 2n + 1. \quad (9.35)$$

The corresponding eigenfunction is

$$\phi^{(n)}(x) = \phi_0^{(n)} \frac{\hat{\omega}}{is} H_n(is/\hat{\omega})^{1/2}(x + \Delta) e^{-is(x+\Delta)^2/2\hat{\omega}}, \quad (9.36)$$

where  $H_n$  is the Hermite function of order  $n$  and

$$\Delta = -\frac{\hat{v}'_{0\parallel} \hat{\omega}}{2s(\hat{\omega} + K)}. \quad (9.37)$$



It is easy to notice that the mode growth rate is independent of the sign of  $\widehat{v}'_{0\parallel}$  from Eq. (9.35). However, the asymmetry element, the shift  $\Delta$  of the position of the maximum  $\phi^{(0)}(x)$  from the mode rational surface ( $x = 0$ ), depends on the sign of  $\widehat{v}'_{0\parallel}$  and is important for the Reynolds stress calculation. For cold ion approximation ( $K \rightarrow 0$ )  $\Delta$  is a real shift in  $x$ -space. In general  $\Delta$  is complex and introduces a deformation of the eigenfunction given by  $\text{Re}\{\phi^{(n)}(x) \exp(ik_y y - i\omega t)\}$  as well as a shift in the frequency.

### 9.4.12 Equations for the Reynolds stress

The general expression for the perturbed electrostatic potential is  $\widetilde{\phi} = \text{Re}\left\{\sum_{k_y} \phi_0 \phi(x) \exp(-i\omega t + ik_y y)\right\}$ . The  $\mathbf{E} \times \mathbf{B}$  drift velocity is

$$\widetilde{v}_x = -\frac{c}{B} \frac{\partial \widetilde{\phi}}{\partial y}, \quad \widetilde{v}_y = \frac{c}{B} \frac{\partial \widetilde{\phi}}{\partial x}, \quad (9.38)$$

where  $B$  is the toroidal magnetic field and  $c$  is the speed of light. In the representation of  $\widetilde{\phi}$  we use  $\phi_0$  to characterize the rms fluctuation level and  $\phi(x)$  the normalized wave function structure.

Now we introduce the two components of the micro-Reynolds stress that measure the radial flux of the parallel and perpendicular momentum,

$$\pi_{xy}(x) = \widetilde{v}_x^* \widetilde{v}_y + \widetilde{v}_x \widetilde{v}_y^*, \quad (9.39)$$

$$\pi_{x\parallel}(x) = \widetilde{v}_x^* \widetilde{v}_{\parallel} + \widetilde{v}_x \widetilde{v}_{\parallel}^*, \quad (9.40)$$

where in the quasilinear approximation  $\widetilde{v}_{\parallel} = (\text{esc}_s/T_e \widehat{\omega}) x \widetilde{\phi}$ . In writing Eqs. (9.39) and (9.40) we leave implicit the summation over all poloidal mode numbers and all rational surfaces determined by the toroidal mode number spectrums. It is straightforward to obtain the analytic expressions for Eqs. (9.39) and (9.40), using Eqs. (9.36) and (9.37), as

$$\pi_{xy} = |\phi_0|^2 \frac{c^2}{\rho_s B^2} \frac{2k_y}{s} (2x \widehat{\omega}_r + \Delta \widehat{\omega}^* + \Delta^* \widehat{\omega}) e^{is[\widehat{\omega}(x+\Delta^*)^2 - \widehat{\omega}^*(x+\Delta)^2]/2|\widehat{\omega}|^2}, \quad (9.41)$$

$$\pi_{x\parallel} = |\phi_0|^2 \frac{cc_s e}{BT_e} \frac{x}{s} (-2k_y \gamma) e^{is[\widehat{\omega}(x+\Delta^*)^2 - \widehat{\omega}^*(x+\Delta)^2]/2|\widehat{\omega}|^2}, \quad (9.42)$$

where  $*$  stands for complex conjugate,  $\widehat{\omega}_r$  and  $\gamma$  are the real and imaginary part of  $\widehat{\omega}$ , respectively. For energy transport we need the radial flux  $q_x(x)$  of the ion pressure fluctuation

$$q_x(x) = \widetilde{v}_x^* \widetilde{p} + \widetilde{v}_x \widetilde{p}^* = |\phi_0|^2 \frac{P_0(1 + \eta_i)c^2}{\rho_s c_s B^2} \frac{2\gamma k_y}{s^2} e^{is[\widehat{\omega}(x+\Delta^*)^2 - \widehat{\omega}^*(x+\Delta)^2]/2|\widehat{\omega}|^2}, \quad (9.43)$$

where again we use the quasilinear approximation  $\tilde{p} = -\tilde{v}_x dP_0/i\omega dx$  for the perturbation of the pressure. Here  $P_0$  is the equilibrium pressure and the equilibrium pressure gradient is  $dP_0/dx \equiv -KP_0/L_n$ .

All the quantities given in Eqs. (9.8)–(9.10) are function of  $x = r - r_0$  with  $r_0$  being the position of the mode rational surface. In order to obtain the effects of these quantities on the macro-motion, or background motion, these micro-fluxes that are localized to small layers around the resonant surfaces ( $x + \Delta = 0$ ) must be integrated over  $x$ . The results are the corresponding values used in the macro-motion equation on the mode rational surface. In this way we have

$$\langle \pi_{xy} \rangle = \int_{-\infty}^{+\infty} (\tilde{v}_x^* \tilde{v}_y + \tilde{v}_x \tilde{v}_y^*) dx = -|\phi_0|^2 \frac{c^2 k_y}{B^2 \rho_s} \sqrt{\pi} |\hat{\omega}|^3 K \tilde{v}'_{0\parallel} s^{5/2} \gamma^{1/2} |\hat{\omega} + K|^2 e^{\gamma \tilde{v}_{0\parallel}^2 K^2} 4s |\hat{\omega} + K|^4, \quad (9.44)$$

$$\langle \pi_{x\parallel} \rangle = \int_{-\infty}^{+\infty} (\tilde{v}_x^* \tilde{v}_{\parallel} + \tilde{v}_x \tilde{v}_{\parallel}^*) dx = -|\phi_0|^2 \frac{cc_s e}{BT_e s^{5/2}} \sqrt{\pi} \frac{k_y \gamma^{1/2} |\hat{\omega}|^3 \tilde{v}'_{0\parallel}}{|\hat{\omega} + K|^2} e^{\gamma \tilde{v}_{0\parallel}^2 K^2 / 4s |\hat{\omega} + K|^4}, \quad (9.45)$$

and

$$\langle q_x \rangle = \int_{-\infty}^{+\infty} (\tilde{v}_x^* \tilde{p} + \tilde{v}_x \tilde{p}^*) dx = |\phi_0|^2 \frac{P_0(1 + \eta_i) c^2 (\pi \gamma)^{1/2} |\hat{\omega}| k_y}{\rho_s c_s B^2} \frac{e^{\gamma \tilde{v}_{0\parallel}^2 K^2 / 4s |\hat{\omega} + K|^4}}{s^{5/2}}. \quad (9.46)$$

In Eqs. (9.44)–(9.46) the mode growth rate  $\gamma$  and real frequency  $\hat{\omega}_r$  must be obtained from the mode dispersion equation (with  $\hat{\omega} = \hat{\omega}_r + i\gamma$ ), for each  $k_y$  and the mean fluxes summed over all  $k_y$ . Apparently,  $\langle \pi_{xy} \rangle$  and  $\langle \pi_{x\parallel} \rangle$  vanish linearly with  $\tilde{v}'_{0\parallel} \rightarrow 0$  while  $\langle q_x \rangle$  does not. Considering that the ion temperature gradient is taken into account, the instability is still possible under such limit. This clearly shows the importance of the parallel velocity shear for the momentum transport from turbulence.

With this presentation of  $\langle \pi_{xy} \rangle$ ,  $\langle \pi_{x\parallel} \rangle$ , and  $\langle q_x \rangle$  we are giving the intensity of the fluxes for the fluctuations at the specified  $k_y$ . The complete flux is then the integral of the intensity over the spectral distribution of the fluctuations  $\int I(k_y) dk_y$ . When one scale dominates the fluctuation spectrum it is adequate to take  $\phi_0^2$  as the rms amplitude and choose  $k_y$  corresponding to the dominant scale.

In integrating the micro-fluxes over  $x$  we obtain the transport across a single rational surface at  $r_0$ . To obtain the total flux across the sheared magnetic field, we must introduce the density of the rational  $\rho_{k_y}(r) = (6|q'|/\pi^2 q^2) k_y(r)$  surfaces and define  $\langle \pi_{xy} \rangle = \sum_{k_y} \int \rho_{k_y}(r) \pi_{xy} dr$ . Note that  $\rho_{k_y}(r)$  varies only on the scale of  $q(r)$  and is then essentially constant over the shear flow layer and the mode width. The total fluxes is given by the integrated formulas Eqs. (9.44)–(9.45) multiplied by the function  $\rho_{k_y}(r)$  and summed over all  $k_y$ . Here we give the flux per unit of these weighting factors. The momentum transport coefficients  $\mu_{\perp}$  and  $\mu_{\parallel}$  are defined by

$$\mu_{\perp} = \frac{\langle \pi_{xy} \rangle}{-\frac{dv_{\parallel}}{dx}} = |\phi_0|^2 \frac{c^2 k_y (\pi)^{1/2} |\hat{\omega}|^3 K L_n}{c_s B^2 \rho_s s^{5/2} \gamma^{1/2} |\hat{\omega} + K|^2} e^{\gamma \tilde{v}_{0\parallel}^2 K^2 / 4s |\hat{\omega} + K|^4}, \quad (9.47)$$

and

$$\mu_{\parallel} = \frac{\langle \pi_{x\parallel} \rangle}{-\frac{dv_{\parallel}}{dx}} = |\phi_0|^2 \frac{ce k_y (\pi)^{1/2} |\widehat{\omega}|^3 L_n \gamma^{1/2}}{B T_e s^{5/2} |\widehat{\omega} + K|^2} e^{\gamma \widehat{v}_{0\parallel}'^2 K^2 / 4s |\widehat{\omega} + K|^4}. \quad (9.48)$$

The energy transport coefficient  $\chi$  is defined as

$$\chi = \frac{\langle q_x \rangle}{-\frac{dP_0}{dx}} = \frac{L_n}{P_0(1 + \eta_i)} \langle \widetilde{v}_x^* \widetilde{p} + \widetilde{v}_x \widetilde{p}^* \rangle = |\phi_0|^2 \frac{c^2 L_n |\widehat{\omega}| k_y (\pi \gamma)^{1/2}}{c_s B^2 \rho_s s^{5/2}} e^{\gamma \widehat{v}_{0\parallel}'^2 K^2 / 4s |\widehat{\omega} + K|^4}. \quad (9.49)$$

The transport coefficients  $(\mu_{\perp}, \mu_{\parallel}, \chi)$  are proportional to the square of the fluctuation level  $\langle \phi^2 \rangle$ . It is important to consider the ratio of the coefficients for which the dependence on  $\phi$  is removed. The ratios of the energy transport coefficient to the momentum transport coefficients are,

$$\frac{\chi}{\mu_{\perp}} = \frac{\gamma |\widehat{\omega} + K|^2}{|\widehat{\omega}|^2 K} \quad (9.50)$$

$$\frac{\chi}{\mu_{\parallel}} = \frac{|\widehat{\omega} + K|^2}{|\widehat{\omega}|^2}. \quad (9.51)$$

The ratios in Eqs. (9.50) and (9.51) are the reciprocal of the perpendicular and the parallel Prandtl numbers for the turbulent plasmas. The approximate solution for the dispersion equation can be written as

$$\gamma \simeq \frac{sK}{1 - \frac{\widehat{v}_{0\parallel}'^2}{4K}} \quad (9.52)$$

if  $\frac{1}{2} |\widehat{v}_{0\parallel}'| \leq sK$ , which is generally true in tokamak plasmas. In this parameter regime we have the turbulent thermal diffusivity

$$\frac{\chi}{\mu_{\perp}} \sim \frac{1 - \frac{\widehat{v}_{0\parallel}'^2}{4K}}{s} + sK^2,$$

and

$$\frac{\chi}{\mu_{\parallel}} \sim \frac{\left(1 - \frac{\widehat{v}_{0\parallel}'^2}{4K}\right)}{s^2} + 1.$$

The comparison with the Prandtl numbers for Coulomb collision plasma are given in Sec. 9.4.13.

### 9.4.13 Evaluation of the transport coefficients

The dispersion equation (9.35) is solved numerically. Typical mode growth rates and frequencies are shown in Fig. ???. The reference parameters are  $s = 0.1, b_s = 0.1$ , and  $\tau = 1$ . In Fig. ???a the mode growth rate is shown as function of  $\widehat{v}_{0\parallel}' = L_n dv_{\parallel} / c_s dx$  for  $\eta_i = 0.5, 1.0, 1.5$ , and  $2.0$ .

A variety of drift-type instabilities relevant to toroidal magnetic fusion devices, including the trapped electron modes by *Prager, et al.* (1974), the trapped ion instability by *Slough, et*

*al.* (1981), the collisionless curvature driven trapped particle mode by *Scarmozzino, et al.* (1986) have been produced and identified in the Columbia Linear Machine.

The drift wave driven by the radial ion temperature gradient in a collisionless cylindrical plasma was demonstrated in the modified Columbia Linear Machine (CLM) by *Sen, et al.* (1991) by using biased wire screens to create a  $T_{i\parallel}(r)$  gradient sufficient to excite an  $m = 2, 10$  kHz (in the plasma frame) drift wave oscillation. The toroidal ITG mode driven by the magnetic curvature was also produced and identified by *Chen and Sen* (1995) in the same machine.

It is clear in the figure that there are two regimes for the mode development. In the first regime, where  $\widehat{v}'_{0\parallel} \sim 1$  and the growth of the mode is dominated by the ion temperature gradient, the mode growth rate increases slowly with  $\widehat{v}'_{0\parallel}$ . In the second regime, where  $\widehat{v}'_{0\parallel} \sim 2$  and the growth of the mode is dominated by the parallel velocity shear, the mode growth rate increases rapidly with  $\widehat{v}'_{0\parallel}$ . The approximate mode growth rate is given by Eq. (9.19) in the first regime. The higher the  $\eta_i$  value [deeper  $T_i(r)$  profile or flatter density profile  $n(r)$ ] or the lower the  $\tau$  value (lower  $T_e$  or higher  $T_i$ ), the flatter the curves  $\gamma$  versus  $\widehat{v}'_{0\parallel}$ .

In the second regime the approximate solution of the dispersion equation (9.35) is

$$\widehat{\omega} = \frac{1}{2(1+b_s)} \left\{ 1 - is + \left[ (1 - is)^2 - (1 + b_s) \widehat{v}_{0\parallel}^{\prime 2} \left( 1 - \frac{2K(1 + b_s)^{1/2}}{i|\widehat{v}'_{0\parallel}| + 1} \right) \right]^{1/2} \right\} \quad (9.53)$$

if  $K$  is small compared with  $|\widehat{v}'_{0\parallel}|$ . For small magnetic shear Eq. (9.52) gives

$$\gamma \simeq \frac{1}{2(1+b_s)^{1/2}} \left( |\widehat{v}'_{0\parallel}| - \frac{K+s}{|\widehat{v}'_{0\parallel}|} \right). \quad (9.54)$$

The mode real frequency exhibits two flat regimes and a transition regime. The higher the  $\eta_i$  value the larger the difference between the two flat regimes. Generally speaking, the mode rotates in the ion diamagnetic direction and frequency increases with  $\widehat{v}'_{0\parallel}$ . The frequency in the laboratory frame is Doppler shifted from what is given here where  $v_{\parallel}(x=0) = 0$ .

The microturbulence Reynolds stress  $\pi_{xy}$  without the factor  $|\phi_0|^2 c^2 / \rho_s B^2$  is plotted in Fig. 9.12 as function of  $x$  for  $\eta_i = 1, \tau = 1, b_s = 0.1$ . In Fig. 9.12(a)  $s = 0.1$  and  $\widehat{v}'_{0\parallel} = -1.5, -1.0, -0.5$  and  $0.0$ . It is easy to see that  $\pi_{xy}$  is antisymmetric about the  $x = 0$  surface for  $\widehat{v}'_{0\parallel} = 0$  and that the asymmetry develops dramatically with the increasing of  $|\widehat{v}'_{0\parallel}|$ . In addition, the magnitude of the micro-Reynolds stress  $\pi_{xy}$  increases significantly with  $|\widehat{v}'_{0\parallel}|$ . In Fig. 9.12(b)  $s = 0.5$  and  $\widehat{v}'_{0\parallel} = -1.5, -0.5, 0.5$ , and  $1.5$ . Comparison of the two cases with  $\widehat{v}'_{0\parallel} = -1.5$  shows that the asymmetry is higher while the amplitude is lower for  $s = 0.5$  than that for  $s = 0.1$ .

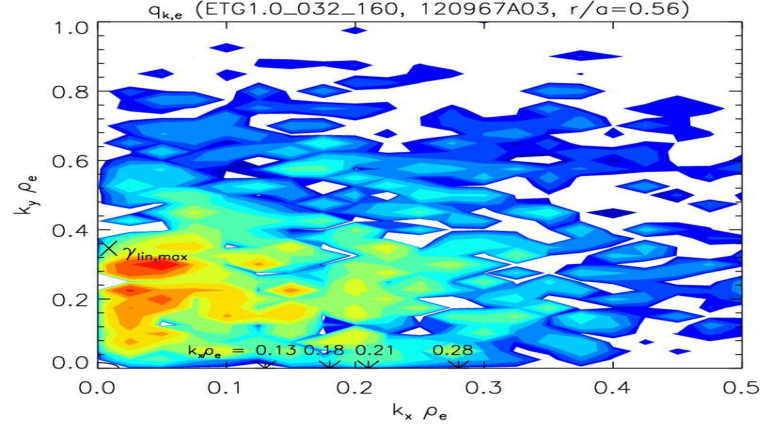


Figure 9.12: Diffusivity from Heat Flux  $q$  divided by local temperature gradient.

The Reynolds stress  $\langle \pi_{xy} \rangle$  [Eq. (9.47)] without the factor  $|\phi_0|^2 c^2 / \rho_s B^2$  is given in Fig. 9.13 as function of  $\widehat{v}'_{0\parallel}$  for  $\tau = 1, b_s = 0.1$ . In Fig. 9.13(a)  $\eta_i = 1.0, s = 0.1, 0.2, 0.3$ , and  $0.4$ . It is shown that for the same  $\widehat{v}'_{0\parallel}$ ,  $|\langle \pi_{xy} \rangle|$  decreases with the magnetic shear  $s$ , and that for all the  $s$  values studied here the Reynolds stress increases with the parallel velocity shear  $|\widehat{v}'_{0\parallel}|$ . The sign of  $\langle \pi_{xy} \rangle$  is opposite to the sign of  $\widehat{v}'_{0\parallel}$ . In Fig. 9.13(b)  $s = 1, \eta_i = 2, 3, 4$ , and  $5$ . It is seen that  $|\langle \pi_{xy} \rangle|$  increases with the increasing of  $\eta_i$  for  $\widehat{v}'_{0\parallel} \leq 1.5$  where the ion temperature gradient is the dominant driving force. For  $\widehat{v}'_{0\parallel} \sim 2$  it is the opposite,  $|\langle \pi_{xy} \rangle|$  increases with the decreasing of  $\eta_i$ .

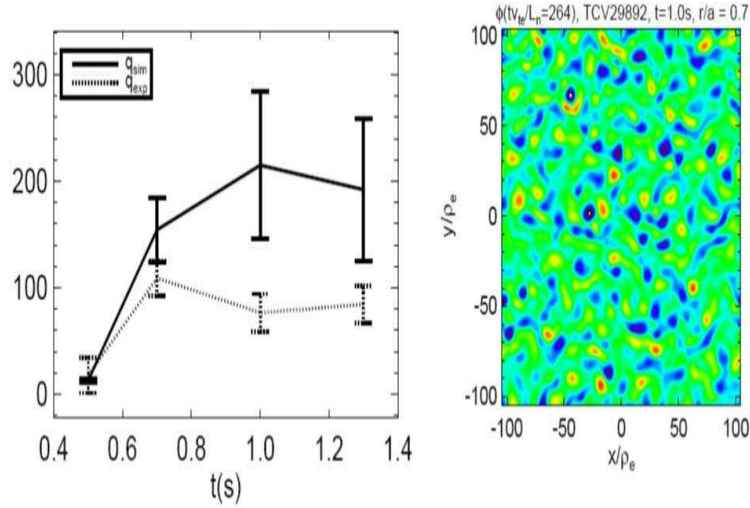


Figure 9.13:  $\chi_e$  from Modulated ECH in Frascati Tokamak FTU Analysis supports ETG transport.

The micro-Reynolds stress  $\pi_{x\parallel}$  without the factor  $|\phi_0|^2 c c_s e / B T_e$  as function of  $x$  is plotted in Fig. 9.14 for  $\tau = 1, b_s = 0.1, s = 0.1$ . In Fig. 9.14(a)  $\eta_i = 1, \widehat{v}'_{0\parallel} = -1.5, -1.0, -0.5$ , and  $0$ .

Similar to  $\pi_{xy}$ , the stress  $\pi_{x\parallel}$  is inversely symmetric about the  $x = 0$  surface when  $\widehat{v}'_{0\parallel}$  and such symmetry breaks as long as  $\widehat{v}'_{0\parallel} \neq 0$ . In Fig. 9.14(b)  $\widehat{v}'_{0\parallel} = -1.5$ ,  $\eta_i = 1, 2, 3$ , and 4. Both the amplitude and the asymmetry of  $\pi_{x\parallel}(x)$  increase with parallel velocity shear  $|\widehat{v}'_{0\parallel}|$  as well as with the ion temperature gradient  $\eta_i$  for the parameters studied here.

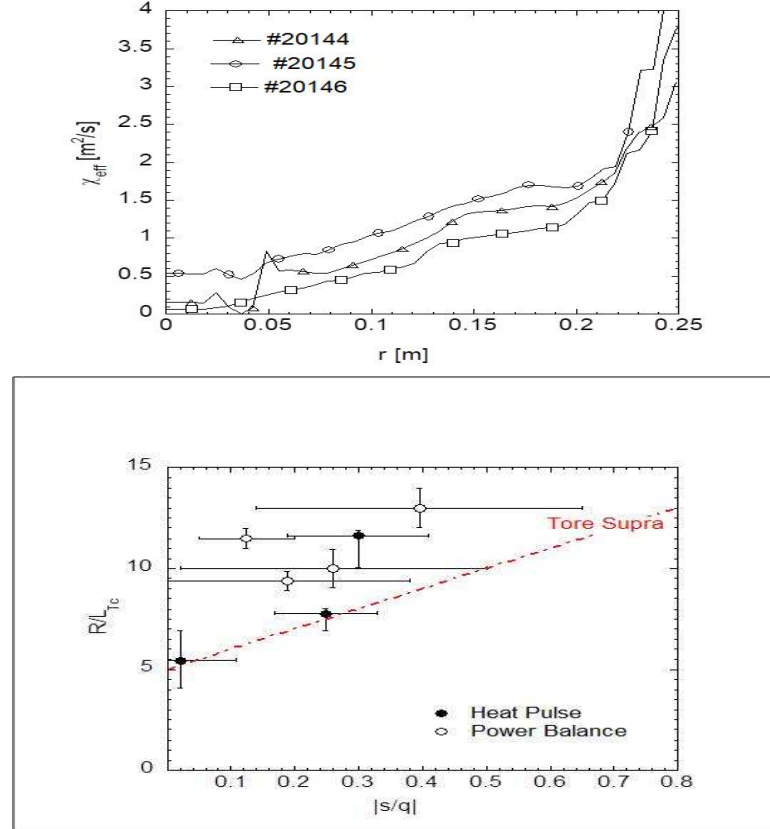


Figure 9.14: Reduction of fluctuation is well correlated with improved confinement. High- $k$  scattering shows significant level of turbulence that remains without ITG turbulence [ (XXXX)].

The Reynolds stress  $\langle \pi_{x\parallel} \rangle$  [Eq. (9.48)] is plotted as function of parallel velocity shear  $\widehat{v}'_{0\parallel}$  in Fig. 9.15 for  $\tau = 1, b_s = 0.1$ . In Fig 9.15(a)  $s = 0.1$ ,  $\eta_i = 2, 3, 4$  and 5. The Reynolds stress  $\langle \pi_{x\parallel} \rangle$  increases with the increasing of  $\eta_i$  for  $|\widehat{v}'_{0\parallel}| \gtrsim 1.5$ . For  $|\widehat{v}'_{0\parallel}| \gtrsim 2$  it decreases while  $\eta_i$  increases. In Fig. 9.5(b)  $\eta_i = 3, s = 0.1, 0.2, 0.3$  and 0.4. The Reynolds stress  $\langle \pi_{x\parallel} \rangle$  increases when the magnetic shear  $s$  decreases. For  $\eta_i \sim 1$  the Reynolds stress  $\langle \pi_{x\parallel} \rangle$  is not sensitive to the magnetic shear  $s$ . In addition,  $\langle \pi_{x\parallel} \rangle$  has the opposite sign to the flow shear  $\widehat{v}'_{0\parallel}$ .

*Reduction of fluctuation is well correlated with  
improved confinement*

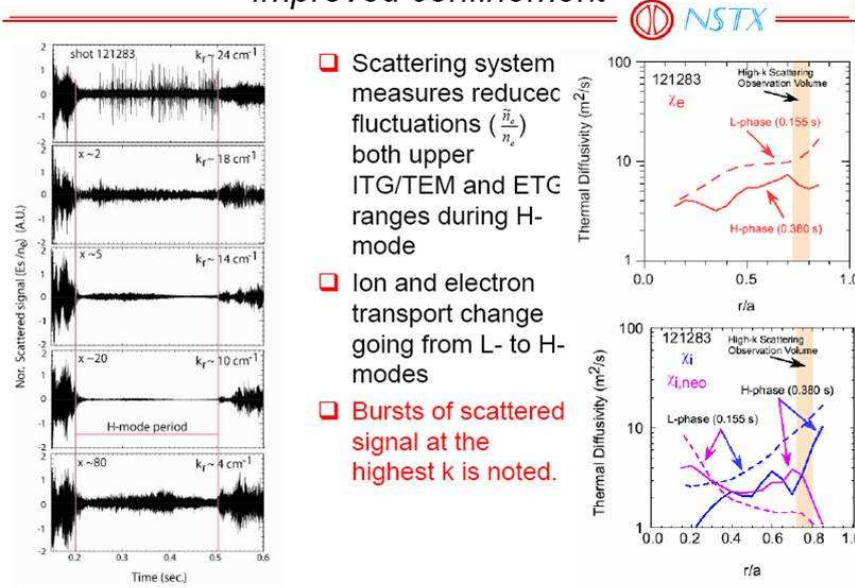
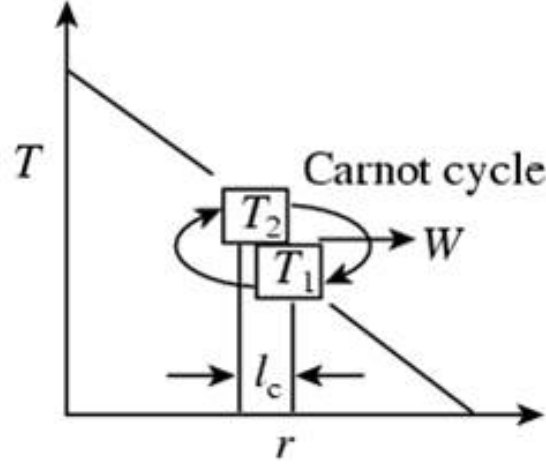


Figure 9.15: Record shot with D-D with equivalent  $Q$  for  $-T$  (factor 220 in n/s) of  $Q_{\text{fusion}}^{\text{eq}} \sim 1$ . Reversed magnetic shear [Ishida, *et al.* (1997)] and Fujita, *et al.* (1999).

A common feature of  $\langle \pi_{xy} \rangle$  and  $\langle \pi_{x\parallel} \rangle$  is that both of them are equal to zero for  $\hat{v}'_{0\parallel} = 0$  and that the magnitudes increase with the increasing of the flow shear  $\hat{v}'_{0\parallel}$ .

The micro-thermal flux  $q_x$  is given in Fig. 9.16 for  $\tau = 1$ ,  $b_s = 0.1$ , and  $s = 0.1$ . In Fig. 9.16(a)  $\hat{v}'_{0\parallel} = -1.5$ ,  $\eta_i = 1, 2, 3$ , and 4. In contrast to the momentum fluxes  $\pi_{xy}$  and  $\pi_{x\parallel}$ , the energy flux is always positive and increases with  $\eta_i$ . In Fig. 9.16(b)  $\eta_i = 1$ ,  $\hat{v}'_{0\parallel} = -1.5, -0.5, 0.5$ , and 1.5. It is easy to notice that the curve for  $\hat{v}'_{0\parallel} = -1.5$  is identical to the curve for  $\hat{v}'_{0\parallel} = 1.5$  but shifts towards the left. It is the same for the curves of  $\hat{v}'_{0\parallel} = -0.5$  and 0.5.

### Threshold $\nabla T$ for Convection



Model of Internal Transport Barrier  
for JT-60U Shot E27969

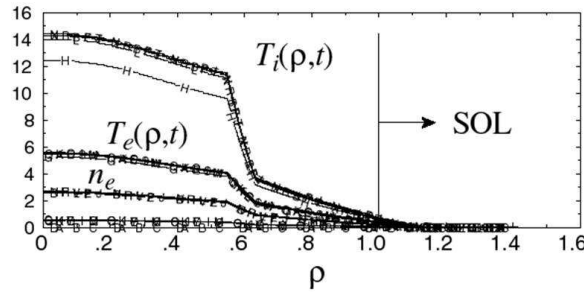


Figure 9.16: Boundaries of collisional and turbulent diffusivities.

The integrated energy flux  $\langle q_x \rangle$  [Eq. (9.13)] is shown in Fig. 9.16 as function of the parallel flow shear  $\hat{v}'_{0\parallel}$  for  $\tau = 1, b_s = 0.1$ . For given magnetic shear  $s = 0.1$  the energy flux increases with the increasing of  $\eta_i$  [see Fig. 9.16(a)] while for  $\eta_i = 1$  it decreases with the increasing of the magnetic shear  $s$  [see Fig. 9.16(b)]. The momentum fluxes  $\langle \pi_{xy} \rangle$  and  $\langle \pi_{x\parallel} \rangle$  are zero while the energy flux is not for  $\hat{v}'_{0\parallel} = 0$ .

All the above mentioned variations of  $\langle \pi_{xy} \rangle, \pi_{xy}, \langle \pi_{x\parallel} \rangle, \pi_{x\parallel}, \langle q_x \rangle$  and  $q_x$  with the parameters  $(s, \eta_i, \hat{v}'_{0\parallel})$  are at a fixed  $\phi_0^2$  so that additional variation through the dependence of  $\phi_0^2$  on the parameters must be further calculated for comparisons with a laboratory physics system.

For Coulomb collisions the corresponding inverse Prandtl numbers are

$$\frac{\chi}{\mu_{\parallel}} \simeq 7, \quad \frac{\chi}{\mu_{\perp}} \simeq 1.7.$$

Thus the turbulent Prandtl numbers ( $\simeq 0.01$ ) are small compared with the Coulomb collisional



values ( $\simeq 0.6$ ). There are no parameters in the theory based on the Coulomb collision corresponding to  $\mu_{\perp}$ . The viscosity parameter  $\mu_{\perp}$  introduced is unique for the theory of turbulence driven by velocity shear.

#### 9.4.14 Analysis of turbulent transport with shear flow

It is widely recognized by fusion physicists [*Jenko and Dorland* (2002), *Erba, et al.* (1995, 1999)], that the plasma dynamics in the bulk region and in the Scrape-Off Layer (SOL) are significantly different from each other. As a consequence there must be a transition region around the edge of the limiter or the Last Closed Flux Surface (LCFS), where some of the plasma parameters change rather rapidly across the region. In other words, the edge plasma is characterized by a rapid radial dependence of the plasma parameters such as parallel plasma flow velocity. Particles may move freely along the magnetic field lines in the bulk plasma while such freedom does not exist in SOL due to the presence of limiter and divertor plates.

Experimentally, a poloidal flow shear has been observed in the vicinity of a material limiter [*Chen and Sen* (1995)], in a ohmically-heated plasma. The poloidal velocity shear is important in the L-H transition [*Chen and Cheng* (1980)]. We present evidence showing that the plasma parallel velocity changes at about the same radial location as the poloidal shear flow layer. These measurements were taken on the TEXT-U tokamak with plasma conditions  $B_T = 2.5$  T,  $I_p = 220$  kA, and a line-averaged density,  $\bar{n}_e = 3.0 \times 10^{13} \text{ cm}^{-3}$ , using a reciprocating probe array. The plasma was defined by three rail limiters located at  $r = 27$  cm. The probe array was mounted on the top of the vessel separated from the limiters by  $247.5^\circ$  in the plasma current direction. The toroidal magnetic field was in the same direction as the plasma current, and the ion grad- $B$  drift was upwards. Figure ??(a) shows a radial profile of the parallel flow Mach number  $M = v_{\parallel}/c_d$  measured with a Mach probe with two collecting electrodes biased with  $-180$  V to collect ion saturation currents from upstream and downstream. The current ratio can then be used to calculate the flow Mach number [*Fukuyama, et al.* (1994), *Furnish, et al.* (1999), *Gang, et al.* (1991)] with the approximation that the ion temperature is equal to the electron temperature. We used the Hutchinson model [*Gang, et al.* (1991)] which includes diffusion and viscosity into the probe presheath. The ion flow direction is in the direction of the toroidal magnetic field and plasma current. Figure ??(b) presents the normalized radial derivative of the ion parallel velocity. In Fig. ??(c) we show a radial profile of the poloidal phase velocity,  $v_{\text{phase}}$ , used to define the shear layer [*Chen and Sen* (1995)]. The phase velocity is derived from the power spectrum measured with a two-point correlation technique,  $v_{\text{phase}} = \sum_{k,\omega} \frac{\omega}{k} S(\omega, k) / \sum_{k,\omega} S(\omega, k)$ , where  $S(k, \omega)$  is the measured power spectra [*Garbet and Waltz* (1996)] as a function of wavenumber and frequency. Since the phase velocity measurements were not taken on the same shot as the data on parallel flow velocity, it is important to note that the plasma conditions were similar and the location of the velocity shear layer is generally robust for the plasma conditions used. We estimate the uncertainty in position for the location of the flow shear layer to be of order 4 mm. To within the limits of plasma reproducibility the maximum gradient of the parallel ion flow occurs at the same radial position as the velocity shear in the perpendicular direction.

In order to make detailed comparison possible the quasilinear saturation amplitude is estimated in the following. Suppose that the mixing length saturation level is determined by the condition that

$$x \frac{dv_{\parallel}}{dx} \sim \tilde{v}_{\parallel}(x), \quad (9.55)$$

which is valid if  $|\tilde{v}'_{0\parallel}| \gtrsim 1 + \eta_i$ . Noting from the motion equation in the parallel direction that  $\tilde{v}_{\parallel} = (\text{esc}_s/T_e \hat{\omega}) x \tilde{\phi}$ , then it is straightforward to have

$$\phi_0 \sim \frac{T_e}{e} \frac{\rho_s}{L_n} \tilde{v}'_{0\parallel}. \quad (9.56)$$

For  $\tilde{v}'_{0\parallel} < 1 + \eta_i$  the saturation level is  $\phi_0 \simeq (\eta_i - \eta_{ic})/\langle k_x^2 \rangle^{1/2} \simeq (\eta_i - \eta_{ic})/\langle k_y^2 \rangle^{1/2}$ .

Substituting Eq. (9.23) into Eqs. (9.11)–(9.13) gives the approximate formulas as follows

$$\begin{aligned} \langle \pi_{xy} \rangle &= -\frac{c^2 T_e^2}{e^2 B^2 L_n^2} \frac{(\pi)^{1/2} k_y \rho_s}{s^{5/2}} \frac{\gamma^{1/2} |\hat{\omega}|^2 K \tilde{v}_{0\parallel}'^3}{|\hat{\omega} + K|^2} \\ &= -\left( \frac{c T_e}{e B L_n} \right)^2 F_{\perp}(\eta_i, \tau, s, \tilde{v}_{0\parallel}', b_s), \end{aligned} \quad (9.57)$$

$$\begin{aligned} \langle \pi_{x\parallel} \rangle &= -\frac{c^2 T_e^2}{e^2 B^2 L_n^2} \frac{(\pi)^{1/2} k_y \rho_s}{s^{5/2}} \frac{\gamma^{1/2} |\hat{\omega}|^3 \tilde{v}_{0\parallel}'^3}{|\hat{\omega} + K|^2} \\ &= -\left( \frac{c T_e}{e B L_n} \right)^2 F_{\parallel}(\eta_i, \tau, s, \tilde{v}_{0\parallel}', b_s), \end{aligned} \quad (9.58)$$

$$\begin{aligned} \langle q_x \rangle &= \frac{c^2 T_e^2}{e^2 B^2 L_n c_s} P_0 (1 + \eta_i) (\pi \gamma)^{1/2} k_y \rho_s L_n s^{5/2} |\hat{\omega}| \tilde{v}_{0\parallel}'^2 \\ &= -\left( \frac{\rho_s^2 c_s}{L_n} \right) G(\eta_i, \tau, s, \tilde{v}_{0\parallel}', b_s) \frac{dP_0}{dx}. \end{aligned} \quad (9.59)$$

To obtain the fluxes as function of system parameters the value of  $\hat{\omega} = \hat{\omega}_r + i\gamma$  must be calculated from Eq. (9.2) and substitute into Eqs. (9.24)–(9.26). 9. The dimensionless functions  $F_{\perp}$ ,  $F_{\parallel}$ , and  $G$  are given by

$$\begin{aligned} F_{\perp}(\eta_i, \tau, s, \tilde{v}_{0\parallel}', b_s) &= \frac{(\pi)^{1/2} k_y \rho_s}{s^{5/2}} \frac{\gamma^{1/2} |\hat{\omega}|^2 K \tilde{v}_{0\parallel}'^3}{|\hat{\omega} + K|^2} \\ F_{\parallel}(\eta_i, \tau, s, \tilde{v}_{0\parallel}', b_s) &= \frac{(\pi)^{1/2} k_y \rho_s}{s^{5/2}} \frac{\gamma^{1/2} |\hat{\omega}|^3 \tilde{v}_{0\parallel}'^3}{|\hat{\omega} + K|^2} \end{aligned}$$

and

$$G(\eta_i, \tau, s, \tilde{v}_{0\parallel}', b_s) = \frac{(\pi \gamma)^{1/2} k_y \rho_s}{s^{5/2}} |\hat{\omega}| \tilde{v}_{0\parallel}'^2.$$

The equation for generation of the poloidal velocity  $\langle v_\theta \rangle$  is

$$\frac{\partial}{\partial t} \langle v_\theta \rangle = -\frac{1}{r} \frac{\partial}{\partial r} (r \langle \pi_{xy} \rangle). \quad (9.60)$$

In the present case, the parameters are approximately constant except for  $\hat{v}_{0\parallel}'$ , then

$$\begin{aligned} \frac{\partial}{\partial x} \langle \pi_{xy} \rangle &= -\frac{c^2 T_e^2}{e^2 L_n^3 B^2} \frac{k_y \rho_s (\pi)^{1/2}}{s^{5/2}} \frac{\gamma^{1/2} |\hat{\omega}|^2 K}{|\hat{\omega} + K|^2} \left( 3 + \frac{\gamma K^2 \hat{v}_{0\parallel}'^2}{2s |\hat{\omega} + K|^4} \right) \hat{v}_{0\parallel}'^2 \hat{v}_{0\parallel}'' \\ &= -\frac{c^2 T_e^2}{e^2 L_n^3 B^2} H(\eta_i, \tau, s, b_s, \hat{v}_{0\parallel}', \hat{v}_{0\parallel}'') , \end{aligned} \quad (9.61)$$

where  $\hat{v}_{0\parallel}'' = L_n^2 d^2 v_{\parallel} / c_s dx^2$  and  $K = L_n / L_p$  and

$$H(\eta_i, \tau, s, b_s, \hat{v}_{0\parallel}', \hat{v}_{0\parallel}'') = \frac{k_y \rho_s (\pi)^{1/2}}{s^{5/2}} \frac{\gamma^{1/2} |\hat{\omega}|^2 K}{|\hat{\omega} + K|^2} \left( 3 + \frac{\gamma K^2 \hat{v}_{0\parallel}'^2}{2s |\hat{\omega} + K|^4} \right) \hat{v}_{0\parallel}'^2 \hat{v}_{0\parallel}''.$$

Equations (9.60) and (9.61) show that the driving force for the poloidal velocity is independent of the sign of  $\hat{v}_{0\parallel}'$  but depend on the sign of  $\hat{v}_{0\parallel}''$ . Such dependence of the driving force on  $\hat{v}_{0\parallel}''$  determines the dependence of  $\langle v_\theta \rangle$  on  $\hat{v}_{0\parallel}''$  as will be discussed later. In general, the functions  $F_\perp$ ,  $F_\parallel$ ,  $G$ , and  $H$  should be replaced by  $F_\perp A$ ,  $F_\parallel A$ ,  $GA$ , and  $HA$ , where the exponential part  $A = \exp(\gamma \hat{v}_{0\parallel}'^2 K^2 / 4s |\hat{\omega} + K|^4) \sim 1$  since for this plasma system  $\gamma \hat{v}_{0\parallel}'^2 K^2 / 4s |\hat{\omega} + K|^4 \simeq \gamma \hat{v}_{0\parallel}'^2 / 4s K^2 \ll 1$  when  $\gamma$  is given by Eq. (9.54).

Measurements from the TEXT-U experiment show [Hahm (2002)] that the measured poloidal plasma velocity shear increases with plasma current, decreases with chord average density and the toroidal magnetic field. The shear layer width is a constant over a range of discharge conditions. There is no explicit dependence on plasma density  $\bar{n}$  and current  $I_p$  in Eq. (9.61). However, both the decrease of density  $\bar{n}$  and the increase of current  $I_p$  correspond to an increase of electron temperature  $T_e$  in the shear layer which explicitly appears in Eq. (9.61). The poloidal driving force given in Eq. (9.61) is inversely proportional to  $B^2$ . In summary, the driving force given in Eq. (9.61) is qualitatively in agreement with the measured scaling when the damping mechanism is approximately independent of those parameters. There is no simple scaling for the shear layer width from this model. Physically, it is reasonable to estimate the poloidal shear layer width as approximately the same as of the parallel flow shear.

Some damping mechanism must be introduced to estimate the steady state poloidal velocity driven by the turbulence. As an example the magnetic damping is considered as the only damping mechanism and equilibrium poloidal velocity is included. Under these conditions the plasma motion equation in the poloidal direction, Eq. (9.60) will be modified as follows [Biskamp, *et al.* (1994), Jenko and Dorland (2002), Doyle *et al.* (1991)]

$$\frac{\partial}{\partial t} \langle v_\theta \rangle = -\frac{1}{r} \frac{\partial}{\partial r} (r \langle \pi_{xy} \rangle) - \nu^{\text{nc}} (\langle v_\theta \rangle - v_\theta^{\text{nc}}) \quad (9.62)$$

where  $v_\theta^{\text{nc}}$  is the equilibrium poloidal velocity, and

$$\nu^{\text{nc}} = \frac{\nu_{ii}}{\epsilon^{3/2}(1 + \nu_*)(1 + \epsilon^{2/3}\nu_*)} \quad (9.63)$$

with  $\nu_* = \nu_{ii}qR/v_\theta\epsilon^{3/2}$  and  $\epsilon$  is the inverse aspect ratio,  $q$  the safety factor,  $R$  the major radius and  $\nu_{ii}$  the ion-ion collision frequency. In steady state Eq. (9.62) reduces to

$$\langle v_\theta \rangle - v_\theta^{\text{nc}} = -\frac{1}{\nu^{\text{nc}}} \frac{\partial}{\partial x} \langle \pi_{xy} \rangle. \quad (9.64)$$

For the dimensionless parameters  $(\eta_i, s, \tau, \widehat{v}'_{0\parallel}, b_s)$  of order unity the poloidal acceleration from the divergence of the momentum flux is of the magnitude  $(cT_e/eBL_n)^2/L_n \simeq v_{de}^2/L_n$  compared with the neoclassical damping rate  $\nu^{\text{nc}}$ .

In order to make further comparison it is assumed that the equilibrium poloidal velocity  $v_\theta^{\text{nc}}$  is negligible, and that the plasma is around the boundary between the Pfirsch-Schlüter and the plateau regimes with  $l \sim qR$  so that  $\nu^{\text{nc}} \simeq \nu_{ii}$ . Then the steady-state poloidal velocity [Eq. (9.31)] reduces to

$$\langle v_\theta \rangle = \frac{1}{\nu_{ii}} \frac{v_{de}^2}{L_n} H(\eta_i, \tau, s, b_s, \widehat{v}'_{0\parallel}, \widehat{v}''_{0\parallel}). \quad (9.65)$$

For the typical TEXT discharge parameters:  $T_e = T_i = 40 \text{ eV}$ ,  $B = 20 \text{ kG}$ ,  $n = 3 \times 10^{12} / \text{cm}^3$ ,  $L_n = 3 \text{ cm}$ , which gives

$$\frac{1}{\nu_{ii}} \frac{v_{de}^2}{L_n} \simeq 2.1 \times 10^5 \text{ cm/s}.$$

The function  $H$  is sensitive to  $\widehat{v}'_{0\parallel}$ . For the parameters used in this study, i.e.  $s = 0.1, b_s = 0.1, \eta_i \sim 1, \tau = 1$ , the results are given in Fig. 9.11.  $H$  versus  $\widehat{v}''_{0\parallel}$  is given in Fig. 9.11(a) for  $\widehat{v}'_{0\parallel} = 0.5$ . The maximum value of  $H$  is about 10 for  $\widehat{v}'_{0\parallel} = 1$ . These numbers are in reasonable agreement with the experimental observations,  $\langle v_\theta \rangle \sim -3$  to  $+3 \times 10^5 \text{ cm/s}$ . It should be noted that the suppression effect of the poloidal velocity shear on the fluctuation is not considered in this calculation. In this regard the driving force from the turbulent Reynolds stress is overestimated. On the other hand, however, the saturation level evaluation [Eq. (9.23)] is made without taking the ion temperature gradient ( $\eta_i$ ) effect into account. This may lead to underestimation of the driving force. These two factors may compensate each other so that the theoretical numbers are well in the regime of the experimental observations.

According to Eq. (9.64) the dependence of  $\langle v_\theta \rangle$  on  $\widehat{v}''_{0\parallel}$  is the same as given Eq. (9.61) for the driving force and is qualitatively in agreement with the experimental observations given in Fig. 9.10 from TEXT-U Tokamak. Roughly speaking,  $\langle v_\theta \rangle$  has the same sign as that of  $\widehat{v}''_{0\parallel}$  and changes sign at the same location where  $\widehat{v}''_{0\parallel} \simeq 0$ . The correlation between  $\langle v_\theta \rangle$  and  $\widehat{v}''_{0\parallel}$  is impressive though the data shown here are not from the same discharge. To further study the profile of the turbulence driven  $\langle v_\theta \rangle$ , the profile of the derivative of the parallel velocity can be modeled as  $\widehat{v}'_{0\parallel}(x) = -0.5 \text{sech}(\alpha x)$ , with  $\alpha$  being a constant of order unity and  $x = 0$  the position where  $\widehat{v}'_{0\parallel}(x)$  has minimum. Then the function  $H(x)$  is given in Fig. 9.10(b). It is reasonable to assume that  $v_{de}^2/\nu_{ii}L_n$  is roughly a constant in the velocity shear layer. Under these assumptions the

poloidal velocity profile from this model is approximately the same as that given in Fig. 9.10(b) which is similar to the experimental results given in Fig. 9.9(c) and in *Hahm* (2002).

The width of the velocity shear layer can be estimated as

$$\Delta \simeq \frac{\langle \pi_{xy} \rangle}{\nu_{ii} \langle v_\theta \rangle} \sim \frac{4 \times 10^9}{3.2 \times 10^9} \sim 1 \text{ cm} \quad (9.66)$$

and is in good agreement with the experimental observations.

To close this section we would like to say a few words about the L–H transition from the point of view of the model suggested in this chapter. One typical feature of the L–H transition is that  $v_\theta$  and  $|v'_\theta| = |dv_\theta/dr|$  increase rapidly ( $\sim 100\mu\text{s}$ ) during the transition. The driving force given in Eq. (9.28) exponentially increases with  $\widehat{v}_{0\parallel}^2 K^2 / |\widehat{\omega} + K|^4$ . Usually  $|\widehat{\omega}| < K$  so that such increase is slow as long as  $|\widehat{v}_{0\parallel}| < K$ . However, the acceleration increases rapidly when  $|\widehat{v}_{0\parallel}| \gtrsim K$ . It may be possible that the condition  $|\widehat{v}_{0\parallel}| \gtrsim K$ , (i.e.  $|v_\parallel/dx| \gtrsim c_s(L_n + L_T)T_i/L_n L_T T_e$ ) somehow is achieved and triggers the L–H transition. Another concern is how the acceleration process is stopped. It has been demonstrated [*Antipov, et al.* (1985), *Antonova* (1983), *Balescu* (1988), *Colas, et al.* (1998)] that the mode growth rate will decrease after the poloidal flow is driven up. The driving force in Eq. (9.28) is proportional to the  $\frac{3}{2}$ -power of the mode growth rate so that the acceleration stops when the mode becomes marginally stable. This stopping effect can be modeled by taking  $\gamma = \gamma_0(1 - v_\theta'^2/v_{\theta\text{crit}}'^2)$ . Another mechanism to stop the acceleration is that  $L_n$  becomes small in the shear flow layer after L–H transition so that the dimensionless driving force parameter  $\widehat{v}_{0\parallel}' = L_n dv_\parallel/c_s dr$  is negligibly small even though  $dv_\parallel/dr$  hardly changes. The plasma will eventually enter into a steady state when other drag forces such as the magnetic damping are taken into account.

#### 9.4.15 The role of parallel sheared flow

The instability driven by parallel flow shear is studied within the fluid approximation in a local slab configuration with magnetic shear. Ion temperature gradient  $\eta_i$  is taken into account. The dimensionless parameter set of the problem is  $(\eta_i, \tau, s, \widehat{v}_{0\parallel}', b_s)$ . The quasilinear expressions for the radial fluxes of the parallel momentum  $\langle \pi_{x\parallel} \rangle$ , the perpendicular momentum  $\langle \pi_{xy} \rangle$  and the thermal energy  $\langle q_x \rangle$  are derived using the exact linear eigenfunction. The perpendicular and parallel momentum fluxes, called Reynolds stress, are shown to vanish when the dimensionless parameter  $\widehat{v}_{0\parallel}' = 0$  due to the symmetry feature of the mode structure about the rational surface. Such symmetry property is broken leading to nonzero parallel and perpendicular momentum transport as long as  $\widehat{v}_{0\parallel}' \neq 0$ . This dependence on the parallel velocity shear does not hold for the thermal energy flux:  $\langle q_x \rangle$  does not vanish when  $\widehat{v}_{0\parallel}' = 0$ . The Reynolds stress exponentially increases with  $(T_e L_n L_T / T_i (L_n + L_T) c_s)^2 (dv_\parallel/dx)^2$ , while it is proportional to the square of the electron temperature  $T_e^2$  and inversely proportional to the square of the toroidal magnetic field  $B^2$ . Experimental measurements of the parallel and poloidal plasma flows on TEXT–U tokamak carried out support the interpretation that the poloidal shear flow is generated through the turbulence

driven by parallel sheared plasma flow. The theoretical models are compared and shown to be of reasonable agreement with the experimental observations for scalings as well as for magnitudes when the neoclassical damping mechanism is introduced to balance the driving force from the Reynolds stress.

The transport coefficients  $(\mu_{\perp}, \mu_{\parallel}, \chi)$  induced by the  $\mathbf{E} \times \mathbf{B}$  turbulence of the instability are obtained analytically. They are always positive. The positivity of the turbulent transport means that entropy production from the transformation of the ordered flows into the turbulent fluctuations is positive definite. The ratio of the energy transport coefficient to the viscosity coefficient is derived and studied numerically.

In *Biskamp, et al.* (1994) hydrodynamic simulations showed that the evolution of  $\widehat{v}_{\parallel}'$ -driven turbulence and the reaction of the turbulence through  $\pi_{xy}$  and  $\pi_{yx}$  on the mean shear flows including the creation of  $\mathbf{E} \times \mathbf{B}$  shear flow. A self-consistent study about the poloidal flow generation by the turbulence and the fluctuation suppression by the poloidal velocity shear is an active area of research.

As is pointed out in *Erba, et al.* (1999), the tokamak plasma is a complex physical system. The edge region, where more physics processes take place than in the bulk region, is the most complex subsystem. The model suggested in this chapter does not exclude other models for the subject of the sheared flow generation. The parallel flow shear is only one of the physical phenomena which exhibit and influence the plasma behavior in the edge region. The emphasis here is that a parallel velocity shear exists in the edge region plasma and provides a free energy source for turbulence, as well as a symmetry breaking element which is necessary for the poloidal sheared flow generation by turbulence in quasilinear theory.

#### 9.4.16 Impurity-induced micro-electromagnetic instabilities in toroidal plasmas

Impurities are important elements in tokamak plasmas. Impurities affect stability, transport, confinement, and safety. Impurity effects on ITG, TEM and AITG modes, and the by impurity-induced electrostatic modes have been studied in tokamak and Field-Reversed Pinch (FRP) plasmas [*Antipov, et al.* (1982, 1985), *Antonova* (1983), *Balescu* (1988), *Biskamp* (1997)]. Kinetic shear Alfvén and kinetic ballooning instabilities have been investigated without the effects of impurities. The impurity induced electromagnetic instabilities (KSA and KBM) are now reviewed [*Zhong, et al.* (2016)].

### 9.4.17 Double critical gradients of impurity density in the HL-2A divertor tokamak for edge electromagnetic turbulence

HL-2A is a divertor tokamak reconstructed SWIP in Chengdu, China and is based on original ASDEX main components (vacuum vessel and magnet coils) [Yan, *et al.* (2002)]. HL-2A project is an important part of the fusion research program of China. The mission of the HL-2A Project is to explore the physics issues involved in advanced tokamaks. Most of the important issues of fusion physics, such as confinement improvement, divertor and scrape-off layer physics, wall conditioning, MHD instability and energetic particles, auxiliary heating and current drive, are studied and explored on the HL-2A through the progressive improvement of the hardware [Liu, *et al.* (2004)]. For the first phase, the divertor (edge plasma) and confinement research was emphasized. The experimental results from HL-2A have made contributions to the development of worldwide fusion research. After realizing the objective for closed divertor research for a period of operation, the divertor was modified into an open divertor [Yan, *et al.* (2002)].

Two experimental campaigns were conducted on HL-2A tokamak in 2003 and 2004 after the first plasma was obtained at the end of 2002. Progress in several aspects has been made, especially in the divertor discharge and feedback control of the plasma configuration. The following operation parameters have been achieved:  $I_p = 320$  kA,  $B_t = 2.2$  T and discharge duration  $T_d = 1580$  ms. With the feedback control of plasma current and horizontal position, an excellent repeatability of discharge was achieved. The tokamak has been operated in both limiter configurations and single null (SN) divertor configurations. The HL-2A SN divertor configuration is simulated with the MHD equilibrium code SWEQU. The divertor experimental results were compared with the simulation results obtained for the HL-2B configuration. When the divertor configuration is formed, the impurity radiation in main plasma decreases remarkably. The plasma performance improves significantly after siliconization. The experiments include

- (a) Divertor  $D_\alpha$  and edge  $n_z$  measurements
- (b)  $B_\theta$  fluctuations measured with Mirnov coil
- (c)  $n_e$  fluctuations from reflectometry (ped. top) data
- (d) Coherence ( $B_\theta$  and  $n_e$  fluctuation data)
- (e) Evolution of integrated coherence for EM turbulence
- (f) Filtered  $B_\theta$  fluctuation of EM turbulence in H-mode
- (g) EM turbulence intensity in H-mode
- (h) Edge impurity accumulation occurrence of EM turbulence (50-150 kHz)
- (i) I: LCOs  $\rightarrow n_z$  decreases  $\rightarrow$  EM turbulence is replaced by ES turbulence

The plasma coherence is noticeably higher in the H-mode and the EM turbulence is localized around the pedestal top. There is exponential growth and then saturation of the EM plasma turbulence.

### 9.4.18 Comparison between experimental and HD7 results with C<sup>+4</sup> impurity ions

The strong asymmetry of the two critical gradients is consistent with the experimental observation [Zhong, *et al.* (2016)].

The impact of impurity ions on a pedestal has been investigated in the HL-2A Tokamak, at the Southwestern Institute of Physics, Chengdu, China. Experimental results have clearly shown that during the H-mode phase, an electromagnetic turbulence was excited in the edge plasma region, where the impurity ions exhibited a peaked profile. It has been found that double impurity critical gradients are responsible for triggering the turbulence. Strong stiffness of the impurity profile has been observed during cyclic transitions between the I-phase and H-mode regime. The results suggest that the underlying physics of the self-regulated edge impurity profile offers the possibility for an active control of the pedestal dynamics via pedestal turbulence.

### 9.4.19 Impurity modes with sheared flow finite-beta plasmas

Do these results have general meaning? The modes are induced by impurities. They are EM modes with finite-beta effects.

### 9.4.20 Physics model and equations

Axisymmetric toroidal configurations of circular flux surfaces with Shafranov shift ( $s$ - $\alpha$  model); Ballooning mode representation;

Gyrokinetic theory retaining the following:

Full main and impurity ion transit  $k_p v_p$ ;

Curvature and magnetic gradient drifts for main and impurity ions  $\omega_D(v_\perp^2, v_p^2, \theta)$ ;

Finite Larmor radius effects;

Ion magnetic trapping is neglected.

The analysis is complicated and requires further numerical work. Here we outline the turbulence problem. The quasineutrality condition is

$$\sum_x Z_s n_x^{0/0} = 0$$



Parallel component of Ampère's law:

$$\nabla_{\perp}^2 A_p = -\frac{4\pi}{c} \sum_s j_s^{0/0}$$

$s = 1, z, e$  for hydrogen, impurity, and electron plasma components. The dynamics is given by

$$n_s^{0/0} = \int f_s d^3v, \quad J_{sp}^{0/0} = q_s \int \nu_p f_s d^3v, \quad f_s = -\frac{q_s F_{Ms}}{T_s} \phi^{0/0} + h_s J_0(\delta_s)$$

$$i \frac{\nu_p}{qR} \frac{\partial}{\partial \theta} h_s + (\omega - \omega_{Ds}) h_s = (\omega - \omega_{*sT}) J_0(\delta_s) F_{Ms} \frac{q_s n_{0s}}{T_s} \left( \phi^S(\theta) - \frac{\nu_p}{c} \mu_{Ap}(\theta) \right).$$

The eigenmode equations are

$$[1 + \tau_i(1 - f_z) + \tau_z Z f_z] \phi^S(k) = \int_{-\infty}^{+\infty} \frac{dk'}{\sqrt{2\pi}} \left\{ (K_{11}^i(k, k') + K_{11}^z(k, k')) \phi^S(k') \right.$$

$$\left. + [(K_{12}^i(k, k') + K_{12}^z(k, k')) + K_{12}^e(k, k')] \mu_{Ap}(k') \right\},$$

$$\frac{k_{\perp}^2}{2\tau_i} \mu_{Ap}(k) = \int_{-\infty}^{+\infty} \frac{dk'}{\sqrt{2\pi}} \left\{ [(K_{21}^i(k, k') + K_{21}^z(k, k')) + K_{21}^e(k, k')] \phi^S(k') \right.$$

$$\left. + [(K_{22}^i(k, k') + K_{22}^z(k, k')) + K_{22}^e(k, k')] \mu_{Ap}(k') \right\},$$

where  $f_z = Zn_z n_e$  is the impurity charge concentration.

$$K_{m,n}^{s(s=i,z)}(k, k') = -i \int_{-\infty}^0 \omega_{*e} d\tau H_{m,n}^s(\tau, k, k'),$$

and

$$H_{11}^s(\tau, k, k') = \sqrt{2} f_s e^{-i\omega\tau} \frac{\exp[-(k, k')^2/4\lambda_s]}{\sqrt{a_s}(1+a_s)\sqrt{\lambda_s}} \times \left\{ \omega\tau_s Z_s + L_{es} \left[ 1 + \tau_s \left( -\frac{3}{2} + \frac{2}{1+a_s} \right) \right] \right.$$

$$\left. + L_{es} \eta_s \left[ \left( \frac{(k, k')^2}{4a_s \lambda_s} - \frac{k_{\perp}^2 + k'_{\perp}^2}{1+a_s} \frac{\mu_s}{\tau_s Z_s^2} \right) + \frac{2k_{\perp} k'_{\perp}}{1+a_s} \frac{\mu_s}{\tau_s Z_s^2} \frac{I_1}{I_0} \right] \right\} \Gamma_{0s}(k_{\perp}, k'_{\perp}),$$

$$H_{12}^s(\tau, k, k') = \frac{k - k'}{2\sqrt{a_s \lambda_s}} H_{11}^s(\tau, k, k'),$$

$$H_{21}^s(\tau, k, k') = -\beta_s \frac{(k - k')}{2\sqrt{a_s \lambda_s}} H_{11}^s(\tau, k, k'),$$

$$\begin{aligned}
H_{22}^s(\tau, k, k') &= -\beta_s \frac{(k - k')^2}{4a_s \lambda_s} H_{11}^s(\tau, k, k'), \\
K_{12}^e(k, k') &= \frac{iq\sqrt{\pi\tau_i}}{2\sqrt{2}\varepsilon_n S} (\omega - 1) \text{sgn}(k, k'), \quad K_{12}^e(k, k') = -\beta_i K_{12}^e, \\
g(\theta, \theta') &= (s + 1)(\sin \theta - \sin \theta') - s(\theta \cos \theta - \theta' \cos \theta') - \frac{\alpha}{2}(\theta - \theta' - \sin \theta \cos \theta + \sin \theta' \cos \theta'), \\
\lambda_s &= \frac{\tau^2 \omega_{*e}^2}{a_s} \frac{1}{\tau_s \mu_s} \left( \frac{s}{q} \varepsilon_n \right)^2 a_s = 1 + i \frac{2\varepsilon_n}{\tau_s Z_s} \frac{g(\theta, \theta')}{(\theta - \theta')} \omega_{*e} \tau, \\
\Gamma_{0s} &= I_0 \left( \frac{k_\perp k'_\perp}{(1 + a_s)} \frac{\mu_s}{\tau_s Z_s^2} \right) \exp \left[ -\frac{k_\perp^2 + k'_\perp^2}{2(1 + a_s)} \frac{\mu_s}{\tau_s Z_s^2} \right], \\
k_\perp^2 &= k_\theta^2 + k^2, \quad k'_\perp^2 = k'_\theta^2 + k'^2, \quad k = k_\theta(s\theta - \alpha \sin \theta), \quad k' = k_\theta(s\theta' - \alpha \sin \theta'), \\
\alpha &= -R_0 q^2 \frac{d\beta}{dr} = \frac{q^2 \beta_e}{\varepsilon - n} \left\{ \frac{L_{ei}(1 - f_z)}{\tau_i} (\eta_i + 1) + (\eta_e + 1) + \frac{L_{ez} f_z}{Z_e \tau_e} (1 + \eta_z) \right\}.
\end{aligned}$$

**Typical test case parameters:**

$$\begin{aligned}
\eta_i &= \eta_e = 0, & q &= 4.0, & 1/L_{ns} &= -\partial \ln n_s / \partial r, \\
T_e/T_i &= \tau_i = T_e/T_z = \tau_z = 1, & k_\theta \rho_s &= 0.3, s = 2.0, \\
m_i/m_e &= 1836, & \beta_e &= 0.01, & f_z = Zn_z/n_e &= 0.3.
\end{aligned}$$

## 9.5 Nonlinear MHD Simulations of Pellet Triggered Edge Localized Modes (ELMs) for ITER Plasma Scenarios

ITER operation in its high-fusion performance DT scenarios relies on the achievement of the H-mode confinement regime, which is expected to lead to the quasi-periodic triggering of Edge Localized Modes (ELMs) [Fututani, *et al.* (2017)]. The energy fluxes associated with natural (or ‘uncontrolled’) ELMs are expected to produce excessive erosion and/or superficial surface damage on the plasma facing component and large tungsten W influxes due to the wall sputtering during the ELMs. Controlled triggering of ELMs by the injection of small deuterium-ice pellets at frequencies significantly exceeding those of uncontrolled ELMs is one of the schemes to control ELM energy losses, divertor power fluxes and W production during ELMs. Although the technique has been demonstrated to decrease ELM energy loss successfully in ASDEX Upgrade [Lang, *et al.* (2004)], JET [Lang, *et al.* (2013)], and DIII-D [Baylor, *et al.* (2013)], uncertainties still remain regarding the physics understanding as well as of the consequence of its application, such

as localized power loads associated with this technique [Wenninger, *et al.* (2011)]. The nonlinear MHD simulations with the JOREK code [Huijsmans and Czarny (2007), Futatani, *et al.* (2014)] have been performed to study the dependence of the pellet size required to trigger an ELM in the ITER plasma, and also the dependency of the threshold on the pedestal plasma pressure when the pellet is injected; based on the assumption of that the pedestal pressure leading to spontaneous ELM triggering is 150 kPa pedestal pressure of 75 kPa and 112.5 kPa have been studied. The work leads to the estimations of the requirements for the pellet injection conditions to control ELMs in ITER 15 MA plasma operation scenarios.

## 9.6 Implemented Pellet Modeling in JOREK MHD Code

The nonlinear MHD code JOREK includes a model for the density source coming from the ablation of an injected deuterium pellet [Huijsmans and Czarny (2007), Futatani, *et al.* (2014), Futatani (2016)]. The pellet is assumed to travel along a straight line with a given fixed velocity. The amplitude of the space and time varying density source is such that the integrated source rate is consistent with the Neutral Gas Shielding (NGS) pellet ablation model [Gal, *et al.* (2008)]. With nonlinear MHD equations, the pellet ablation process is calculated self-consistently. The ablation of the pellet as it travels into the plasma causes a large local, moving density source. Since the deuterium pellet injection is mostly adiabatic, the temperature at the location of the density source will drop such that the local pressure stays constant initially. Due to the large heat conductivity, the region over which the density perturbation extends will be quickly heated up. This results in a strong local increase of the pressure which triggers an ELM.

## 9.7 Pellet–Triggered ELM in ITER 15 MA/5.3 T $Q = 10$ Operation Scenarios

The ITER plasma equilibrium profiles which have the pressure of 150 kPa, 112.5 kPa and 75 kPa at the pedestal top are prepared as shown in Fig. 9.17. The distance to the edge MHD stability limit of the target plasma is varied by changing the pedestal pressure gradient, and, self-consistently, the pedestal bootstrap current in a given number of steps (at 50% and 75% of the maximum stable condition which corresponds to the 150 kPa of the pressure at the pedestal top). There will be three pellet injection ports in ITER plasma as shown in Fig. 9.17 In JOREK, the initial pellet locations are chosen to be located slightly outside of the separatrix.

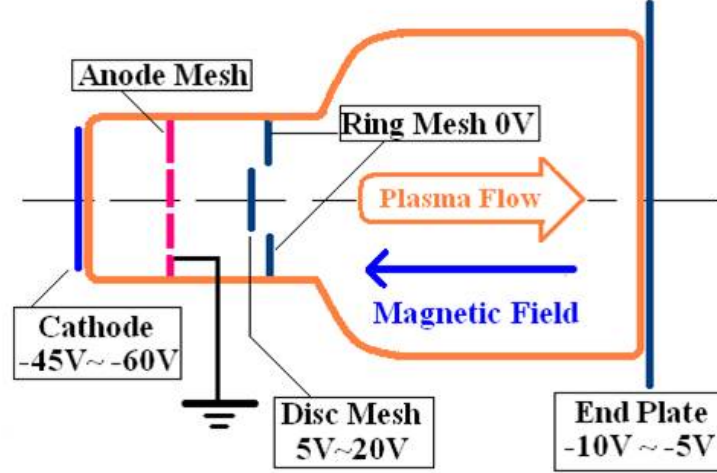


Figure 9.17: Typical Plasma Parameters: Plasma Density:  $n \sim 5 \times 10^8 - 3 \times 10^9 \text{ cm}^{-3}$ ; Magnetic Field in Cell Region:  $B_{r\text{mcell}} \cong 1 \text{ kG}$ ; Electron Temperature:  $T_e \sim 8 - 20 \text{ eV}$ ; Ion Temperature:  $T_i \sim 3 \text{ eV}$ ; Plasma Cell Length:  $L \sim 10 \text{ cm}$ .

The dependence of ELM size on the pellet size has been studied for the pedestal pressure of 75 kPa. The pellet injection velocity is 300 m/s, and the injection location is the X-point region. Simulations of the pellet injection from the X-point region have been performed with the toroidal modes  $n$  of  $n = 0$  to 10. The pellet size has been varied from  $1.0 \times 10^{21} \text{ D/pellet}$  (3.0 mm of cylindrical pellet) to  $4.0 \times 10^{21} \text{ D/pellet}$  (4.7 mm), with pellet injection speed of 300 m/s; the time of injection of the pellet is  $t = 2443.1 \mu\text{s}$ . The pellet ablation rate profile versus normalized flux is shown in Fig. 9.17. The pellet ablation profiles show some oscillations in the vicinity of the time of the maximum pellet ablation rate. This is due to the interaction between the pellet ablated particles and the local plasma temperature. Figure shows the time evolution of the magnetic energies of toroidal modes of  $n = 8 - 10$ . The pellet triggering ELM appears at  $2800 \mu\text{s}$  for the largest pellet case,  $4.0 \times 10^{21} \text{ D}$ . The duration of the ELM crash due to the pellet triggered ELM is  $600 \mu\text{s} - 800 \mu\text{s}$  which is a reasonable value. The pellet injections in the plasma which is in the MHD stability limit, i.e. the 112.5 kPa at the pedestal top have been carried out. The parameters of the pellet injection is identical with the studies of 75 kPa. The pellet size has been varied for two sizes,  $1.0 \times 10^{21} \text{ D/pellet}$  and  $2.0 \times 10^{21} \text{ D/pellet}$ . The pellet ablation rate profile versus time and versus normalized flux is shown in Fig. 9.17. The 112.5 kPa plasma has higher temperature profile than the one of 75 kPa, therefore the pellet ablation rate is higher than the one of 75 kPa case. Figure shows the magnetic energies of the  $n = 8 - 10$  modes after the pellet injection. The pellet with  $2.0 \times 10^{21} \text{ D}$  atoms increases the MHD activity strongly.

The time evolution of the energy content inside of the separatrix is compared for 75 kPa and 112 kPa plasmas as shown in Fig. and Fig. , respectively. The energy content in the plasma decreases due to the pellet-triggered ELM. The 75 kPa shows that the energy loss has a nonlinear dependence on the pellet size as shown in Fig. . It means the smaller pellets, such as  $1.0 \times 10^{21} \text{ D}$  and  $2.0 \times 10^{21} \text{ D}$  do not trigger an ELM while the  $4.0 \times 10^{21} \text{ D}$  pellet triggers an ELM which leads

to a large energy release from the plasma. The pellet of  $1.0 \times 10^{21}$  D in 112.5 kPa plasma leads the energy loss of 0.1% of the total plasma in 100 s. The pellet injection of the pellet size  $2.0 \times 10^{21}$  D in 75 kPa plasma leads 0.23% of the total energy in 100 s while the pellet of  $2.0 \times 10^{21}$  D leads 0.47% of the energy loss in 1000 s.

The nonlinear MHD simulations with the JOREK code show that the size of the pellet required to trigger an ELM depends on the pedestal plasma pressure when the pellet is injected; for 15 MA plasmas it is necessary to increase the pellet size by a factor of 1.5 (in number of particles) to trigger ELMs for a pedestal pressure of 75 kPa compared to 112.5 kPa (note that for the pedestal assumptions in these simulations the pedestal pressure leading to spontaneous triggering of ELMs is 150 kPa). In these simulations it has also been found that the magnitude of the ELM energy loss is strongly correlated with the pedestal plasma pressure (lower at lower pressures) rather than with the size of the pellet that is required for triggering (larger at lower pressures). The next important step is to investigate the pellet triggered ELM in the presence of realistic plasma flows including diamagnetic drift, neoclassical effects, and toroidal rotation which had been neglected in previous studies.

# Bibliography

- [1] Antipov, S. V., Nezlin, M. V., Snezhkin, E. N. and Trubnikov, A. S. (1982). Rossby soliton in the laboratory, *Sov. Phys. JETP* **55**, p. 85, <https://ui.adsabs.harvard.edu/#abs/1982ZhETF..82..145A/abstract>.
- [2] Antipov, S. V. Nezlin, M. V., Snezhkin, E. N. and Trubnikov, A. S. (1985). Rossby autosoliton and laboratory model of Jupiter's Great Red Spot, *Soviet Phys. JETP* **62**, p. 1097.
- [3] Antonova, R. A. (1983). Drift solitons in a shallow rotating fluid, *JETP Lett.* **37**, p. 651, <https://ui.adsabs.harvard.edu/abs/1983ZhPmR..37..545A/abstract>.
- [4] Balescu, R. (1988). *Transport Processes in Plasmas* (North-Holland-Amsterdam), Vols. 1–2.
- [5] Baylor, L. R., Commaux, N., Jernigan, T. C., Brooks, N. H., Combs, S. K., Evans, T. E., Fenstermacher, M. E., Isler, R. C., Lasnier, C. J., Meitner, S. J., Moyer, R. A., Osborne, T. H., Parks, P. B., Snyder, P. B., Strait, E. J., Unterberg, E. A. and Loarte, A. (2013). Reduction of edge-localized mode intensity using high-repetition rate-pellet injection in tokamak H-mode plasmas, *Phys. Rev. Lett.* **110**, p. 245001, <https://doi.org/10.1103/PhysRevLett.110.245001>.
- [6] Biskamp, D., Camaargo, S. J. and Scott, B. D. (1994). Spectral properties and statistics of resistive drift-wave turbulence, *Phys. Lett. A*, **186**, p. 239, [https://doi.org/10.1016/0375-9601\(94\)90346-8](https://doi.org/10.1016/0375-9601(94)90346-8).
- [7] Biskamp, D., Schwarz, E. and Drake, J. F. (1997). Two-fluid theory of collisionless magnetic reconnection, *Phys. Plasmas* **4**, p. 1002, <https://doi.org/10.1063/1.872211>.
- [8] Burrell, K. H. (1997). Effects of  $\mathbf{E} \times \mathbf{B}$  velocity shear and magnetic shear on turbulence and transport in magnetic confinement devices, *Phys. Plasmas* **4**, p. 1499, <http://dx.doi.org/10.1063/1.872367>.
- [9] Carreras, B. A., Garcia, L. and Diamond, P. H. (1987). Theory of resistive pressure-gradient-driven turbulence, *Phys. Fluids* **30**, p. 1388, <http://dx.doi.org/10.1063/1.866518>.
- [10] Chen, F. F. (1965a). Resistive over-stabilities and anomalous diffusion, *Phys. Fluids* **8**, p. 912, <http://dx.doi.org/10.1063/1.1761335>.

- [11] Chen, F. F. (1965b). Excitation of drift instabilities in thermionic plasmas, *J. Nucl. Energy Pt. C*, **7**, p. 399, <https://doi.org/10.1088/0368-3281/7/4/305>.
- [12] Chen, F. F. (1965c). Effects of sheaths on drift instabilities in thermionic plasmas, *Phys. Fluids* **8**, p. 752, <https://doi.org/10.1063/1.1761294>.
- [13] Chen, L. and Cheng, C. Z. (1980). Drift-wave eigenmodes in toroidal plasmas, *Phys. Fluids* **23**, p. 2242, <https://doi.org/10.1063/1.862907>.
- [14] Chen, J. and Sen, A. K. (1995). Experimental study of a mixed slab and toroidal ion-temperature-gradient mode, *Phys. Plasmas* **2**, p. 3063, <https://doi.org/10.1063/1.871204>.
- [15] Chen, L. and Zonca, F. (2019). Self-consistent kinetic theory with nonlinear wave-particle resonances, *Plasma Sci. Technol.* **21**, p. 125101, <https://doi.org/10.1088/2058-6272/ab3dce>.
- [16] Colas, L., Zou, X. L., Paume, M., Chareau, J., Guiziou, L., Hoang, G. T., Michelot, Y. and Grésillon, D. (1998). Internal magnetic fluctuations and electron heat transport in the Tora Supra Tokamak: Observation by cross-polarization scattering, *Nuclear Fusion* **38**, pp. 903–918, <http://dx.doi.org/10.1088/0029-5515/38/6/308>.
- [17] Connor, J. W. (1993). Pressure gradient turbulent transport and collisionless reconnection, *Plasma Phys. Control. Fusion* **35**, pp. 757–763, <http://dx.doi.org/10.1088/0741-3335/35/6/009>.
- [18] Devynck, P., Garbet, X., Laviron, C., Payan, J., Saha, S. K., Gervais, F., Hennequin, P., Quemeneur, A. and Truc, A. (1993). Localized measurements of turbulence in the TORE SUPRA tokamak *Plasma Phys. Control. Fusion* **35**, p. 63, <https://doi.org/10.1088/0741-3335/35/1/005>.
- [19] Dimits, A. M., Bateman, G., Beer, M. A., Cohen, B. I., Dorland, W., Hammett, G. W., Kim, C., Kinsey, J. E., Kotschenreuther, M., Kritiz, A. H., Lao, L. L., Andrekas, J. M., Nevins, W. M., Parker, S. E., Redd, A. J., Shumaker, D. E., Sydora, R., and Weiland, J. (2000). Comparisons and physics basis of tokamak transport models and turbulence simulations *Phys. Plasmas* **7**, pp. 969–983, <https://doi.org/10.1063/1.873896>.
- [20] Dong, J-Q., Sanuki, H., Itoh, K. and Chen, L. (2002). Electron temperature gradient instability in toroidal plasmas, *Phys. Plasmas* **9**, p. 4699, <https://doi.org/10.1063/1.1515275>.
- [21] Dong, J-Q., Jian, G. D., Wang, A. K., Sanuki, H. and Itoh, K. (2002b). Instability and transport driven by electron temperature gradient close to critical, 19th IAEA Fusion Energy Conference, (Lyon, France, October 2002), IAEA-CN-94/TH/1-6.

- [22] Dorland, W., Jenko F., Kotschenreuther, M. and Rogers, B. N. (2000). *Phys. Rev. Lett.* **85** p. 5579, <https://doi.org/10.1103/PhysRevLett.85.5579>.
- [23] Doyle, E. J., Groebner, R. J., Burrell, K. H., Gohil, P., Lehecka, T., Luhmann, Jr., N. C., Matsumoto, H., Osborne, T. H., Peebles, W. A. and Philipona, R. (1991). Modifications in turbulence and edge electric fields at the L–H transition in the DIII–D tokamak, *Phys. Fluids B* **3**, pp 2300–2307, <https://doi.org/10.1063/1.859597>.
- [24] Durst, R. D., Fonck, R. J., Kim, J. S., Paul, S. F., Bretz, N., Bush, C., Chang, Z. and Hulse, R., (1993). Observation of a localized transition from edge to core density turbulence in the TFTR tokamak, *Phys. Rev. Lett.* **71**, pp. 3135–3138, <https://doi.org/10.1103/PhysRevLett.71.3135>.
- [25] Erba, M., Parail, V., Springmann, E. and Taroni, A. (1995). Extension of a Bohm model for L–mode electron heat transport to ion heat transport and to the ohmic regime, *Plasma Phys. Control. Fusion* **37**, p. 1249, <https://doi.org/10.1088/0741-3335/37/11/005>.
- [26] Erba, M., Aniel, T., Basiuk, V., Becoulet, A. and Litaudon, X. (1998). Validation of a new mixed Bohm/gyroBohm model for electron and ion heat transport against the ITER, Tore Supra and START database discharges, *Nucl. Fusion* **38**, p. 1013, <http://dx.doi.org/10.1088/0029-5515/38/7/305>.
- [27] Erba, M., Horton, W. and Ottaviani, M. (1999). Predictive tests of ITG based models of tokamak heat transport on ITER database discharges, *Nucl. Fusion* **39**, p. 495, <http://dx.doi.org/10.1088/0029-5515/39/4/307>.
- [28] Fukuyama, K., Itoh, S–I., Itoh, M., Yagi, M. and Azumi, M. (1994). Theory of improved confinement in high– $\beta_p$  tokamaks, *Plasma Phys. Control. Fusion* **36**, p. 1385, <https://doi.org/10.1088/0741-3335/36/9/001>.
- [29] Furnish, G., Horton, W., Kishimoto, Y., LeBrun, M. J. and Tajima, T. (1999) Global gyrokinetic simulation of tokamak transport *Phys. Plasmas* **6**, p. 1227, <https://doi.org/10.1063/1.873366>.
- [30] Futatani, S., Huijsmans, G., Laorte, A., Baylor, L. R., Commaux, N., Jernigan, T. C., Fenstermacher, M. E., Lasnier, C., Osborne, T. H. and Pegourié, B. (2014). Nonlinear MHD modeling of ELM triggering by pellet injection in DIII–D and implications for ITER, *Nucl. Fusion* **54**, p. 073008, <https://doi.org/10.1088/0029-5515/54/7/073008>.
- [31] Futatani, S. *et al.*, 26th IAEA Fusion Energy Conference, Kyoto, Japan (2016), 43rd EPS Conference Leuven, Belgium (2016).
- [32] Futatani, S., Huijsmans, G. T. A., Loarte, A., Mantsinen, M., Pamela, S., Garzotti, L., Hoelzl, M., Lang, P. T. and Orain, F. (2017). Nonlinear MHD simulations of pellet–triggered ELM for ITER plasma scenarios. In 44th EPS Conference on Plasma Physics. Geneva: European Physical Society, <http://hdl.handle.net/21.11116/0000-0000-B2B2-D>.



- [33] Gal, K., Belonohy, E., Kocsis, G., Lang, P. T., Veres, G. and the ASDEX Upgrade Team. (2008). Role of shielding in modeling cryogenic deuterium pellet ablation, *Nucl. Fusion* **48**, p. 085005, <https://doi.org/10.1088/0029-5515/48/8/085005>.
- [34] Gang, F. Y., Diamond, P. H. and Rosenbluth, M. N. (1991). A kinetic theory of trapped-electron-driven drift wave turbulence in a sheared magnetic field, *Phys. Fluids B* **3**, p. 68, <https://doi.org/10.1063/1.859957>.
- [35] Garbet, X. and Waltz, R. E. (1996). Action at distance and Bohm scaling of turbulence in tokamaks, *Phys. Plasmas* **3**, pp. 1898–1907, <https://doi.org/10.1063/1.871985>.
- [36] Hahm, T. S. (2002). Physics behind transport barrier theory and simulations, *Plasma Phys. Control. Fusion* **44**, p. A87, <https://doi.org/10.1088/0741-3335/44/5A/305>.
- [37] Halfmoon, M., Hatch, D., Kotschenreuther, M., Mahajan, S., Hassan, E., Nelson, O., Laggner, F., Diallo, A. and Groebner, R. (2019). Application of gyrokinetic “Fingerprints: in identifying microinstabilities in DIII-D pedestals, 61st Annual Meeting of the APS Division of Plasma Physics, October 21–25, 2019, Fort Lauderdale, Florida.
- [38] Hallatschek, K. and Biskamp, D. (2001). Transport control by coherent zonal flows in the core/edge transitional regime, *Phys. Rev. Lett.* **86**, p. 1223, <https://doi.org/10.1103/PhysRevLett.86.1223>.
- [39] Hasegawa, A. and Mima, K. (1977). Stationary spectrum of strong turbulence in magnetized nonuniform plasma, *Phys. Rev. Lett.* **39**, p. 205, <https://doi.org/10.1103/PhysRevLett.39.205>.
- [40] Hasegawa, A. and Mima, K. (1978), Pseudo-three-dimensional turbulence in magnetized nonuniform plasma, *Phys. Fluids* **21**, pp. 87–92, <https://doi.org/10.1063/1.862083>.
- [41] Hasegawa, A. MacLennan, C. G. and Kodama, Y. (1979). Nonlinear behavior and turbulence spectra of drift waves and Rossby waves, *Phys. Fluids*, **22**, pp. 2122–2129, <https://doi.org/10.1063/1.862504>.
- [42] Hasegawa, A. and Wakatani, M. (1983). Plasma edge turbulence, *Phys. Rev. Lett.* **50**, p. 682, <https://doi.org/10.1103/PhysRevLett.50.682>.
- [43] Hendel, H. W., Chu, T. K. and Politzer, P. A. (1968). Collisional drift waves—Identification, stabilization, and enhanced plasma transport, *Phys. Fluids* **11**, p. 2426, <http://dx.doi.org/10.1063/1.1691833>.
- [44] Hinton, F. L. and Horton, W. (1971). Amplitude limitation of a collisional drift wave instability, *Phys. Fluids* **14**, pp. 116–123, <https://doi.org/10.1063/1.1693260>.
- [45] Hirose, A, Elia, M. and Smolyakov, A. I. (2002). Short wavelength temperature gradient driven modes in tokamaks, *Phys. Plasmas* **9**, p. 1659, <https://doi.org/10.1063/1.1469025>.

- [46] Hirose, A. and Elia, M. (2002). Short wavelength temperature gradient driven modes in tokamaks. II. Electron mode, *Phys. Plasmas* **9**, p. 4664, <https://doi.org/10.1063/1.1513470>.
- [47] Hoang, G. T., Saoutic, B., Guiziou, L., Basiuk, V., Becoulet, A., Budny, R. V., Clairet, F., Colas, L., Devynck, P., Gil, C., Joffrin, E., Litaudon, X., Segui, J-L., Voitsekhovitch, I. and Zou, X. L. (1998). *Nucl. Fusion* **38**, p. 117, <https://doi.org/10.1088/0029-5515/38/1/311>.
- [48] Hoang, G. T., Bourdelle, C., Garbet, X., Giruzzi, G., Aniel, T. and Ottaviani, M., Horton, W., Zhu, P. and Budney, R. V. (2001). Experimental determination of critical threshold in electron transport on tore supra, *Phys. Rev. Lett.* **87**, p. 125001, <http://dx.doi.org/10.1103/PhysRevLett.87.125001>.
- [49] Holland, C. and Diamond, P. H. (2002). Electromagnetic secondary instabilities in electron temperature gradient turbulence, *Phys. Plasmas* **9**, p. 3857, <http://dx.doi.org/10.1063/1.1496761>.
- [50] Hong, B-G., Horton, W., Hamaguchi, S., Wakatani, M., Yagi, M. and Sugama, H. (1991). Transition from resistive- $G$  to  $\eta_i$  driven turbulence in stellarator systems, *Phys. Fluids B: Plasma Phys.* **3**, p. 1638, <https://doi.org/10.1063/1.859683>
- [51] Horton, W. (1976). Spectral distribution of drift-wave fluctuations in tokamaks, *Phys. Rev. Lett.* **37**, p. 1269, <http://dx.doi.org/10.1103/PhysRevLett.37.1269>.
- [52] Horton, W. (1990). Nonlinear drift waves and transport in magnetized plasma, *Phys. Rep.* **192**, pp. 1-177, [https://doi.org/10.1016/0370-1573\(90\)90148-U](https://doi.org/10.1016/0370-1573(90)90148-U).
- [53] Horton, W., Wootton, A. and Wakatani, M. (Eds.) (1994). In U.S.-Japan Workshop on Ion Temperature Gradient Driven Turbulent Transport, *AIP Conference Proceedings*, Vol. 284, p. 255 (10 pp).
- [54] Horton, W. and Ichikawa, Y. (1996). *Chaos and Structures in Nonlinear Plasmas* (World Scientific) ISBN:8177642340.
- [55] Horton, W., Hu, B., Dong, J-Q. and Zhu, P. (2003). Turbulent electron thermal transport in tokamaks, *New J. Phys.* **5**, p. 14, <http://dx.doi.org/10.1088/1367-2630/5/1/314>.
- [56] Horton, W. (2018). *Turbulent Transport in Magnetized Plasmas*, 2nd Edition (World Scientific, 2018), ISBN:978-981-3225-86-6.
- [57] Hu, et al. (2002).
- [58] Huang, Q., Hu, B., Zhong, W., Chen, L. and Shi, Y. (2019). Effects of background pressure on the arc characteristics of gas spark gap, *Plasma Sci. Technol.* **21**, p. 125401, <https://doi.org/10.1088/2058-6272/ab3058>.

- [59] Huijsmans, G. T. A. and Czarny, O. (2007). MHD stability in X-point geometry: simulation of ELMs, *Nucl. Fusion* **47**, pp. 659–666, <https://doi.org/10.1088/0029-5515/47/7/016>.
- [60] Idomura, Y., Wakatani, M. and Tokuda, S. (2000). Gyrokinetic theory of slab electron temperature gradient mode in negative shear tokamaks *Phys. Plasmas* **7**, p. 2456, <https://doi.org/10.1063/1.874085>.
- [61] Jenko F., Dorland, W., Kotschenreuther, M. and Rogers B. N. (2000). Electron temperature gradient driven turbulence, *Phys. Plasmas* **7** p. 1904, <https://doi.org/10.1063/1.874014>.
- [62] Jenko, F., Dorland, W. and Hammett, G. W. (2001). Critical gradient formula for toroidal electron temperature gradient modes, *Phys. Plasmas* **8**, p. 4096, <https://doi.org/10.1063/1.1391261>.
- [63] Jenko, F. and Dorland, W. (2002). Prediction of significant tokamak turbulence at electron gyroradius scales, *Phys. Rev. Lett.* **89**, p. 225001, <https://doi.org/10.1103/PhysRevLett.89.225001>.
- [64] Kadomtsev, B. B. and Pogutse, O. P. (1979). Electron heat conductivity of the plasma across a ‘braided’ magnetic field, *Nucl. Fusion, Suppl.* **1**, pp. 649–662, <https://ui.adsabs.harvard.edu/abs/1979ppcf....1..649K/abstract>.
- [65] Kadomtsev, B. B. (1992). *Tokamak Plasma: A Complex Physical System* (Institute of Physics Pub., Bristol, UK and Philadelphia) p. 153, ISBN:0750302348.
- [66] Kaye, S. M., Greenwald, M., Stroth, U., Kardaun, O., Kus, A., Schissel, D., DeBoo, J., Bracco, G., Thomsen, K., Cordey, J., Miura, Y., Matsuda, T., Tamai, H., Takizuda, T., Hirayama, T., Kikuchi, H., Naito, O., Chudnovskij, A., Ongena, J., and Hoang, G. T. (1997). *Nucl. Fusion* **37**, pp. 1303–1328, <https://doi.org/10.1088/0029-5515/37/9/I10>.
- [67] Kim, D. E., Choi, D.-I., Horton, W., Yushmanov, P. N. and Parail, V. V. (1990). Transition from neoclassical to turbulent electron diffusion, *Phys. Fluids B* **2**, p. 547, <https://doi.org/10.1063/1.859291>.
- [68] Kishimoto, Y., Tajima, T., Horton, W., LeBrun, M. J. and Kim, J-Y. (1996). Theory of self-organized critical transport in tokamak plasmas, *Phys. Plasmas* **3**, pp. 1289–1307, <http://dx.doi.org/10.1063/1.871754>.
- [69] Koide, Y., Kikuchi, M., Mori, M., Tsuji, S., Ishida, S., Asakura, N., Kamada, Y., Nishitani, T., Kawano, Y., Hatae, T., Fujita, T., Fukuda, T., Sakasai, A., Kondoh, T., Yoshino, R. and Neyatani, Y. (1994). Internal transport barrier on  $q = 3$  surface and poloidal plasma spin-up in JT-60U high- $\beta_p$  discharges, *Phys. Rev. Lett.* **72**, pp. 3662–3665, <http://dx.doi.org/10.1103/PhysRevLett.72.3662>.

- [70] Koniges, A. E., Crotinger, J. A. and Diamond, P.H. (1992). Structure formation and transport in dissipative drift-wave turbulence, *Phys. Fluids B: Plasma Phys.* **4**, p. 2785, <https://doi.org/10.1063/1.860151>.
- [71] Kotschenreuther, M., Liu, X., Hatch, D. R., Mahajan, S., Zheng, L., Diallo, A., Gorebner, R., the DIII-D Team, Hillesheim, J. C., Maggi, C. F., Giroud, C., Koechl, F., Parail, V., Saarelma, S., Solano, E. R., Chankin, A. and JET Contributors (2019). Gyrokinetic analysis and simulation of pedestals to identify the culprits for energy losses using ‘fingerprints’, *Nucl. Fusion* **59**, p. 096001, <https://doi.org/10.1088/1741-4326/ab1fa2>.
- [72] Krommes, J. A. and Hu, G. (1994). The role of dissipation in the theory and simulation of homogeneous plasma turbulence, and resolution of entropy paradox *Phys. Plasmas* **1**, p. 3211, <https://doi.org/10.1063/1.870475>.
- [73] Lang, P., Conway, G. D., Eich, T., Fattorini, L., Gruber, O., Gunter, S., Horton, L. D., Kalvin, S., Kallenbach, A., Kaufmann, M., Kocsis, G., Lorenz, A., Manso, M. E., Maraschek, M., Mertens, V., Neuhauser, J., Nunes, I., Schneider, W., Suttrop, W., Urano, H. and the ASDEX Upgrade Team. (2004). ELM pace making and mitigation by pellet injection in ASDEX Upgrade, *Nucl. Fusion* **44**, p. 665, <https://doi.org/10.1088/0029-5515/44/5/010>.
- [74] Lang, P., Frigione, D., Geraud, A., Alarcon, T., Bennett, P., Cseh, G., Garnier, D., Garzotti, L., Köchl, F., Kocsis, G., Lennholm, M., Neu, R., Mooney, R., Saarelma, S., Sieglin, B. and JET-EFDA Contributors. (2013). ELM pacing and trigger investigations at JET with the new ITER-like wall, *Nucl. Fusion* **53**, p. 073010, <https://doi.org/10.1088/0029-5515/53/7/073010>.
- [75] Lee, Y. C., Dong, J-Q. Gudzar, P. N. and Liu, C. S. (1987). Collisionless electron temperature gradient instability, *Phys. Fluids* **30**, p. 1331, <https://doi.org/10.1063/1.866248>.
- [76] Levinton, F. M., Zarnstorff, M. C., Batha, S. H., Bell, M., Bell, R. E., Budny, R. V., Bush, C., Chang, Z., Fredrickson, E., Janos, A., Manickam, J., Ramsey, A., Sabbagh, S. A., Schmidt, G. L., Synakowski, E. J. and Taylor, G. (1995). Improved confinement with reversed magnetic shear in TFTR, *Phys. Rev. Lett.* **75**, pp. 4417–4420, <http://dx.doi.org/10.1103/PhysRevLett.75.4417>.
- [77] Lin, Z., Hahm, T. S., Lee, W. W., Tang, W. M. and White, R. B. (1998). Turbulent transport reduction by zonal flows: massively parallel simulations, *Science* **281**, pp. 1835–1837, <http://dx.doi.org/10.1126/science.281.5384.1835>.
- [78] Liu, Y., Bondeson, A., Gribov, Y. and Polevoi, A. (2004). Stabilization of resistive wall modes in ITER by active feedback and toroidal rotation, *Nuclear Fusion* **44**, p. 232, <https://doi.org/10.1088/0029-5515/44/2/003>.
- [79] Liu, Xing (2018). Gyrokinetic simulation of pedestal turbulence using GENE, Dissertation, The University of Texas at Austin, <http://hdl.handle.net/2152/69104>.

- [80] Mazzucato, E. (1976). Small-scale density fluctuations in the adiabatic toroidal compressor, *Phys. Rev.* **36**, p. 792, <http://dx.doi.org/10.1103/PhysRevLett.36.792>.
- [81] Mazzucato, E. and Nazikian, R. (1993). Radial scale length of turbulent fluctuations in the main core of TFTR plasmas, *Phys. Rev. Lett.* **71**, p. 1840–1843, <https://doi.org/10.1103/PhysRevLett.71.1840>.
- [82] McWilliams, J. C., Weiss, J. B. and Yavneh, I. (1999). The vortices of homogeneous geostrophic turbulence, *J. Fluid Mech.* **401**, pp. 1–26, <https://doi.org/10.1017/S0022112099006382>.
- [83] Nelson, A., Kolen, E., Laggner, F., Izacard, O., Groebner, R., Eldon, D., Shafer, M., Leonard, A., Shiraki, D. and Sontag, A. (2018). Pedestal fueling variation in a closed divertor configuration at DIII-D, APS Division of Plasma Physics Meeting 2018, abstract id.PP11.030, <https://ui.adsabs.harvard.edu/abs/2018APS..DPPP11030N>.
- [84] Ohkawa, T. and Yoshikawa, M. (1967). Experimental observation and theoretical interpretation of low-frequency interchange instability in “average minimum- $B$ ” configurations, *Phys. Rev. Lett.* **19**, p. 1374, <https://doi.org/10.1103/PhysRevLett.19.1374>.
- [85] Ohkawa, T. (1978). A transport model for alcator scaling in tokamaks, *Phys. Lett. A* **67**, p. 35, [https://doi.org/10.1016/0375-9601\(78\)90560-1](https://doi.org/10.1016/0375-9601(78)90560-1).
- [86] Okabayashi, M. and Arunasalam, V. (1977). Study of drift-wave turbulence by microwave scattering in a toroidal plasma, *Nuclear Fusion* **17**, pp. 497–513, <https://doi.org/10.1088/0029-5515/17/3/010>.
- [87] Ottaviani, M., Horton, W. and Erba, M. (1997). The long wavelength behaviour of ion-temperature-gradient-driven turbulence and the radial dependence of the turbulent ion conductivity, *Plasma Phys. Control. Fusion* **39**, pp. 121–146, [https://doi.org/10.1016/S0370-1573\(96\)00056-7](https://doi.org/10.1016/S0370-1573(96)00056-7).
- [88] Ottaviani, M. and Manfredi, G. (1999). The gyroradius scaling of ion thermal transport from global numerical simulations of ion temperature gradient driven turbulence, *Phys. Plasmas* **6**, pp. 3267–3275, <https://doi.org/10.1063/1.873567>.
- [89] Pécseli, H. L., Rasmussen, J. Juul and Thomsen, K. (1984). Nonlinear interaction of convective cells in plasmas, *Phys. Rev. Lett.* **52**, pp. 2148–2151, <https://doi.org/10.1103/PhysRevLett.52.2148>.
- [90] Pécseli, H. L., Rasmussen, J. Juul and Thomsen, K. (1985). Nonlinear interaction of convective cells in plasmas, *Plasma Phys. Control. Fusion* **27**, pp. 837–846, <https://doi.org/10.1088/0741-3335/27/8/002>.
- [91] Perkins, F. W., Barnes, C. W., Johnson, D. W., Scott, S. D., Zarnstorff, M. C., Bell, M. G., Bell, R. E., Bush, C. E., Grek, B., Hill, K. W., Mansfield, D. K., Park, H., Ramsey, A.

- T., Schivell, Stratton, B. C. and Synakowski, E. (1993). Nondimensional transport scaling in the tokamak fusion test reactor: Is tokamak transport Bohm or gyro-Bohm? *Phys. Fluids B* **5**, pp. 477–498, <https://doi.org/10.1063/1.860534>.
- [92] Petty, C. C., Luce, T. C., Burrell, K. H., Chiu, S. C., deGrassie, J. S., Forest C. B., Gohil, P., Greenfield, C. M., Groebner, R. J., Harvey, R. W., Pinsker, R. I., Prater, R. and Waltz, R. E. (1995). Nondimensional transport scaling in DIII-D: Bohm versus gyroBohm resolved, *Phys. Plasmas* **2**, pp. 2342–2348, <https://doi.org/10.1063/1.871259>.
- [93] Petviashvili, V. I. (1977). Self-focusing of an electrostatic drift wave, *Sov. J. Plasma Phys.* **3**, p. 150, <https://ui.adsabs.harvard.edu/abs/1977FizPl...3..270P/abstract>.
- [94] Prager, S. C., Sen, A. K. and Marshall, T. C. (1974). Dissipative trapped-electron instability in cylindrical geometry, *Phys. Rev. Lett.* **33**, pp. 692–695, <https://doi.org/10.1103/PhysRevLett.33.692>.
- [95] Rebut, P. H., Watkins, M. L., Gambier, D. J. and Boucher, D. (1991). A program towards a fusion reactor, *Phys. Fluids B* **3**, p. 2209, <https://doi.org/10.1063/1.859638>.
- [96] Redd, A. J., Kritiz, A. H., Bateman, G. and Kinsey, J. E. (1997). Sensitivity of predictive tokamak plasma transport simulations *Phys. Plasmas* **4**, pp. 2207–2214, <https://doi.org/10.1063/1.872384>.
- [97] Rewoldt, G. and Tang, W. M. (1990). Toroidal microinstability studies of high-temperature tokamaks, *Phys. Fluids B: Phys. Plasmas* **2** p. 318, <https://doi.org/10.1063/1.859320>.
- [98] Robinson, P. A. (1997). Nonlinear wave collapse and strong turbulence, *Rev. Mod. Phys.* **69**, pp. 507–574, <https://doi.org/10.1103/RevModPhys.69.507>.
- [99] Rogers, B. N., Drake, J. F. and Zeiler, A. (1998). Phase space of tokamak edge turbulence, the L–H transition, and the formation of the edge pedestal *Phys. Rev. Lett.* **81**, p. 4396, <https://doi.org/10.1103/PhysRevLett.81.4396>.
- [100] Ross, D. W., Tang, W. M. and Adam, J.C. (1977). Study of trapped electron instabilities driven by magnetic curvature drifts, *Phys. Fluids* **20** p. 613, <https://doi.org/10.1063/1.861920>.
- [101] Ryter, F., Imbeaux, F., Leuterer, F., Fahrbach, H.–U., Suttrop, W. and ASDEX Upgrade Team. (2001a). Experimental characterization of the electron heat transport in low-density ASDEX Upgrade Plasmas, *Phys. Rev. Lett.* **86**, pp. 5498–5501, <http://dx.doi.org/10.1103/PhysRevLett.86.5498>.
- [102] Ryter, F., Leuterer, F., Pereverzev, G., Fahrbach, H.–U., Stober, J., Suttrop, W. and ASDEX Upgrade Team. (2001b). Experimental evidence for gradient length-driven electron transport in tokamaks, *Phys. Rev. Lett.* **86**, pp. 2325–2328, <http://dx.doi.org/10.1103/PhysRevLett.86.2325>.

- [103] Scarmozzino, R., Sen, A. K. and Navratil, G. A. (1986). Production and identification of a collisionless, curvature-driven, trapped-particle instability, *Phys. Rev. Lett.* **57**, pp. 1729–1732, <https://doi.org/10.1103/PhysRevLett.57.1729>.
- [104] Scott, B. (1989). Global consistency for thin flux tube treatment of toroidal geometry, *Phys. Plasmas* **5**, p. 2334, <https://doi.org/10.1063/1.872907>.
- [105] Sen, A. K., Chen, J. and Mauel, M. (1991). Production and identification of the ion-temperature-gradient instability, *Phys. Rev. Lett.* **66**, pp. 429–432, <http://dx.doi.org/10.1103/PhysRevLett.66.429>.
- [106] Shaing, K. C. (1988). Neoclassical quasilinear transport theory of fluctuations in toroidal plasmas, *Phys. Fluids* **31**, p. 2249, <http://dx.doi.org/10.1063/1.866626>.
- [107] Slough, J., Navratil, G. A. and Sen, A. K. (1981). Production and observation of the dissipative trapped-ion instability, *Phys. Rev. Lett.* **47**, p. 1057, <https://doi.org/10.1103/PhysRevLett.47.1057>.
- [108] Smolyakov, A. I., Yagi, M. and Kishimoto, Y. (2002). Short wavelength temperature gradient driven modes in tokamak plasmas, *Phys. Rev. Lett.* **89**, p. 125005, <https://doi.org/10.1103/PhysRevLett.89.125005>.
- [109] Stenzel, R. L. (1978). Experiments on current-driven three-dimensional ion sound turbulence. Part I: Return-current limited electron beam injection, *Phys. Fluids* **21**, p. 99, <http://dx.doi.org/10.1063/1.862085>.
- [110] Strait, E. J., Lao, L. L., Mauel, M. E., Rice, B. W., Taylor, T. S., Burrell, K. H., Chu, M. S., Lazarus, E. A., Osborne, T. H., Thompson, S. J. and Turnbull A. D. (1995). Enhanced confinement and stability in DIII-D discharges with reversed magnetic shear, *Phys. Rev. Lett.* **75**, pp. 4421–4424, <https://doi.org/10.1103/PhysRevLett.75.4421>.
- [111] Sugama, H., Wakatani, M. and Hasegawa, A. (1988). Study of resistive drift and resistive interchange modes in a cylindrical plasma with magnetic shear, *Phys. Fluids* **31** p. 1601, <https://doi.org/10.1063/1.866699>.
- [112] Sugama, H., Okamoto, M., Horton, W. and Wakatani, M. (1996). Transport processes and entropy production in toroidal plasmas with gyrokinetic electromagnetic turbulence, *Phys. Plasmas* **3**, pp. 2379–2394, <http://dx.doi.org/10.1063/1.871922>.
- [113] Surko, C. M. and Slusher, R. E. (1976). Study of the density fluctuations in the adiabatic toroidal compressor scattering tokamak using CO<sub>2</sub> laser, *Phys. Rev. Lett.* **37**, pp. 1747–1750, <https://doi.org/10.1103/PhysRevLett.37.1747>, Erratum *Phys. Rev. Lett.* **38**, p. 258 (1977).
- [114] Synakowski, E. J., Batha, S. H., Beer, M. A., Bell, M. G., Bell, R. E., Budny, R. V., Bush, C. E., Efthimion, P. C., Hahm, T. S., Hammett, G. W., LeBlanc, B., Levinton, F.,

- Mazzucato, E., Park, H., Ramsey, A. T., Schmidt, G., Rewoldt, G., Scott, S. E., Taylor, G. and Zarnstorff, M. C. (1997). Local transport barrier formation and relaxation in reverse-shear plasmas on the tokamak fusion test reactor, *Phys. Plasmas* **4**, pp. 1736–1744, <https://doi.org/10.1063/1.872275>.
- [115] Taroni, A., Erba, M., Tibone, F. and Springmann, E. (1994). Global and local energy confinement properties of simple transport coefficients of the Bohm type, *Plasma Phys. Control. Fusion* **36**, p. 1629, <http://dx.doi.org/10.1088/0741-3335/36/10/003>.
- [116] van Milligen, B. Ph., Nicolau J. H., Garcia, L., Carreras, B. A., Hidalgo, C. and the TJ-II Team. (2017). The impact of rational surfaces on radial heat transport in TJ-II, *Nucl. Fusion* **57**, p. 056028, <https://doi.org/10.1088/1741-4326/aa611f>.
- [117] Wakatani, M. and Hasegawa, A. (1984). A collisional drift wave description of plasma edge turbulence, *Phys. Fluids* **27**, p. 611, <https://doi.org/10.1063/1.864660>.
- [118] Wakatani, M., Watanabe, K., Sugama, H. and Hasegawa, A. (1992). Resistive drift wave and interchange turbulence in a cylindrical plasma with magnetic and velocity shear, *Phys. Fluids B: Plasma Phys.* **4**, pp. 1754–1765, <https://doi.org/10.1063/1.860031>.
- [119] Waltz, R. E., DeBoo, J. C. and Rosenbluth, M. N. (1990). Magnetic-field scaling of dimensionally similar tokamak discharges, *Phys. Rev. Lett.* **65**, p. 2390, <https://doi.org/10.1103/PhysRevLett.65.2390>.
- [120] Wenninger, R. P., Eich, T. H., Huijsmans, G. T. A., Lang, P. T., Devaux, S., Jachmich, S., Köchl, F. and JET EFDA Contributors. (2011). Scrape-off layer heat transport and divertor power deposition of pellet-induced edge localized modes, *Plasma Phys. Control. Fusion* **53**, p. 105002, <https://doi.org/10.1088/0741-3335/53/10/105002>.
- [121] Wong, K. L., Bretz, N. L., Hahm, T. S. and Synakowski, E. (1997). Short wavelength fluctuations and electron heat conductivity in enhanced reversed shear plasmas, *Phys. Lett. A* **236** p. 339–344, [https://doi.org/10.1016/S0375-9601\(97\)00806-2](https://doi.org/10.1016/S0375-9601(97)00806-2).
- [122] Yagi, M. and Horton, W. (1994). Reduced Braginskii equations, *Phys. Plasmas* **1**, p. 2135, <https://doi.org/10.1063/1.870611>.
- [123] Yan, et al. (2002).
- [124] Zakharov, V. E. (1972). Collapse of Langmuir waves, *Zh. Eksp. Teor. Fiz.* **62**, pp. 1745–1759.
- [125] Zakharov, V. E., L’vov, V. S. and Falkovich, G. (1992). Kolmogorov spectra of turbulence 1. Wave turbulence, (Springer-Verlag, Germany), p. 275, ISBN:3-540-54533-6.
- [126] Zhong, W. L., Shen, Y., Zou, X. L., Gao, J. M., Shi, Z. B., Dong, J-Q., Duan, X. R., Xu, M., Cui, Z. Y., Li, Y. G., Ji, X. Q., Yu, D. L., Cheng, J., Xiao, G. L., Jiang, M., Yang, Z. D. C., Zhang, B. Y., Shi, P. W., Liu, Z. T., Song, X. M., Ding, X. T. and Liu, Y.



- (HL-2A Team). (2016). Observation of double impurity critical gradients for electromagnetic turbulence excitation in tokamak plasmas, *Phys. Rev. Lett.* **117**, p. 045001, <https://doi.org/10.1103/PhysRevLett.117.045001>.
- [127] Zou, X. L., Colas, L., Paume, M., Chareau, J. M., Laurent, L., Devynck, P. and Gresillon, D. (1995). Internal magnetic turbulence measurement in plasma by cross polarization scattering, *Phys. Rev. Lett.* **75**, p. 1090, <https://doi.org/10.1103/PhysRevLett.75.1090>.